

HYDROPHOBINS – INVESTIGATION AND
CONTROL OF STRUCTURE FORMATION IN
AMPHIPHILIC FUNGAL PROTEINS

Dissertation

zur Erlangung des Doktorgrades der Naturwissenschaften
(Dr. rer. nat.)

der

Naturwissenschaftlichen Fakultät II
Chemie, Physik und Mathematik

der Martin-Luther-Universität
Halle-Wittenberg

vorgelegt von

Herrn Martin Kordts
geb. am 16. Januar 1990 in Halle (Saale)

Durchgeführt am: Institut für Chemie, Physikalische Chemie

Gutachter: Herr Prof. Dr. Dariush Hinderberger
Herr Prof. Dr. Bernd Abel

Datum der Verteidigung: 16.07.2020

“THE SUN IS SIMPLE. A SWORD IS SIMPLE. A STORM IS SIMPLE. BEHIND EVERYTHING
SIMPLE IS A HUGE TAIL OF COMPLICATED.”

— SIR TERRY PRATCHETT, *I SHALL WEAR MIDNIGHT*

TABLE OF CONTENTS

TABLE OF CONTENTS	5
LIST OF SYMBOLS AND ABBREVIATIONS.....	VII
LIST OF FIGURES AND TABLES.....	X
1. HYDROPHOBINS – CONTEXT AND BACKGROUND	1–11
1.1 Structure, classification and roles.....	1–11
1.2 Application potential and scientific challenges.....	1–14
2. THEORETICAL BACKGROUND AND EXPERIMENTAL PARAMETERS.....	2–17
2.1 Protein production and Purification.....	2–17
2.1.1 Deglycosylation of SC3.....	2–18
2.2 Surface tension and monolayers	2–20
2.2.1 Film Balance Measurements	2–21
2.2.2 Epi-fluorescence microscopy	2–23
2.3 Atomic Force Microscopy (AFM)	2–25
2.4 Dynamic Light Scattering (DLS)	2–28
2.5 Electron Paramagnetic Resonance Spectroscopy (EPR)	2–32
2.6 Spin-labelling of HFB2.....	2–37
2.7 Vesicle Preparation	2–40
3. THE AIR/WATER INTERFACE AND TRANSFER TO SOLID SUBSTRATES – THE INFLUENCE OF AREAL AND INTERFACIAL CONSTRAINTS ON MICROSCOPIC MORPHOLOGY	3–40
3.1 Single compression to various surface pressures.....	3–41
3.1.1 SC3	3–43
3.1.2 HFB2	3–47
3.2 Multiple compressions/expansions to various surface pressures.....	3–49
3.2.1 SC3	3–51
3.2.1.1 Epi-fluorescence microscopy.....	3–54
3.2.2 HFB2	3–60
3.2.3 Dendritic superstructures in both classes.....	3–63

3.2.3.1	Adsorption kinetics may reveal the underlying mechanisms.....	3-64
3.2.3.2	Fingering instability and the <i>Marangoni</i> effect	3-66
3.3	The impact of glycosylation on the compression isotherms of SC3.....	3-70
3.4	Summary, Conclusions and Outlook.....	3-73
3.4.1.1	Single compression to various surface pressures.....	3-73
3.4.1.2	Multiple cycles of constraint	3-74
3.4.1.3	Outlook.....	3-76
4.	IN SOLUTION – INTERACTION WITH PHOSPHOLIPID VESICLES.....	4-77
4.1	Mixed vesicles of POPC and 16-DSA – the guest’s perspective.....	4-78
4.2	Spin-labelled phospholipids – the vesicle’s perspective	4-87
4.3	Spin-labelled HFB2 – the protein’s perspective	4-89
4.4	Summary and outlook.....	4-91
5.	MULTIPLE FORMS, MULTIPLE FACES	5-93
5.1	Controlled assembly at the air/water interface	5-93
5.2	Protein – liposome interactions	5-95
5.3	The missing link.....	5-96
6.	REFERENCES.....	6-98
	APPENDIX	I
A.	Chapter 2.....	i
B.	Chapter 4.....	iv
	ACKNOWLEDGEMENTS.....	A
	SCIENTIFIC CONTRIBUTIONS	B
	List of publications	B
	Oral contributions	B
	Conferences.....	B
	CURRICULUM VITAE.....	D
	EIGENSTÄNDIGKEITSERKLÄRUNG	G

LIST OF SYMBOLS AND ABBREVIATIONS

$\langle I \rangle$	mean scattering intensity
16-DSA	16-DOXYL stearic acid
5-MSL	3-maleimido-PROXYL
A	Hyperfine coupling tensor with principal elements (A_{xx} , A_{yy} and A_{zz})
AFM	atomic force microscopy
a_{iso}	isotropic hyperfine coupling constant
B_0	external magnetic field
bis-ANS	4,4'-Dianilino-1,1'-binaphthyl-5,5'-disulfonic acid dipotassium salt
Cys	cysteine
DEER	Double electron – electron resonance
DLS	Dynamic Light Scattering
D_s	self-diffusion coefficient
D_s	translational diffusion coefficient
EPR	Electron Paramagnetic Resonance
ESI	electrospray ionization (mass spectrometry)
EZ	electron <i>Zeeman</i> effect
f	frictional coefficient (DLS)
FA	formic acid
FWHM	full width at half maximum
g	g-tensor with principal elements (g_{xx} , g_{yy} and g_{zz})
$g_1(\tau)$	normalized field time correlation function

$g_2(\tau)$	normalized intensity time correlation function
g_e	Landé-factor of the free electron in vacuum; $g_e = 2.00231930436256(35)$
g_{iso}	isotropic g-value
h	Planck's constant; $h = 6.62606876 \times 10^{-34} \text{ J s}$
HF	hyperfine coupling
HOPG	highly oriented pyrolytic graphite
IRRAS	Infra-red reflection absorption spectroscopy
k	Boltzmann constant; $k = 1.38064852 \times 10^{-23} \text{ m}^2 \text{ kg s}^{-2} \text{ K}^{-1}$
LB	Langmuir-Blodgett transfer
LS	Langmuir-Schaefer transfer
MALDI-TOF	matrix-assisted laser desorption/ionization time of flight (mass spectrometry)
m_I	nuclear secondary spin quantum number
m_s	electron secondary spin quantum number; $m_s = \pm 1/2$
MSL	maleimide spinlabel (see '5-MSL')
MWCO	molecular weight cut-off
NZ	nuclear <i>Zeeman</i> effect
PDI	polydispersity index
PDSPC	1-palmitoyl-2-stearoyl-(16-doxyl)-sn-glycero-3-phosphocholine
POPC	1-palmitoyl-2-oleoyl-sn-glycero-3-phosphocholine
q	wave vector

R_H	hydrodynamic radius
Rh123	2-(6-Amino-3-imino-3H-xanthen-9-yl)benzoic acid methyl ester
rmsd	root mean square deviation
SD	standard deviation
SDSL	site-directed spin labelling
SDS-PAGE	sodium dodecyl sulphate poly(acrylamide) gel electrophoresis
SEC	size-exclusion chromatography
Ser	serine
SOMO	singly occupied molecular orbital
T	absolute temperature
TFA	trifluoroacetic acid
TFMSA	trifluoromethanesulfonic acid
Thr	threonine
TICT	twisting intramolecular charge transfer
β_e	Bohr magneton; $\beta_e = 9.274009994(57) \times 10^{-24} \text{ J T}^{-1}$
Γ	decay constant
η	dynamic viscosity
Θ	scattering angle
λ_0	wavelength
ν	frequency
Π	surface pressure
Π_e	equilibrium spreading pressure

σ	surface tension
τ	correlation time (DLS)
τ_c	rotational correlation time (EPR)
ω_i	angular frequency of spin transition (EPR)

LIST OF FIGURES AND TABLES

Table 1 Reagents for the deglycosylation of SC3	2–19
Figure 1 Exemplary isotherm of a phospholipid monolayer exhibiting multiple phases taken from: Dörfler, H.-D., 2002; pp. 103 ff.....	2–22
Figure 2 Schematic depiction of transfer methods. (A) <i>Langmuir-Blodgett</i> ; (B) <i>Langmuir-Schäfer</i> . Courtesy of M. Kampe.	2–22
Figure 3 General setup and measurement principle of the atomic force microscope. Courtesy of M. Kampe.	2–26
Figure 4 Temporal intensity fluctuation. (measuring interval Δt is small compared to fluctuating time) adapted from: EISERMANN, J. 2017	2–29
Figure 5 Splitting of electronic energy levels due to the <i>Zeeman</i> effect. Adapted from: JUNK, M. J. N. 2012	2–33
Table 2 Common microwave frequency bands and corresponding magnetic fields used in EPR	2–34
Figure 6 Dependence of the isotropic hyperfine coupling constant on polarity. Adapted from: JUNK, M. J. N. 2012.....	2–36
Figure 7 X-band cwEPR spectra of spin-labelled HFB2 (<i>black</i>) and free MSL (<i>red</i>) under identical conditions.....	2–38
Figure 8 Q-Band spectra of spin-labelled HFB (<i>black</i>) and the free MSL (<i>red</i>) in water at room temperature.....	2–39
Figure 9 Compression isotherms of SC3 and HFB2 on pure water at 20 °C.....	3–42
Table 3 Mean molecular areas [\AA^2] and hysteresis at 6 mN/m between compression and expansion after the second cycle for both hydrophobins.	3–42

Table 4 Coverage of the mica surface by SC3 at different transfer pressures after a single compression.....	3–43
Figure 10 AFM height micrographs of SC3 at different transfer surface pressures	3–44
Figure 11 Height distribution of SC3 structures transferred at different surface pressures.....	3–45
Table 5 Average number, length and width of SC3 fibrils depending on transfer pressure.....	3–45
Figure 12 Length and width of fibrils depending on transfer pressure.	3–46
Figure 13 AFM height micrographs of HFBII at different surface pressures.....	3–47
Figure 14 Height distribution of HFBII structures transferred at different surface pressures.....	3–48
Figure 15 Coverage of the mica surface by protein films transferred at different surface pressures. <i>Left: SC3; right HFB2</i>	3–49
Figure 16 Hysteresis between the compression and expansion isotherms of HFB2.....	3–50
Figure 17 Height distribution of SC3 aggregates over several compression/expansion cycles to 13 mN/m.....	3–51
Figure 18 <i>top</i> : AFM height images after A) 1 compression, B) 1 expansion, C) 2 compressions, D) 2 expansions, E) 3 compressions F) 3 expansions, G) 4 compressions, H) 5 compressions	3–53
Figure 19 <i>top</i> : compression isotherm of SC3 on 0.5 μ M Bis-ANS solution; <i>bottom</i> : fluorescence microscopy images at the indicated points in the isotherm.	3–55
Figure 20 Compression isotherm of SC3 on a 1.4 μ M solution of Bis-ANS at 20 °C.....	3–57
Figure 21 Compression and expansion isotherms of SC3 on 15 nM Rh123 at 20 °C.....	3–58
Figure 22 Fluorescence microscopy images of SC3 on 15 nM Rh123 at 20 °C	3–59
Figure 23 AFM micrographs of HFB2 transferred at 13 mN/m.	3–61
Figure 24 Height distribution of HFBII structures transferred after several compressions to 13 mN/m and subsequent expansions.....	3–62
Figure 25 Coverage of the mica surface by HFBII after each compression to 13 mN/m and subsequent expansion.	3–62

Figure 26 <i>top</i> : AFM micrographs of A) HFB2 and B) SC3 transferred at 13 mN/m after one and three compressions, respectively <i>bottom</i> : cross-sections along the white lines	3–64
Figure 27 AFM height micrograph of HFB during the first compression; transferred at 3.3 mN/m.....	3–65
Figure 28 AFM height micrograph of HFB2 after single compression; transferred at 27.5 mM/m.....	3–68
Figure 29 Isotherms of SC3 for several compressions and expansions. <i>top</i> : native SC3; <i>bottom</i> : deglycosylated SC3	3–71
Figure 30 Schematic depiction of emergent dendritic structures.....	3–75
Figure 31 cwEPR spectra of mixed vesicles with POPC : 16-DSA ratios of 50:1 (<i>red</i> ; <i>bottom</i>) and 5:1 (<i>black</i> ; <i>top</i>) compared to 200 μ M 16-DSA (<i>blue</i> ; <i>top</i>) in water recorded at 20 °C	4–79
Figure 32 DLS traces of mixed vesicles with varying amounts of HFB2 (<i>left</i>) and SC3 (<i>right</i>), recorded in water at 20 °C and a scattering angle of 90 °	4–80
Figure 33 cwERP spectra of mixed vesicles with varying amounts of HFB2 in water recorded at 20 °C. <i>left</i> : full spectra; <i>right</i> : high field lines.....	4–81
Figure 34 experimental (<i>black</i>) and simulated (<i>red</i>) spectra of mixed vesicles for varying amounts of HFB2	4–82
Figure 35 cwERP spectra of mixed vesicles with varying amounts of SC3 in water recorded at 20 °C. <i>left</i> :full spectra; <i>right</i> : high field lines.....	4–83
Figure 36 experimental (<i>black</i>) and simulated (<i>red</i>) spectra of mixed vesicles. <i>top</i> : pure vesicles <i>bottom</i> : containing 8 g/L SC3	4–84
Table 6 simulation parameters for spectra shown in Figure 36.	4–84
Figure 37 Particle size distribution of PDSPC vesicles of varying composition in water at 20 °C	4–87
Figure 38 DLS traces for vesicles containing spin-labelled phospholipids with varying amounts of HFB (<i>left</i>) and SC3 (<i>right</i>) recorded in water at 20 °C.....	4–88
Figure 39 cwEPR spectra of PDSPC vesicles with SC3 (<i>left</i>) and HFB2 (<i>right</i>) recorded in water at 20 °C.	4–88
Figure 40 Particle size distribution of POPC vesicles with different amounts of spin- labelled HFB2 recorded in water at 20 °C	4–90

Figure 41 Normalized cwEPR spectra of POPC vesicles with varying amounts of spin-labelled HFB2 recorded in water at 20 °C.....	4–90
Figure 42 The three main fields of hydrophobin self-assembly and interactions elaborated upon in this thesis	5–97
Table A - 1 Constituents of liquid culture medium for <i>S. commune</i>	i
Table A - 2 composition of medium for agar plate cultures of <i>S. commune</i>	ii
Table A - 3 composition of minimal medium for liquid cultures of <i>S. commune</i>	ii
Table A - 4 composition of the trace element solution	ii
Table A - 5 Buffer composition for Laemmli-PAGE	iii
Table A - 6 Buffer composition for Tricine-PAGE	iii
Table A - 7 stock solutions used for vesicle preparations.....	iv
Figure B - 1 cwEPR spectra of POPC:PDSPC vesicles (5:1) recorded in water at 20 °C. ...	iv
Figure B - 2 Saturation curve for pure POPC: PDSPC vesicles (50:1) recorded at 20°C	v
Figure B - 3 Saturation curve for POPC: PDSPC vesicles with SC3 (50:1:7) recorded at 20°C.....	v
Figure B - 4 Saturation curve for POPC: PDSPC vesicles with HFB2 (50:1:14) recorded at 20°C.....	vi

1. HYDROPHOBINS – CONTEXT AND BACKGROUND

Hydrophobins are a large family of small amphipathic, cysteine rich proteins exclusively produced by filamentous fungi. Their amphiphilic nature allows for their spontaneous self-assembly into a multitude of insoluble films and structures at hydrophilic/hydrophobic interfaces. Originally discovered in the study of highly expressed genes during the formation of fruiting bodies, their involvement in a great variety of stages and processes during the fungal lifecycle has been observed or suggested in the past decades. The following chapter presents results of the earliest studies on the nature and roles of hydrophobins and the structural foundation for their self-assembly and provides some context for the scientific questions and approaches that arise from preliminary studies and/or remain largely unanswered to this day. Furthermore, the motivation and general strategy of the work presented here will be given and discussed at the end of this chapter.

1.1 *STRUCTURE, CLASSIFICATION AND ROLES*

The first genes encoding hydrophobins were found in a search for abundantly expressed genes in the split gill fungus *Schizophyllum commune* by WESSELS and co-workers. Based on the deduced sequence the term *hydrophobin*, a name earlier used for any hydrophobic substance covering microbial cells, was coined specifically for these small (around 100 amino acids), moderately hydrophobic proteins identified in the hyphal walls of aerial structures in this particular fungus. [DONS, J. J., SPRINGER, J. *ET AL.* 1984]

Since then, a number of genes abundantly expressed by other fungi have been identified as hydrophobins by sequence comparison. The main unifying feature was found to be the presence of eight Cys residues with a particular occurrence in the sequence, namely the second and third as well as the sixth and seventh cysteine always being immediate neighbours. [SCHUREN, F. H. J. AND WESSELS, J. G. H. 1990]

All eight cysteines are assumed to be linked in a specific pattern of disulfide bridges, which connect C1-C6, C2-C5, C3-C4 and C7-C8.

[HAKANPÄÄ, J., PAANANEN, A. *ET AL.* 2004; KWAN *ET AL.* 2006] These cysteines are, at least for class I hydrophobin SC3, essential for retaining a soluble monomeric form in solution, but not directly involved in interfacial self-assembly. [DE VOCHT, M. L., REVIKINE, I. *ET AL.* 2000] Hydrophobins generally contain a four-stranded β -barrel core. This basic fold can be found in virtually all hydrophobins and usually contains a large portion of the hydrophobic amino acids.

Subsequently, it was discovered that different hydrophobins are expressed at different stages of the fungal lifecycle and can be attributed to different processes such as the formation of aerial structures, interactions of pathogenic fungi with host organisms [TALBOT, N. J., KERSHAW, M. J. *ET AL.* 1996; EBBOLE, D. J. 1997; HOLDER, D. J. AND KEYHANI, N. O. 2005; WÖSTEN, H. A. B. AND WESSELS, J. G. H. 1997; RAMBACH, G., BLUM, G. *ET AL.* 2015] and the coating of surfaces and air cavities in fruiting bodies, to give a few examples.

(see DE GROOT, P. W. J., SCHAAP, P. J. *ET AL.* 1996; MULDER, G. H. AND WESSELS, J. G. H. 1986; WESSELS, J. G. H., DE VRIES, O. M. H. *ET AL.* 1991; WESSELS, J. G. H., DE VRIES, O. M. H. *ET AL.* 1991B; WÖSTEN, H. A. B., ASGEIRSDOTTIR, S. A. *ET AL.* 1994 for detailed information)

Based on hydropathy patterns of several hydrophobins WESSELS and co-workers proposed their classification into two groups, dubbed class I and class II, and predicted the solubility of their respective members' primary aggregates.

(see WESSELS, J. G. H. 1994)

The amino acid sequences of class I hydrophobins are diverse, with relatively large and varying intercysteine spacing, while class II hydrophobins are more homologous. [REN, Q., KWAN, A. H. AND SUNDE 2013]

While both classes initially form closed surface membranes, the ultimate morphologies differ considerably.

Members of class I tend to form fibrous aggregates that are highly insoluble in aqueous solution, even withstanding 2% sodium dodecyl sulphate (**SDS**) at 100 °C and can only be dissociated in formic acid (**FA**) or trifluoroacetic acid (**TFA**). The findings of DE VRIES and co-workers also showed that non-covalent interactions rather than intermolecular disulfide bridges are responsible for the aggregation. [DE VRIES, O. M. H., FEKKES, M. P. *ET AL.* 1993]

It was found that the self-assembly of SC3 into rodlets proceeds via intermediate α -helical and β -sheet states. [DE VOCHT, M. L., REVIKINE, I. *ET AL.* 2002] These fibres are very similar to amyloids. [SUNDE, M., KWAN, A. H. *ET AL.* 2008] They are straight, unbranched and bind standard chromophores used in amyloid research, such as thioflavin T and Congo Red. X-ray diffraction data shows, however, that hydrophobin fibres exhibit the characteristic reflection for β -sheets while lacking the one attributed to stacked cross-beta structures found in “conventional” amyloids. This suggested that the mechanism of fibre formation differs considerably from classical amyloidogenic compounds such as A β -peptides.

Based on these observations, a model was proposed for the formation of fibres in class I hydrophobin EAS that involves the unstructured loops on both ends of the β -barrel that “add on” to said barrel by forming additional β -structures.

[KWAN *ET AL.* 2006]

On the other hand, structures formed by class II hydrophobins may generally be solubilized in aqueous dilutions of organic solvents or SDS [WÖSTEN, H. A. B. AND DE VOCHT, M. L. 2000] and lack fibrillary morphology.

These films are often highly crystalline, but can be distinctly different between individual hydrophobins within this class and even originating from the same organism. Contrary to the multitude of intermediate structures, the membranes seem to form spontaneously at hydrophilic/hydrophobic interfaces in a highly ordered manner.

Class II hydrophobins HFB1 and HFB2, both from *T. reesei*, appear to exist in various stages of aggregation in solution, i.e. dimers or monomers at low and tetramers at higher concentrations for HFB2 and even larger oligomers for HFB1. Class II hydrophobins tend to be more rigid with a distinct spatial separation of hydrophilic and hydrophobic regions. Combined with the relatively large size compared to “generic” surfactants, this feature might explain the regular well-organized nature of the resulting membranes, since it allows for rigid building blocks large enough to make favourable intermolecular contacts, whereas unstructured flexible loop-regions seem to be the key factor in the fibrillation of class I members. [HAKANPÄÄ, J., PAANANEN, A. *ET AL.* 2004]

Although this prediction of aggregate properties has been remarkably accurate so far, its biological significance remains largely unclear. In 2011, SEIDL-SEIBOTH and

colleagues presented a novel set of hydrophobins that deviate from the established classification in hydrophathy, cysteine spacing and protein surface patterns. [SEIDL-SEIBOTH, V., GRUBER, S. *ET AL.* 2011] Since then several hydrophobins have been described that may form subgroups within this broader classification.

At the scale of microorganisms interfacial phenomena are the dominant forces while large-scale interactions like gravity are essentially inconsequential. The surface tension of water, for example, is a very strong force on a molecular to micro-metre scale and can easily overcome gravity or buoyancy. Most biological functions of hydrophobins seem to be linked to controlling these interfacial interactions. The excretion of hydrophobins into the aqueous surroundings of the fungus and their subsequent assembly at the water surface lowers the surface tension to allow the growth of areal hyphae. Hydrophobin layers prevent water-logging, e.g. in fruiting bodies, while maintaining permeability to gas exchange. [WANG, X., SHI, F. *ET AL.* 2005; LUGONES, L., BOSSCHER, J. S. *ET AL.* 1996] Hydrophobin RodA from *Aspergillus fumigatus* has been shown to protect spores from recognition by host defence mechanisms. [AIMANIANDA, V., BAYRY, J. *ET AL.* 2009] Besides pathogenic interactions, hydrophobins have also been discussed in the context of symbiotic relationships. [HONEGGER, R. 1991; TAGU, D., DE BELLIS, R. *ET AL.* 2001]

This multitude of crucial roles during the fungal lifecycle has inspired a quite imaginative discussion of potential applications in numerous fields. Some of these applications, recent developments and arising challenges will be discussed in the following section.

1.2 APPLICATION POTENTIAL AND SCIENTIFIC CHALLENGES

The tendency of hydrophobins to form amphipathic layers entails the ability to deposit on either side of a hydrophilic/hydrophobic boundary. This has the effect of reversing that wettability of the surface in question. Thus, hydrophobins have been proposed as coating agents in biomedical and biotechnological applications; for example as anti-fouling agents [LIU, Y., NEVANEN, T. K. *ET AL.* 2019; HEKTOR, H. J. AND SCHOLTMEIJER, K. 2005] or cell growth on hydrophobic solids. [JANSSEN, M. I., VAN LEEUWEN, M. B. M. *ET AL.* 2002] A major advantage of utilizing proteins for

this purpose is their biocompatibility and degradability. Moreover, genetic modification of the sequence, post-translational modification or the subsequent attachment of ligands onto specific amino acids would arguably allow for precise fine-tuning of the surface properties.

Potential examples of hydrophobin application are the coating of nanodevices and medical implants to improve biocompatibility, as emulsifiers in the food and cosmetics industries and as foam stabilizers and nanomaterial design.

[DE STEFANO, L., REA, I. *ET AL.* 2009; HEINONEN, H., LAAKSONEN, P. *ET AL.* 2014]

On the other hand, the presence of hydrophobins in carbonated beverages such as beer and cider can induce gushing, i.e. the vigorous foaming of the beverage even without prior shaking. Described by LINDER as “[...] a phenomenon where beer foam gushes out of the bottle [...], almost emptying it even if it has not been shaken before.” [LINDER, M. B. 2009] such products cannot be sold to consumers and therefore pose a significant economic risk to producers. [KHALESI, M., DECKERS, S. M. *ET AL.* 2012] Studies indicate that this particular phenomenon might be more related to class II rather than class I hydrophobins. [LINDER, M. B., SZILVAY, G. R. *ET AL.* 2005; POSTULKOVA, M., RIVEROS-GALAN, D. *ET AL.* 2016]

As mentioned in the previous section, class I hydrophobins assemble into stable rodlets which share many structural similarities with amyloids. They are unbranching and straight, rich in cross- β structures and bind the dyes thioflavin T and Congo Red, resulting in enhanced fluorescence and green-gold birefringence, respectively. [BAYRY, J., AIMANIANDA, V. *ET AL.* 2012] Amyloids are directly linked to a number of neurodegenerative diseases, such as Alzheimer’s or Parkinson’s disease. However, it was shown that amyloid fibril formation not necessarily results in toxic aggregates but can provide biologically functional structures.

[GEBBINK, M. F., CLAESSEN, D. *ET AL.* 2005]

Although hydrophobins are generally considered non-toxic for humans, the structural similarities might be of interest for foundational studies on the mechanics of fibrillation, stability and interactions with other biological units such as cell membranes and liposomes. All of the aforementioned potential applications, as well as challenges for feasible production levels, rely on a better understanding of the self-assembly mechanisms at work. This should allow for precise fine-tuning of their

interactions, both among themselves and with other compounds at various interfaces and in solution. Based on a recent advances in our understanding of their interfacial behaviour and properties, a number of scientific questions need to be addressed.

The first part of this work elaborates on various aspects of structure formation of class I SC3 from *Schizophyllum commune* and class II HFB2 from *Trichoderma reesei* at the air/water interface. Since hydrophobins are primarily involved in interfacial phenomena, especially the water surface of aqueous environments the respective fungi typically inhabit, this is an intuitive starting point for the second major topic of this thesis, which deals with their interactions with phospholipid vesicles as a model system for cell membranes and confined interfaces in solution.

The main questions that will be addressed are:

- What large-scale (i.e. several micrometres up to several hundred micrometres) structures are formed at the air/water interface?
- What is the effect of areal constraints on these structures? Most importantly, how do multiple compressions and expansions and subsequent transfer to solid substrates affect the interfacial structures?
- How do both proteins interact with phospholipid vesicles as a simple model for cell membranes?
- What is the difference between both proteins in these contexts? Can these differences be explained by the currently accepted defining features of the two classes?

2. THEORETICAL BACKGROUND AND EXPERIMENTAL PARAMETERS

The scientific questions addressed in this work all revolve around the central issue of a coherent understanding of hydrophobin self-assembly, the detailed mechanisms at work and, consequently, their structure function relations.

Feasible approaches to specific questions, however, differ greatly in their potential to elucidate structures on any given scale, monitor interactions between proteins and other compounds and even their applicability for different hydrophobins.

The following chapter provides introductions, theoretical considerations and practical aspects of the experimental techniques utilized in this work. Specific goals or questions sought to be achieved or answered will also be given with every technique.

2.1 PROTEIN PRODUCTION AND PURIFICATION

Class I hydrophobin SC3 was extracted from the cultural medium of *S. commune*. Both liquid medium and agar plates were utilized, because the fungal culture has a longer shelf life and changes in the morphology are better visible on agar plates, but secretion of the protein mainly occurs in liquid medium. The composition of both media is listed in the Appendix.

Agar plates were incubated aerobically for seven days at room temperature and are subsequently storable for up to one month in the fridge. Liquid medium was then inoculated with fungus from these agar plates.

Liquid medium cultures were incubated aerobically for 14 days at 24 °C on a shaker running at 350 rounds per minute.

Extraction of the protein was achieved in a two-step process. Firstly, coarse fungal matter was removed from the liquid by sifting. When needed, the highly viscous medium could be diluted with isotonic sodium chloride solution. The use of pure water is discouraged to avoid bursting of the mycelia due to osmotic pressure.

The liquid culture was subsequently centrifuged at 4 °C and 3220g for four hours.

SC3 has a high affinity to hydrophilic/hydrophobic interfaces and thus readily assembles around gas bubbles. Protein coated gas vesicles then float to the surface, where they form a stable foam that can easily be collected. While blowing nitrogen or hydrogen gas into the medium would work in principle, hydrogen bubbles generated *in situ* are smaller and can be distributed more evenly with a magnetic stirrer. In the second stage the medium was thus subjected to electrolysis at 300 mA direct current for up to 11 hours, until no more stable foam was formed.

The cathode was kept deep in the liquid medium, while the anode was submerged in sodium bicarbonate solution, separated by a salt bridge containing 1 M potassium chloride solution. The collected foam was then flash-frozen in liquid nitrogen and lyophilized overnight. The freeze dried protein can be stored in the fridge for several months.

Finally, the lyophilisate was washed in 60 % ethanol. After centrifugation at 3220g for two minutes, any precipitate formed was discarded and the ethanol was removed in a stream of nitrogen.

The protein was analysed by SDS-PAGE and silver staining. The buffer composition for the Laemmli-PAGE can be found in the appendix.

2.1.1 DEGLYCOSYLATION OF SC3

SC3 is one of only two hydrophobins that are proven to be glycosylated at the N-terminus. DE VOCHT *et al.* could show that SC3 carries an average of 20-24 Manose units, presumably bound to several threonine and a serine moieties. [DE VOCHT, M. L., SCHOLTMEIJER, K. *ET AL.* 1998] The biological significance and the exact influence on structure formation are yet unknown. After verification of the glycosylation state by mass spectrometry the removal of all sugars was attempted using trifluoromethanesulfonic acid (TFMSA). In a water-free environment containing anisole solvolysis of the O-glycosidic bonds by TFMSA generally leaves the protein intact. Anisole acts as a scavenger, stabilizing intermediate radicals and quenching reactive electrophilic intermediates, which could lead to undesired side reactions involving tryptophane, cysteine, methionine, serine and threonine moieties within the protein.

This wet chemical approach was chosen over enzymatic reactions for a number of reasons. Firstly, deglycosylation by TFMSA is unspecific and should cleave all glycosidic bonds. This can often only be achieved by a mixture of several enzymes, because the spatial accessibility of the sugars may vary. Secondly, there is only a small number of enzymes suited for cleaving O-glycosidic bonds; and none could be found that were successfully tested on fungal proteins. Lastly, purification of the protein is challenging due to its amphipathic nature, which causes it to adhere to the walls of common purification or concentration columns. The self-assembly leads to multimers in solution. The mass of these multimers likely approach that of a typical enzyme (e.g. 52 kDa for PNGase A), further complicating separation of the protein from all other reactants.

Experimental parameters. The applied procedure is based on the *GlycoProfile*TM, *Chemical Deglycosylation Kit* by Sigma Aldrich. All utilized compounds are listed in Table 1.

Table 1 Reagents for the deglycosylation of SC3

Compound	Supplier	CAS-No.
Anisole	Sigma Aldrich	100-66-3
Bromophenol blue	Carl Roth GmbH	115-39-9
Ethanol	Carl Roth GmbH	64-17-5
Pyridine	Carl Roth GmbH	110-86-1
Trifluoromethane-sulfonic acid	Sigma-Aldrich	1493-13-6

The protein was freeze-dried overnight to remove all residual moisture. All containers are flushed with argon and kept on ice; 150 μ L of a mixture of TFMSA and Anisole (1:10 v/v) per 1 mg of protein are slowly added and the resulting solution is kept on ice for three hours under gentle stirring.

After this two drops of a 0.2% solution of Bromophenol blue in Ethanol are added; the mixture turns deeply red. The reaction is stopped by addition of 60% Pyridine until the mixture turns green.

Purification of the final product was achieved by triple extraction with Diethyl ether, discarding the organic phase. The aqueous phase is dialysed overnight against

water in a dialysis tube with a molecular weight cut-off (**MWCO**) of 5000 Da. Finally, the protein was lyophilized again to ensure storage stability. Details on the Tris-PAGE procedure can be found in the appendix.

2.2 SURFACE TENSION AND MONOLAYERS

Monolayers (sometimes also called *monomolecular films*) are quasi-two-dimensional layers of monomolecular thickness. Two general types of interfacial layers can be distinguished:

Adsorption layers (Gibbs monolayers), which form by migration to the interface from inside the volume phase and in which equilibrium between volume phase and interfacial phase is established; and *insoluble layers (Langmuir monolayers)*, that form on a liquid surface by spreading from a volume phase, i.e. a spreading solution, liquid or solid body. In the latter case, no equilibrium is reached between volume phase and interface. Hence, a portion of the spread molecules (e.g. lipids) are driven to desorb into the subphase. This diffusion is governed by the solubility of the substance spread (carboxylic acids, phospholipids, amines, etc.), e.g. chain length or size and charge of the head group. They are called *insoluble* because the vast majority of molecules do not dissolve into the subphase.

The driving force behind the formation of a Langmuir monolayer is the *equilibrium spreading pressure* Π_e , which describes the difference in surface tensions between the film-carrying substrate (mostly water or other polar liquids; but also solid bodies) σ_{lg}^1 and the sum of the spreading liquids surface tension σ_{lg}^2 and the interfacial tension of the newly formed substrate/spreading liquid interface σ_{ll} .

$$\Pi_e = \sigma_{lg}^1 - (\sigma_{lg}^2 + \sigma_{ll}) \quad \text{Eq. 1}$$

Its dimension is $\frac{[energy]}{[area]} = mN/m$.

According to Eq. 1 spreading occurs when the numerical value of the spreading pressure is *positive*, because in that case the systems gains work.

Therefore, liquids and solids with high values for σ_{lg}^1 are very well suited as substrate for spreading, e.g. water ($\sigma_{lg} \approx 72 \text{ mN/m}$) or mercury ($\sigma_{lg} \approx 460 \text{ mN/m}$).

[Dörfler, H.-D. 2002; PP 99-101]

2.2.1 FILM BALANCE MEASUREMENTS

Monolayers can be studied at the air/water interface using film balances. Specifically, the compression behaviour of the monolayers is monitored. A film balance consists of a trough filled with the subphase liquid, usually made of Teflon, a Wilhelmy-system to measure surface pressure and might have movable barriers to control the surface area. A schematic representation is shown alongside two methods of film transfer in Figure 2.

The resulting dataset consists of the measured *surface pressure* Π , defined as the difference in surface tension between the pure subphase (most commonly water) and the film-carrying surface, and the area per molecule, and is referred to as *compression isotherm* or Π -A-isotherm, with Π and A referring to the surface pressure and molecular area, respectively.

The shape of the isotherm often contains valuable information on the packing of the amphiphiles in the monolayer and phase behaviour in a fashion analogous to three-dimensional phases, i.e. solid bodies or liquids. Figure 1 illustrates a typical Π -A-isotherm of a lipid monolayer. The different phases are named in analogy to their three-dimensional counterparts. Just as is the case in three dimensional phases, the existence of any given phase is dependent on a number of parameters, most notably temperature, subphase composition, pH, ionic strength and, of course, the exact nature of the amphiphile. This “classical” distinction of phases rarely occurs when studying proteins and can be mostly attributed to the organization of alkyl chains in lipids. Nonetheless, break points can occur and provide information on changes in the compressibility of the monolayer.

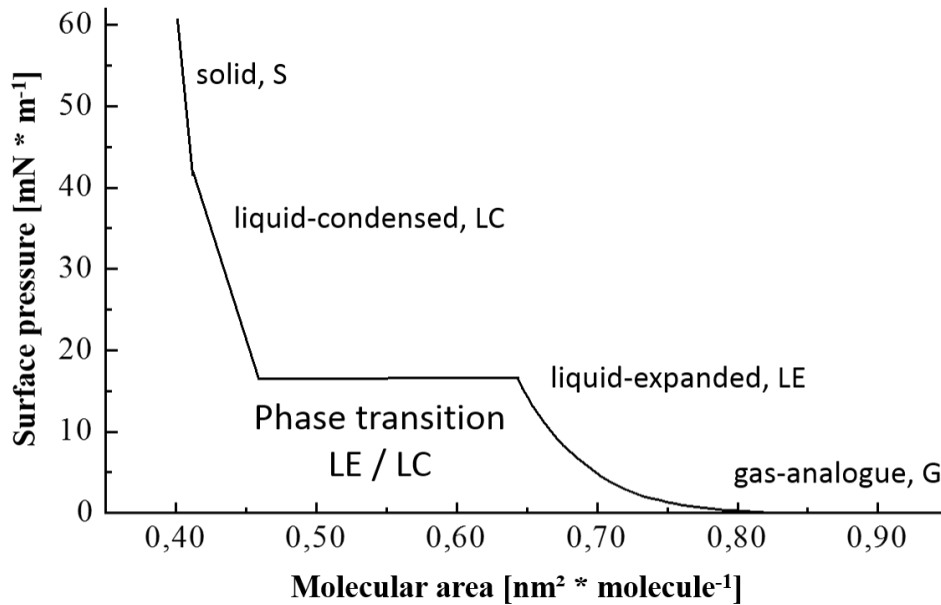


Figure 1 Exemplary isotherm of a phospholipid monolayer exhibiting multiple phases taken from: **Dörfler, H.-D., 2002; pp. 103 ff**

To investigate the interfacial morphology on a micrometre scale the films can be transferred onto a solid substrate, allowing for AFM imaging. The most common techniques are the *Langmuir-Blodgett (LB)* and *Langmuir-Schaefer (LS)* transfer methods. In the former the solid substrate is submersed in the subphase vertical to the interface and pulled upward through the film. This causes the hydrophilic side of the sample to connect with the substrate and allows for imaging of the hydrophobic side. In the latter technique the substrate is placed parallel to the interface and the film is “stamped off”, which exposes the hydrophilic part.

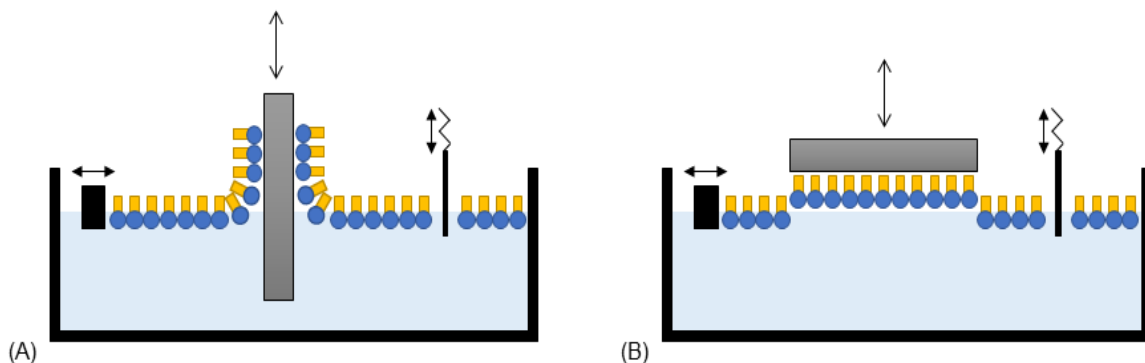


Figure 2 Schematic depiction of transfer methods. (A) *Langmuir-Blodgett*; (B) *Langmuir-Schaefer*. Courtesy of M. Kampe.

LS-transfer was utilized to gather the protein films on freshly cleaved mica and subsequent analysis in tapping mode atomic force microscopy. A detailed description can be found in section 2.3.

In order to get a more detailed view of ordering processes directly at the interface the application of spectroscopic or optical methods is advisable. One such technique will be discussed in the following section.

2.2.2 EPI-FLUORESCENCE MICROSCOPY

The coupling of monolayer techniques with optical or spectroscopic methods provides powerful means to visualize differences of packing density, molecular short- and long-range ordering and molecular orientation with respect to the surface. At the same time, however, achieving the contrast necessary may require the addition of sensitive molecules, such as chromophores, which may influence the interfacial behaviour of the studied system. Epi-fluorescence microscopy is a technique coupling a film balance system with an optical microscope that relies on fluorescence emission. The addition of a fluorophore may take place in the subphase or within the monolayer. In the study of lipid monolayers at the air/water interface, fluorescently tagged lipids have been used with enormous success since the introduction of the technique in the early eighties. They provide contrast upon their segregation between phases due to differences in local molecular organization, resulting in different fluorescence emission properties. However, like many other lipids, they are effectively insoluble in the aqueous subphase and are therefore trapped in the interfacial layer.

Consequently, expelling them from one phase also means concentrating them in another, which can lead to fluorescence quenching, alterations in the structure of all regions involved or perturbations in the mechanical properties of the layer.

[CHOI, S. Q., STELTENKAMP, S. *ET AL.* 2011] Obviously, since they are phospholipids, they also constitute foreign molecules in the study of other surface active compounds such as hydrophobins.

The alternative is to introduce the fluorophore into the subphase. Contrast is achieved by the selective adsorption of a water-soluble dye from the subphase to the monolayer. Several factors have to be taken into consideration for this approach:

1) In conventional wide-field microscopy, fluorescence from the subphase and the interface cannot be distinguished. Nonetheless, ‘lateral’ contrast is achieved by differential adsorption of the dye to regions of different packing density within the monolayer.

2) If the dye adsorbs to the air/water interface, changes in the physical properties of the monolayer are inevitable. Ensuring only negligible influence of the dye on the studied monolayer by control experiments and comparison to other systems (e.g. different fluorophores) thus are essential.

3) The quantum efficiency of the dye needs to be high enough to justify only minute concentrations in the subphase. This is critical for the comparability of the experiment with regards to subphase composition.

Experimental parameters. The full isotherms were recorded on a single-barrier Teflon trough of 4.71 and 22.43 cm² minimal and maximal surface area, respectively, equipped with an R&K controller and software (Riegler & Kirstein GmbH Potsdam, Germany). Purified water (Milli-Q) was used as subphase for the recording of the isotherms and LS-transfer, and solutions of Rh123 (15 nM) and bis-ANS (0.2 μM) in purified water served as subphase for epi-fluorescence microscopy. The temperature was kept constant at (20±0.5) °C, and the compression speed was 2 Å² (molecule*min)⁻¹ in all cases. 40 μg samples of protein in chloroform (SC3) or water (HFB2) were deposited on the surface and allowed to stabilize for 15 minutes (SC3) or 1.5 h (HFB2) before compression began. Pieces of filtering paper served as Wilhelmy plate to continuously record the surface pressure. Fluorescence microscopy imaging of the interface was performed with an Axio Scope A.1 Vario epifluorescence microscope (Carl Zeiss MicroImaging GmbH, Jena, Germany), equipped with an LD EC Epiplan-NEOFLUAR objective (50x magnification). A 100 W mercury arc lamp served as illumination source; respective wavelengths were selected with a filter/beam splitter combination suited for the chosen dye. [FS 81 HE; Wheel 484/25 for Rh123; FS 81 HE; Wheel 375/38 for bis-ANS]. Images were recorded with the AxioVision software v. 4.8.2.0 (Zeiss).

2.3 ATOMIC FORCE MICROSCOPY (AFM)

Apart from spectroscopic methods, imaging techniques provide detailed insight into the morphology of self-assembled structures on varying length scales, from a few nanometres up to several microns. AFM was utilized to investigate the three-dimensional topology of LS-transferred films from the air/water interface onto mica. The major strength of this technique lies in the simplicity of sample preparation and the ability to measure virtually any surface of any sample under ambient conditions with no need for ultra-high vacuum or inert gas atmospheres.

Of the three major operating modes commonly utilized in AFM experimentation (*contact*, *non-contact* and *tapping mode*), the principle of *tapping mode AFM* and its application for hydrophobin films will be described briefly in this section.

Figure 3 shows the general setup of an AFM instrument.

In *tapping mode AFM* the tip positioned on a flexible cantilever is excited to vibrate near the cantilevers resonance frequency by a Piezo element. At every oscillation minimum the tip comes into contact with the sample, before retreating again.

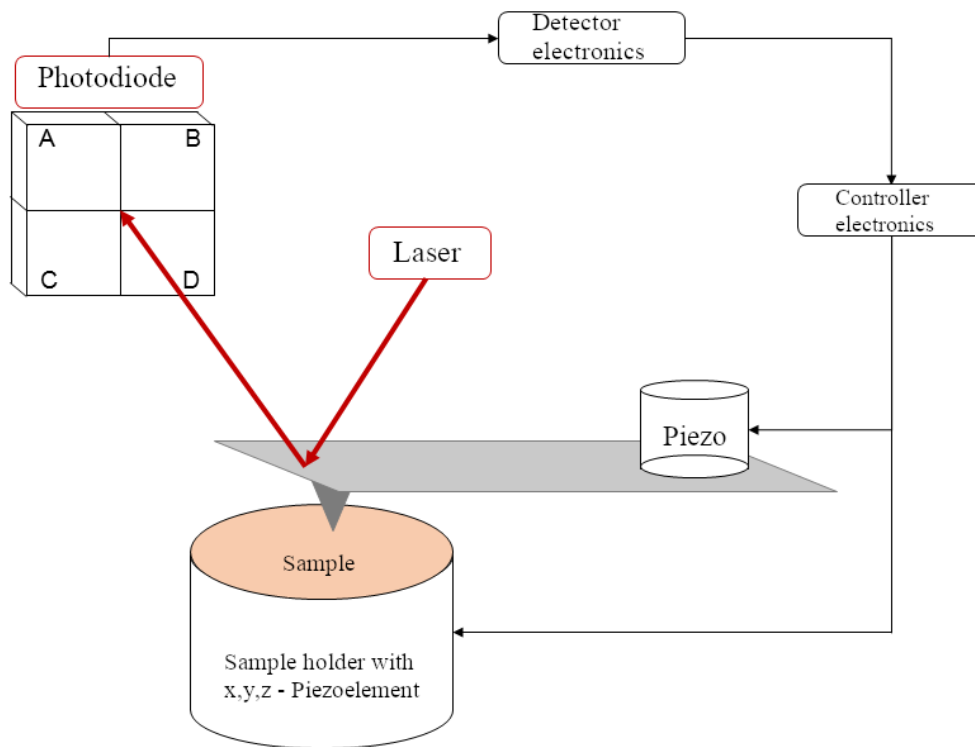


Figure 3 General setup and measurement principle of the atomic force microscope. Courtesy of M. Kampe.

The deflection of the laser across the sectioned photodiode serves as the main feedback for the generation of height images.

When directly in contact with the sample surface repulsive electron-electron interactions are the dominating force. During approach to and retreat from the sample attractive van-der-Waals interactions dominate. A major advantage of this operating mode over the other two is the fact that the force onto the tip acts perpendicular to the sample surface and not in the direction of scanning. Thus there is less drag and smearing of the sample and contamination of the tip, which is important in the imaging of soft matter. Furthermore, the setup allows for the simultaneous recording of different datasets that contain multifarious information.

The height image depicts the three-dimensional topology of the sample. Amplitude Error images are equivalent to a “map” of the slope of the sample and contain information on its shape. Lastly, phase images show the discrepancy in phase between the excited and momentary vibration of the cantilever. The phase shift is caused by interactions between tip and sample and depends on instrumental parameters (i.e.

shape and force constant of the tip and cantilever), but also on viscoelastic properties of the sample. Therefore, phase images allow for the distinction of different sample components even if they are of the same height.

Experimental parameters. Freshly cleaved mica was rinsed with ethanol and briefly blow-dried with pressurized air directly before LS-transfer with a Filmlift FL-1 (MGW Lauda). The substrate was fixed to a magnetic plate by double-sided adhesive tape and magnetically attached to the Filmlift instrument. Lifting of the interfacial film occurred with an approach speed of 25 cm per minute. After 24 s of contact between the mica and the interface the substrate was lifted again at a speed of 30 cm per minute. All samples were then dried in a desiccator for 48 hours before AFM imaging.

The atomic force microscopy was performed on a Multimode AFM (Veeco Instruments Inc., New York) equipped with Tapping Mode cantilevers (BudgetSensors® Innovative Solutions Bulgaria Ltd., Bulgaria) with a spring constant of 5 N/m, a nominal resonance frequency of 150 kHz and a denoted tip radius of < 10 nm. On average, three scans were recorded over the chosen sample region at a scanning rate of 0.5 Hz with a ratio of set-point amplitude to free amplitude of ≈ 0.8 . Similar structures were observed over an average of four different regions of each sample, ensuring the reproducibility of all results.

All images were recorded with the NanoScope software (v. 7.30, Veeco) and processed using the freeware Gwyddion 2.49.

The AFM micrographs were plane levelled and fixed to zero before surface coverage was calculated. The limit for protein signal was chosen at 0.5 nm, meaning that anything above the muscovite surface plus a correction of 0.5 nm was taken as protein film to determine height and coverage.

The height distribution densities were calculated as noncumulative functions in Gwyddion. A gauss 2 fit was utilized to determine the full width at half maximum (**FWHM**) according to the following equation:

$$f(x) = a_1 * \exp\left(-\left(\frac{(x - b_1)}{c_1}\right)^2\right) + a_2 * \exp\left(-\left(\frac{(x - b_2)}{c_2}\right)^2\right) \quad \text{Eq. 2}$$

With the parameters c_1 and c_2 the FWHM can be calculated according to

$$FWHM_i = 2 * \sqrt{2 * \ln(2)} * c_i / \sqrt{2} \quad \text{Eq. 3}$$

2.4 DYNAMIC LIGHT SCATTERING (DLS)

Dynamic Light Scattering (**DLS**) is a powerful tool to determine the size, size distribution and, to some extent, shape of nanoparticle dispersions *in situ*.

Temporal fluctuations of the interparticular interference and intensity of a scattered light beam, caused by Brownian motion of particles in a dispersion, allow for the determination of the translational diffusion coefficient and the hydrodynamic radius or diameter of said particles.

Since molecular motion is much slower than the speed of light, however, frequency shifts due to the Doppler Effect are minute and analysis utilizing an interferometer is inopportune. Instead, the recorded intensity fluctuations of the scattered light beam are transformed to so-called autocorrelation functions to derive the mentioned parameters of interest. The measured intensity $I(t)$ can be described as noise with a fluctuation period oscillating around a mean intensity $\langle I \rangle$. The autocorrelation function is obtained by comparing the intensity at time t with the intensity at the time $t + \tau$. At very small values for the correlation time τ the scattering particles are very similar in position and momentum, hence the measured values for $I(t)$ and $I(t + \tau)$ correlate strongly.

With increasing time intervals the similarity of motion, and thus correlation, are lost. Large particles diffuse slower than small ones; therefore correlation persists for a longer time the larger the observed particle is. The fluctuation of the measured intensity over time is schematically depicted in Figure 4.

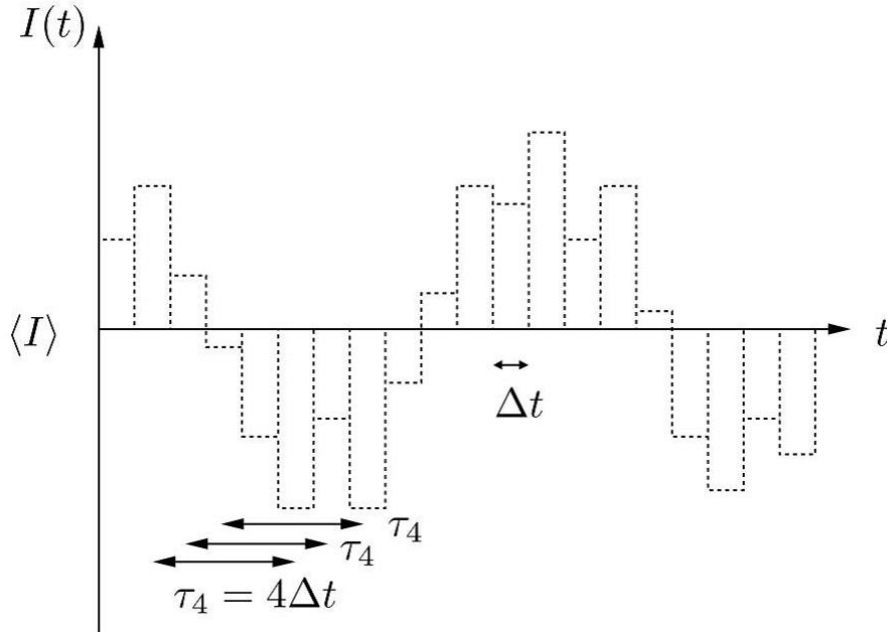


Figure 4 Temporal intensity fluctuation. (measuring interval Δt is small compared to fluctuating time) adapted from: **EISERMANN, J. 2017**

The resulting normalized *intensity time correlation function*

$$g_2(\tau) = \frac{\langle I(t) \cdot I(t + \tau) \rangle}{\langle I(t) \rangle^2} \quad \text{Eq. 4}$$

is related to the scattered *field time correlation function* g_1 by the **Siegert-relation**

$$g_2(\tau) = 1 + |g_1(\tau)|^2 \quad \text{Eq. 5}$$

It represents an exponential decaying function of the correlation time for monodisperse particles in Brownian motion that can be expressed as:

$$g_2(\tau) = A[1 + B \exp(-2\tau\Gamma)] \quad \text{Eq. 6}$$

Here, **A** is the baseline of the correlation function and **B** is the intercept.

$\Gamma = D_s q^2$ is the decay constant, wherein **D_s** is the translational diffusion coefficient and **q** is the wave vector containing information about the sample and setup:

$$\mathbf{q} = \left(\frac{4 \pi n}{\lambda_0} \right) \sin \left(\frac{\Theta}{2} \right) \quad \text{Eq. 7}$$

with the refractive index of the dispersant n , the laser's wavelength λ_0 and the scattering angle Θ . For polydisperse samples the autocorrelation function contains the integral sum of all exponential decays $g_1(\tau)$ and is generally expressed as:

$$g_2(\tau) = A[1 + B g_1(\tau)^2] \quad \text{Eq. 8}$$

The translational diffusion coefficient D_s contained in the parameter Γ for all decays is related to the hydrodynamic radius R_H by the Stokes-Einstein equation:

$$D_s = \frac{kT}{f} = \frac{kT}{6 \pi \eta R_H} \quad \text{Eq. 9}$$

where k is the Boltzmann constant, T is the absolute temperature, η is the medium viscosity and f is the frictional coefficient for a hard sphere in a viscous medium. Therefore, by definition, the radius measured in DLS is the radius of a hypothetical hard sphere that diffuses with the same speed as the examined particle. Since hypothetical hard spheres are non-existent (as the name implies) and many particles, especially macromolecules in solution, are non-spherical, dynamic (i.e. *tumbling*) and solvated, the radius calculated from the diffusional properties indicates the *apparent* size of the solvated, dynamic particle.

Automated data processing allows for the extraction of several relevant parameters aside from the hydrodynamic radius, most importantly the mean *decay constant* $\bar{\Gamma}$ and the polydispersity index (**PDI**). As mentioned above, $g_1(\tau)$ is the integral sum of all exponential decay curves. Fitting by the measurement software is accomplished by reconstructing the function using a so-called cumulant expansion, an ISO-standardized procedure, approximating the integral as a sum that is solved by a power series expansion of Eq. 8, resulting in a simple polynomial given by:

$$\ln \left[\frac{g_2(\tau) - A}{A} \right] = \ln B - 2\tau\bar{\Gamma} + K_2^2\tau^2 \quad \text{Eq. 10}$$

By changing the parameters B, K_2^2 and $\bar{\Gamma}$ the best possible match with an ISO-conform cumulant algorithm is approached. From those fitting parameters the PDI is directly accessible according to the equation:

$$PDI = \frac{K_2}{\bar{\Gamma}} \quad \text{Eq. 11}$$

The PDI is a measure of the size distribution's width. In essence, the cumulant fit calculates a decay constant of the intensity correlation function to derive the particle size and polydispersity.

Experimental parameters. DLS was performed on a Litesizer™ 500 (Anton Paar GmbH, Graz, Austria) in a low-volume cell at 20 °C. The setup irradiates the sample with a 40 mW semiconductor laser at a wavelength of $\lambda_0 = 658$ nm and offers three different detection angles, namely *back* (175 °), *side* (90 °) and *forward* (15 °). 80 μ L of freshly prepared aqueous solutions of the respective material were inserted into the cell and allowed to equilibrate for two minutes before measurement. At scanning times of 10 seconds a total of 20 scans was recorded for each sample and data processing was done by the dedicated software Kalliope™.

2.5 ELECTRON PARAMAGNETIC RESONANCE SPECTROSCOPY (EPR)

The phenomenon of EPR is based on the absorption of electromagnetic radiation by magnetic dipoles, in this case unpaired electrons, in a sample. The common frequency range in EPR lies in the region of Terahertz and microwave radiation, between 10^9 to 10^{12} Hz. The fundamental drawback is the requirement of a paramagnetic species, i.e. an electron system with a non-zero net angular momentum. Typical systems to be measured include several transition metal ions, ‘point’ defects in solids, triplet state systems and compounds with conducting electrons, and free radicals. The latter is of special interest in biological systems, because a great number of artificially stabilized radicals, mostly based on nitroxides, is commercially available for a great number of applications. With the introduction of a stable unpaired electron into the system, the explicit nature of the sample (e.g. crude oil or purified protein) is of no major importance, at least in principle.

The absorption of microwave radiation is based on the *Zeeman* – Effect. The degenerate energy levels of the paramagnetic centre (e^-) of spin $s = \frac{1}{2}$ are split in an external magnetic field \mathbf{B}_0 . This externally applied magnetic field aligns the spin either parallel or anti-parallel to its direction, resulting in a splitting of the energy states given by

$$E(m_s) = g_e * \beta_e * m_s * B_0 \quad \text{Eq. 12}$$

Here, $E(m_s)$ is the energy of the spin state, m_s is the electron spin angular momentum quantum number, β_e is the Bohr magneton. B_0 is the magnetic field induction in units of Gauss (G) or Tesla (T) and g_e is the Landé-factor of the free electron in vacuum. Absorption of EM-radiation, resulting in a transition between spin states, occurs when the resonance condition is met, i.e. the incidental energy matches the energy gap between spin states:

$$\Delta E = h\nu = g_e * \beta_e * B_0 \quad \text{Eq. 13}$$

In this work, nitroxide radicals were utilized. Analogous to chemical shift in NMR, the chemical environment of the unpaired electron influences the effective magnetic

field it experiences and thus shifts the g-factor and the energy gap, resulting in an altered absorption spectrum. The most abundant Oxygen nucleus is ^{16}O with a total spin quantum number of zero, hence without influence on the electron. On the other hand, the most common Nitrogen nucleus is ^{14}N with a spin quantum number of one and a natural abundance of 99.63%. Since this nucleus is magnetically active, it is also subject to the *Zeeman* – Effect and spin-orbit coupling between the electron and the Nitrogen nucleus results in a splitting of the resonance into three lines. The total splitting of the energy levels, and therefore the absorption spectrum, is influenced by the electron *Zeeman* (**EZ**), nuclear *Zeeman* (**NZ**) and hyperfine coupling (**HF**) effects.

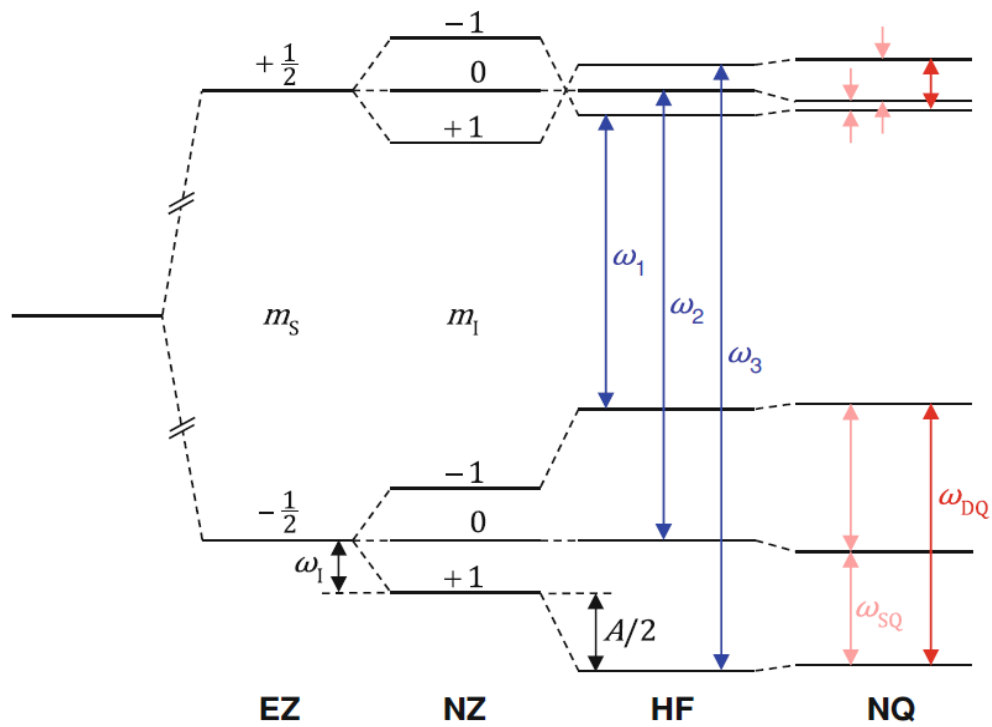


Figure 5 Splitting of electronic energy levels due to the *Zeeman* effect. For further explanation see text.

Adapted from: **JUNK, M. J. N. 2012**

The parameters \mathbf{m}_s and \mathbf{m}_I are the secondary electron and nuclear spin quantum numbers, respectively. \mathbf{A} is the hyperfine coupling tensor and will be described below in more detail. The nuclear single quantum (SQ) and double quantum (DQ) transitions from the nuclear quadrupole contribution (NQ) can be determined by advanced EPR methods, which are beyond the scope of this work. The allowed transitions (blue arrows; ω_i indicates the angular frequency of the transitions) according to the selection rules $\Delta\mathbf{m}_s = \pm 1$ and $\Delta\mathbf{m}_I = 0$ yield three absorption signals that occur, under irradiation at a constant microwave frequency, at different magnetic fields. The transition occurring at the highest magnetic field (ω_1) is most sensitive to environmental changes because it corresponds to the smallest energy gap. Frequency ranges of interest are classified into bands named after conventions of post-World War military radio technology. (see Table 2) Within each band, a range of frequencies is possible, the ones denoted in Table 2 show only the most common one. The ‘field’ values are given in units of Tesla (T) for $g = 2.0023$. Therefore, the exact values for the magnetic field at which transitions occur depend on the chosen band. By far the most commonly used frequency band is the X-band with microwave frequencies of about 9.5 GHz.

Table 2 Common microwave frequency bands and corresponding magnetic fields used in EPR

Band	Frequency [GHz]	Magnetic field [T]
X	9.5	0.34
Q	34	1.21
W	95	3.4

In general, the shape and position of the absorption lines are sensitive to both rotational dynamics of the probe and the polarity of the environment.

Depending on the molecular geometry, the Landé-factor g deviates from its value for the free electron in vacuum; it is then expressed as a tensor \mathbf{g} of potentially isotropic ($g_{xx} = g_{yy} = g_{zz}$), axial ($g_{xx} = g_{yy} \neq g_{zz}$) or rhombic symmetry ($g_{xx} \neq g_{yy} \neq g_{zz}$), referred to as g -anisotropy. For fast rotating nitroxide radicals in solution this anisotropy is averaged out for X-band frequencies and only the isotropic g -value can be obtained:

$$\mathbf{g}_{iso} = \frac{1}{3} \text{Tr}(\mathbf{g}) = \frac{1}{3} (\mathbf{g}_{xx} + \mathbf{g}_{yy} + \mathbf{g}_{zz}) \quad \text{Eq. 14}$$

Hyperfine interactions are described by the hyperfine coupling tensor \mathbf{A} . It contains both the anisotropic part of the dipolar interactions between the electronic and nuclear magnetic moments and the Fermi contact (isotropic) interaction for an electron in an s -orbital inside the nuclear volume, which is a direct measure of the electronic and nuclear magnetic dipole moments resulting from a finite possibility of the unpaired electron being located at the nucleus. Since this latter part arises exclusively for s -orbitals (or orbitals with partial s -character) the magnitude of the observed isotropic hyperfine coupling can be related to the spin density at the relevant nucleus. It turns out that the \mathbf{A} tensor for nitroxide radicals is axial in good approximation ($A_{xx} = A_{yy} \neq A_{zz}$), describing the anisotropic interactions.

As was the case for the \mathbf{g} tensor, fast rotating spin probes in solution give an averaged value described by:

$$\mathbf{a}_{iso} = \frac{1}{3} \text{Tr}(\mathbf{A}) = \frac{1}{3} (A_{xx} + A_{yy} + A_{zz}) \quad \text{Eq. 15}$$

Both A_{zz} and \mathbf{a}_{iso} are then proportional to the spin density at the ^{14}N nucleus, and the experimentally accessible value of \mathbf{a}_{iso} allows for the evaluation of the polarity of the probes environment, since the spin density shifts along the N-O axis and thus the coupling changes (see Figure 6) The values are generally larger in polar environments, because localization of the electron at the Nitrogen nucleus results in energetically favourable charge separation. Qualitative assessment of polarity and rotational dynamics is therefore possible directly from the experimental spectrum without simulation.

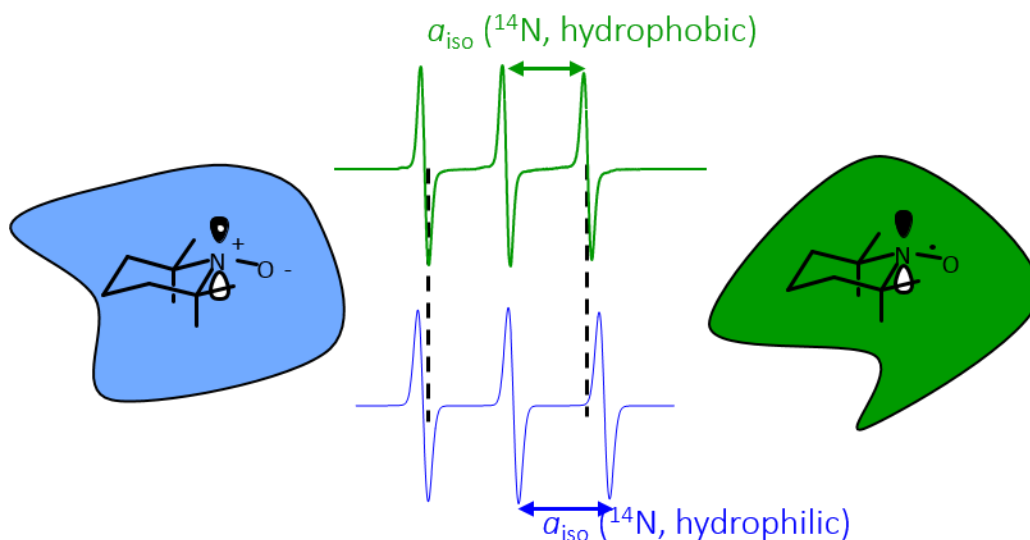


Figure 6 Dependence of the isotropic hyperfine coupling constant on polarity. Adapted from: **JUNK, M. J. N. 2012**

The lineshape of EPR spectra is influenced by a number of dynamic processes that change the resonance frequencies without involving spin flips. Firstly, *molecular tumbling* broadens the spectral lines. The high-field line is, as mentioned above, most sensitive to this effect, because it corresponds to the transition across the smallest energy gap. Therefore, slight perturbations of the energy levels lead to more pronounced changes in the spectrum.

A second major reason for alterations in linewidth is known as *exchange broadening and narrowing*. This phenomenon is caused by enhanced relaxation rates due to frequent collisions between unpaired electrons. Upon colliding the *singly occupied molecular orbitals (SOMOs)* containing the unpaired electrons momentarily overlap and the electrons become indistinguishable. According to the Pauli principle, two electrons with the same spin orientation cannot be simultaneously found in the same orbital; therefore post-collision separation of the orbitals leads to a random re-distribution of the two different spin states, which is the equivalent of relaxation. When the frequency of exchange events approaches the frequency difference of the spectral lines participating the hyperfine structure is lost and the spectrum coalesces into a single broad line. A further increase in the exchange frequency ultimately leads to narrowing of this single line because the exchange happens so fast that the time average of the hyperfine splitting approaches zero. Both spin exchange and

restricted rotational diffusion lead to markedly broadened lines in spectra of aggregated radical species, such as micelles.

2.6 SPIN-LABELLING OF HFB2

While maleimide functionalized spinlabels readily react with sulfhydryl groups and are therefore frequently used site-directed spin labelling (**SDSL**) towards cysteines, they may also react with primary amines at pH values above 8.5 and since all cysteine residues present in the protein are engaged in stable intramolecular disulfide bonds and no reducing agent was used, only amino acids with a primary amine function are valid target sites. These residues include four lysines at positions 27, 46, 49 and 66; two asparagines at positions 10 and 17; and three glutamines at positions 40, 60 and 65. According to RCSB Protein Data Bank and published amino acid sequence of HFB2 [RIVEROS, D. G., SHOKRIBOUSJEIN, Z. *ET AL.* 2015] positions 40 and 46 lie in the large region between beta-strands while all others are part of a beta-strand, mostly located at either end of the secondary structural feature and surrounded by apolar amino acids. Hence, most of the valid target sites are part of the 'hydrophobic patch'.

Experimental parameters. Powdery HFB2 was dissolved in chilled TFA and the solvent was removed in a dry air stream. 1 mg of protein was then dissolved in 1.5 ml of pure water and a ten-fold excess of 3-maleimido-PROXYL (**MSL**) in ethanol was added. After incubation at room temperature and gentle shaking for 14 hours the solution was subjected to size-exclusion chromatography on a self-packed Sephadex™ - G15 glass column to remove residual unattached spinlabel. Figure 7 shows X-band cwEPR spectra of the labelled protein and the pure spinlabel as reference under identical conditions. The intensity of the pure label's high-field signal is closer to that of the other lines, indicating a more isotropic movement, yet the isotropic hyperfine coupling a_{iso} , reflected in the spacing between signals, is smaller than that of the labelled protein. As discussed in **section 2.5** the isotropic hyperfine coupling is sensitive to the environment's polarity.

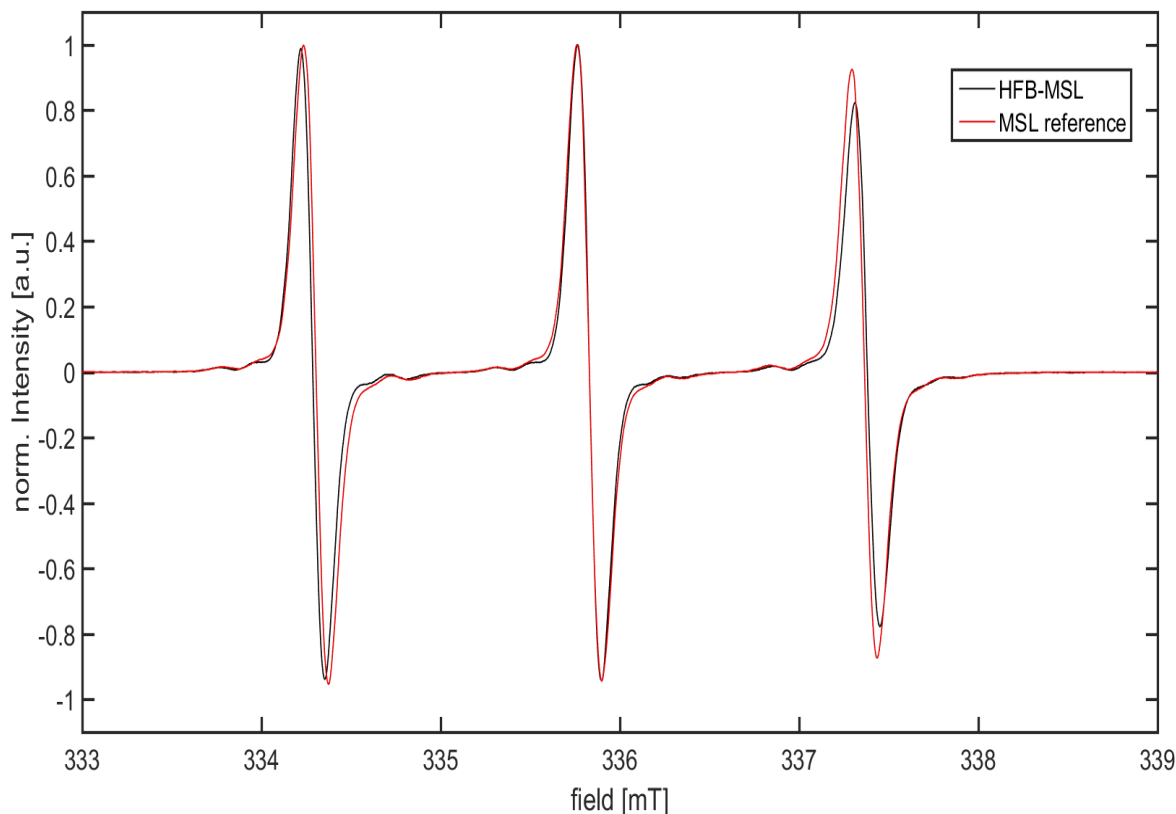


Figure 7 X-band cwEPR spectra of spin-labelled HFB2 (*black*) and free MSL (*red*) under identical conditions.

For further proof of the labelling success Q-Band spectra were recorded at room temperature. Pure MSL was used in the same initial concentration of $280\ \mu\text{M}$ as a reference. While a detailed interpretation of the spectra shown in Figure 8 is rather complicated, the qualitative differences serve as confirmation of the labelling process. After two purification steps via size-exclusion chromatography (**SEC**) all remaining free label should be removed based on experience with ‘standard systems, such as bovine serum albumin (**BSA**) and several spin-labels. One major problem yet to be resolved is the unambiguous confirmation by mass spectrometry. While several attempts have been made applying both matrix-assisted laser desorption/ionization (**MALDI**) and electrospray ionization (**ESI**) mass spectrometry, fragmentation and characterization proved to be difficult for reasons not fully examined yet.

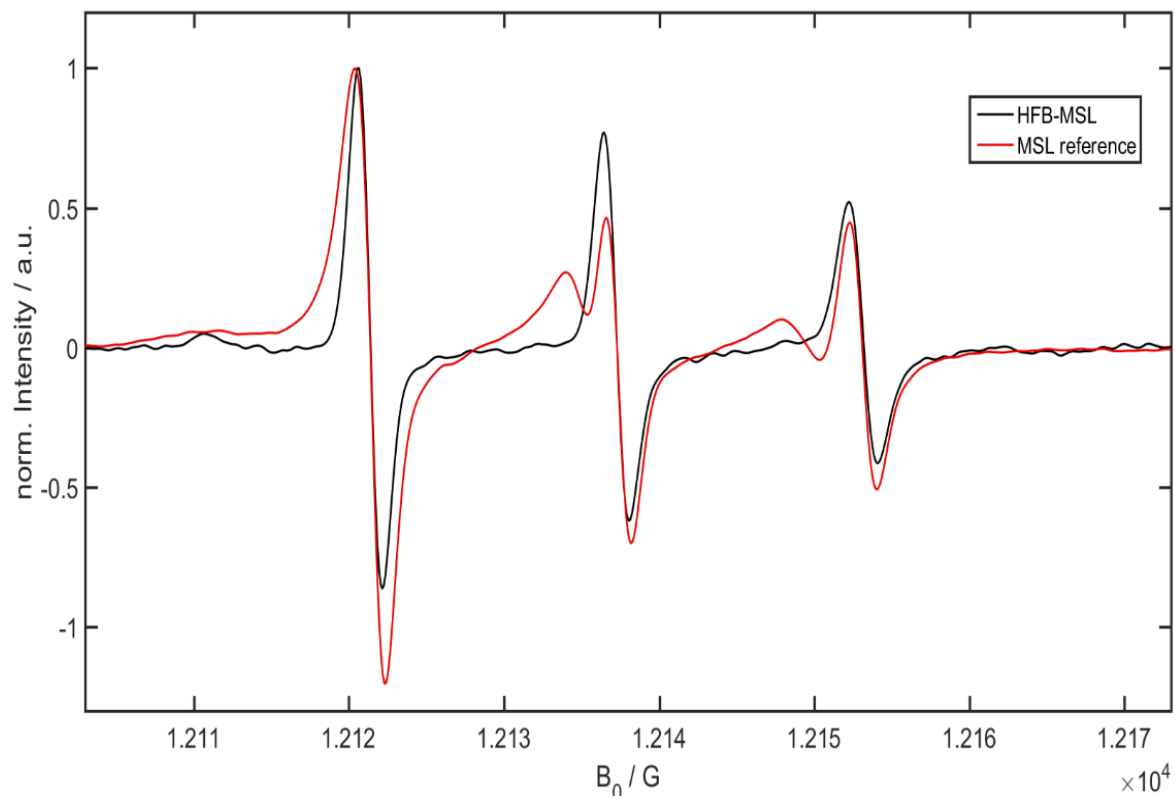


Figure 8 Q-Band spectra of spin-labelled HFB (*black*) and the free MSL (*red*) in water at room temperature.

2.7 VESICLE PREPARATION

Vesicles of 1-Palmitoyl-2-Oleoyl-*sn*-glycero-3-Phosphocholine (**POPC**) containing varying amounts of 16-DOXYL stearic acid (**16-DSA**) were prepared by extrusion to a diameter of 100 nm. After mixing chloroform solutions of both components to the desired ratio the solvent was evaporated in a stream of nitrogen and purified water of 35 °C was added to a total lipid concentration of 1.2 mM.

Concentrations of stock solutions and mixing tables can be found in APPENDIX A. Respective volumes of the aqueous vesicle solutions were then added to 40 µg portions of lyophilized protein to get the desired protein concentrations. Extrusion was performed through a polycarbonate membrane at the same temperature with a total of 31 passes of the solution through the membrane. The preparation of vesicles containing 1-Palmitoyl-2-Stearoyl-(16-doxyl)-*sn*-glycero-3-Phosphocholine (**PDSPC**) followed the same procedure.

To verify the success DLS was performed at 20 °C, resulting in a relatively sharp size distribution around a hydrodynamic diameter of approximately 120 nm (see chapter 4)

3. THE AIR/WATER INTERFACE AND TRANSFER TO SOLID SUBSTRATES – THE INFLUENCE OF AREAL AND INTER-FACIAL CONSTRAINTS ON MICROSCOPIC MORPHOLOGY

The study of structure formation at the air/water interface was approached from different angles. On the one hand epifluorescence microscopy allows for the visualization of protein layers as they form at the interface, while the film balance measurement itself reveals mechanical properties of the monolayer and potential phase transitions or reorganization processes.

On the other hand LS-transferred films studied by AFM allow for a higher resolution while introducing new constraints to the system, namely changing the nature of the interface from air/water to mica/air; and in the case of multilayer structures more complex mechanisms take hold.

The main focus of this chapter is the influence of areal constraint and multiple lateral compressions and expansions on the morphology of protein films of both classes.

It should be noted that sample preparation and handling evidently have a major influence on the observed morphology. YU and co-workers report significant differences between Langmuir-Blodgett (LB) and Langmuir-Schaefer (LS) films for a class I hydrophobin. [YU, L., ZHANG, B. *ET AL.* 2008] SUNDE and colleagues presented AFM images from LB and LS films as well as films deposited from a droplet on different substrates, resulting in visibly different morphologies. [SUNDE, M., KWAN, A. H. *ET AL.* 2008]

All results presented herein are therefore to be considered in the context of the specific preparation methods applied.

3.1 SINGLE COMPRESSION TO VARIOUS SURFACE PRESSURES

While the compression behaviour of and phase transitions in lipid monolayers is generally reversible, the same cannot be assumed for aggregating proteins.

Figure 9 shows isotherms for a single compression and subsequent expansion of both proteins. While neither shows clear indication of phase transitions or ripping, there is a strong hysteresis between compression and expansion. The mean molecular areas for both proteins and magnitude of the hysteresis measured at 6 mN/m displayed in Table 3 suggests the formation of stable multilayer aggregates in both cases that do not easily dissolve upon expansion.

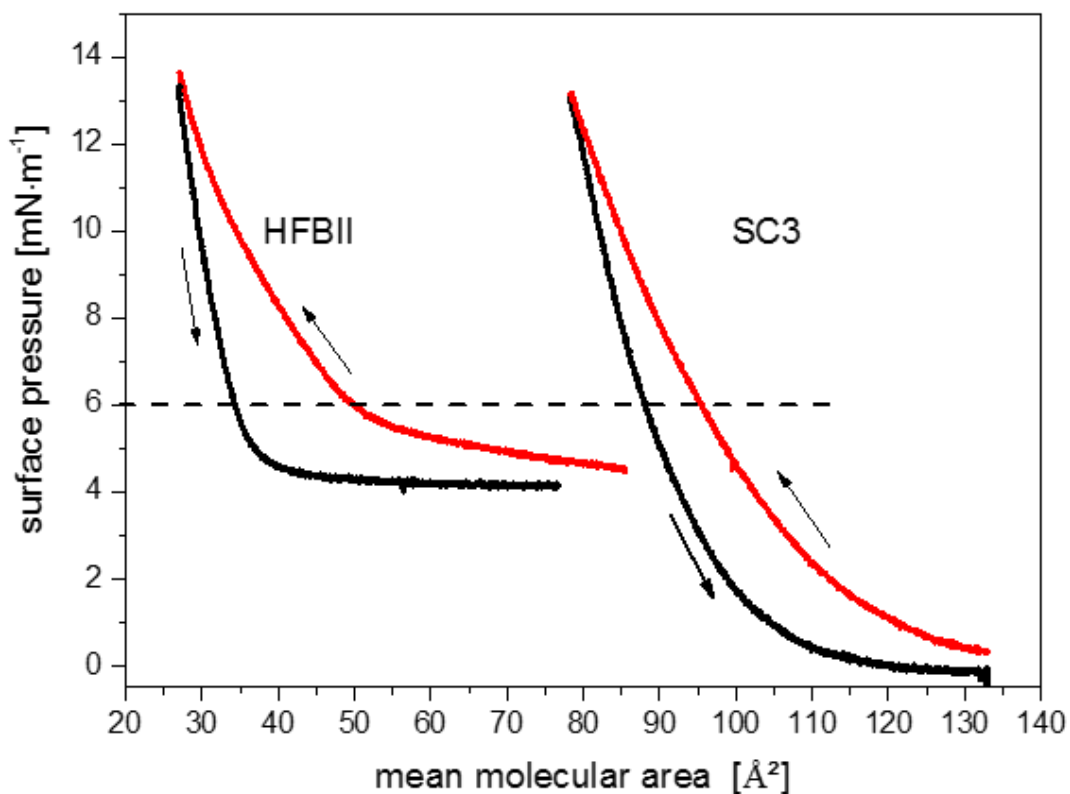


Figure 9 Compression isotherms of SC3 and HFB2 on pure water at 20 °C. Compression speed was 2 Å²/ (molecule*min)

This also hints at a non-uniform dissolution of the film in general. Moreover, additional compressions showed no difference compared to the second one. It can be concluded that no molecules are expelled into the subphase, which is in agreement with the findings of PAANANEN and co-workers.

[PAANANEN, A., VUORIMAA, E. *ET AL.* 2003] This will be discussed further in section 3.2

Table 3 Mean molecular areas [Å²] and hysteresis at 6 mN/m between compression and expansion after the second cycle for both hydrophobins.

Sample	Compression	Expansion	Difference
SC3	95.45	88.00	7.45
HFB2	49.91	34.28	15.64

3.1.1 SC3

AFM micrographs of SC3 transferred at a very low surface pressure of 1.5 mN/m show a rather homogeneous morphology. Globular aggregates between 100 and 500 nm in size and fibrils of varying length are present on top of a closed protein layer. As Figure 10 illustrates, fibrillary aggregates dominate at higher transfer pressures and the film generally becomes more homogeneous. Coverage of the mica surface varied greatly, but generally increased with increasing surface pressure from around 62 % at low constraints to a somewhat stable covering of about 90 % at all higher transfer surface pressures (see Table 4).

Table 4 Coverage of the mica surface by SC3 at different transfer pressures after a single compression; #x indicates independent sample number

Pressure	#1	#2	#3	#4	Average	SD
mN/m	%	%	%	%	%	%
1,5	55,16	58,57	68,06	68,99	62,70	6,88482
6,5	85,96	94,84	94,31	92,00	91,78	4,06961
13	77,37	72,25	93,4	67,69	77,68	11,20267
19	99,91	95,70	94,13	99,36	97,28	2,80845
27,5	97,7	99,38	81,51	99,09	94,42	8,63784

In some cases large clusters of protein matter with a height of about 25 nm were visible on an otherwise clean mica surface. This is believed to be an artefact of sample preparation, as these morphologies could not be reproduced, and once again highlight the heterogeneity of self-assembled structures at weak constraints.

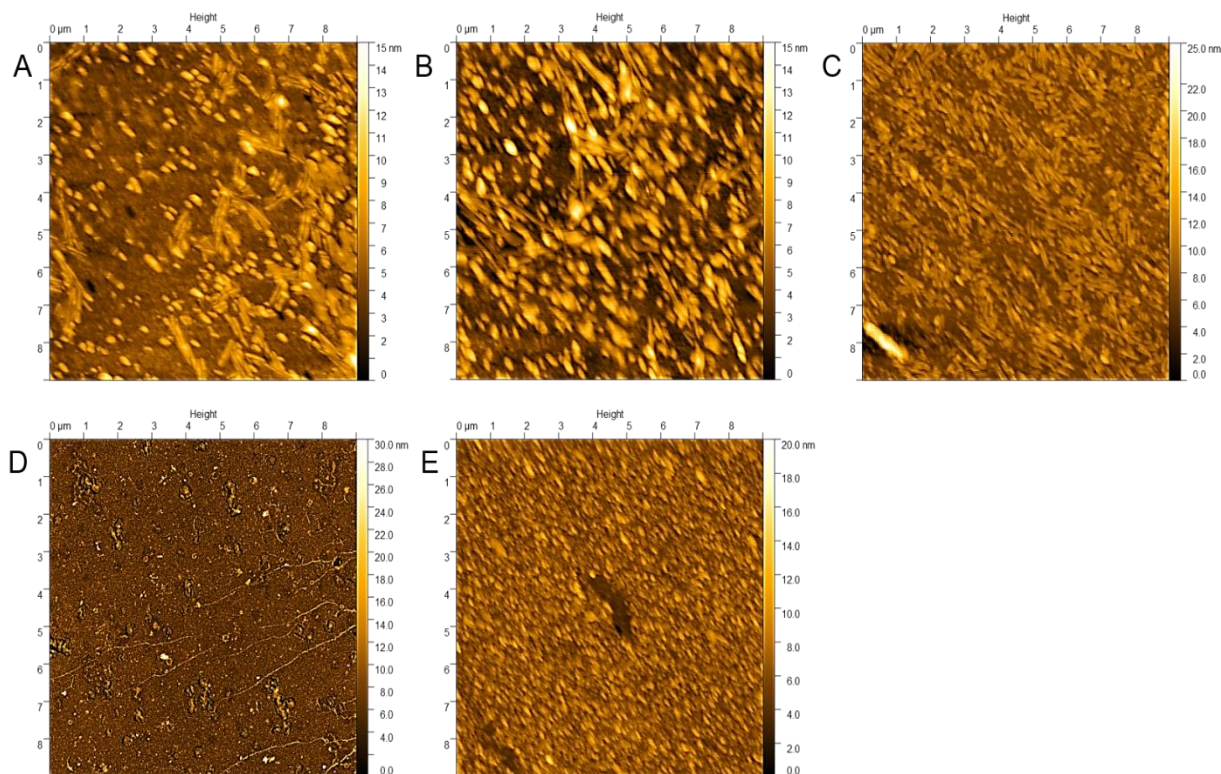


Figure 10 AFM height micrographs of SC3 at different transfer surface pressures: **A)** 1.5, **B)** 6.5, **C)** 13, **D)** 19, and **E)** 27.5 $\text{mN}\cdot\text{m}^{-1}$; dimensions are $9\times 9\ \mu\text{m}^2$.

While the absolute numbers of both distribution density and height shall not be interpreted in this work, due to their dependence on various factors and poor reproducibility, it is evident that the height distribution shifts from bimodal at low and intermediate pressures to a homogeneous distribution centred around 5-6 nm at a transfer pressure of 27.5 mN/m. (see Figure 11). At all stages, a closed yet inhomogeneous protein layer is present underneath these aggregates.

As shown in Figure 12 both length and width vary greatly over the entire range of transfer pressures. Owing in part to the inherent inaccuracy of the “by hand” method, the variance in length for the first three points is nonetheless much greater than for the final pressure of 19 mN/m; it is therefore concluded to be mostly a feature of the aggregates themselves, as comparable random errors in measuring the dimensions are to be expected.

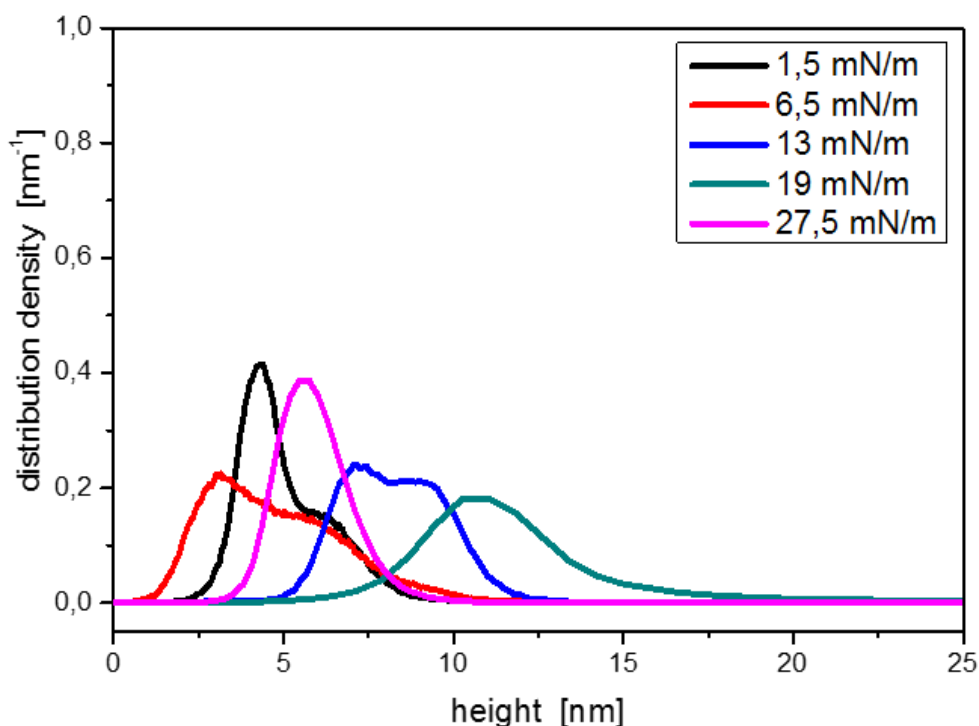


Figure 11 Height distribution of SC3 structures transferred at different surface pressures.

As mentioned above, the apparent sizes of fibrillary aggregates do not follow a clear trend. Moreover, not all AFM micrographs showed fibrils in the first place and their resolution complicates an exact analysis. Sections of micrographs no larger than $5 \times 5 \mu\text{m}$ that contained fibrils were analysed to get an idea of the general size of the aggregates. The results are summarized in Table 5.

Table 5 Average number, length and width of SC3 fibrils depending on transfer pressure

Pressure	Fibril count	Average length	Average width
mN/m		nm	nm
1,5	60	507.5	76
6,5	49	327.4	39.8
13	59	572.9	83.6
19	40	105.8	11.0

At 6.5 mN/m the greatest variance was observed while the micrographs themselves showed the strongest heterogeneity of aggregates.

Taking into account the likely mechanism of aggregation proposed by Kwan and colleagues [KWAN *ET AL.*, 2006] (see also section 3.2.1.1) one can propose the following explanation:

At low compression states aggregation is predominantly self-organized. Molecular motion in the interface allows for the favourable arrangement of molecules to enable loop-regions to extend the existing β -barrels. The external constraint restricts freedom of movement across the interface, resulting in shorter fibrils. On the other hand, the height distribution shifts to a larger average at 19 mN/m, indicating multi-layered structures; therefore, fewer fibrils in total can be observed. This explanation will be further explored in the following section on multiple compression-expansion cycles.

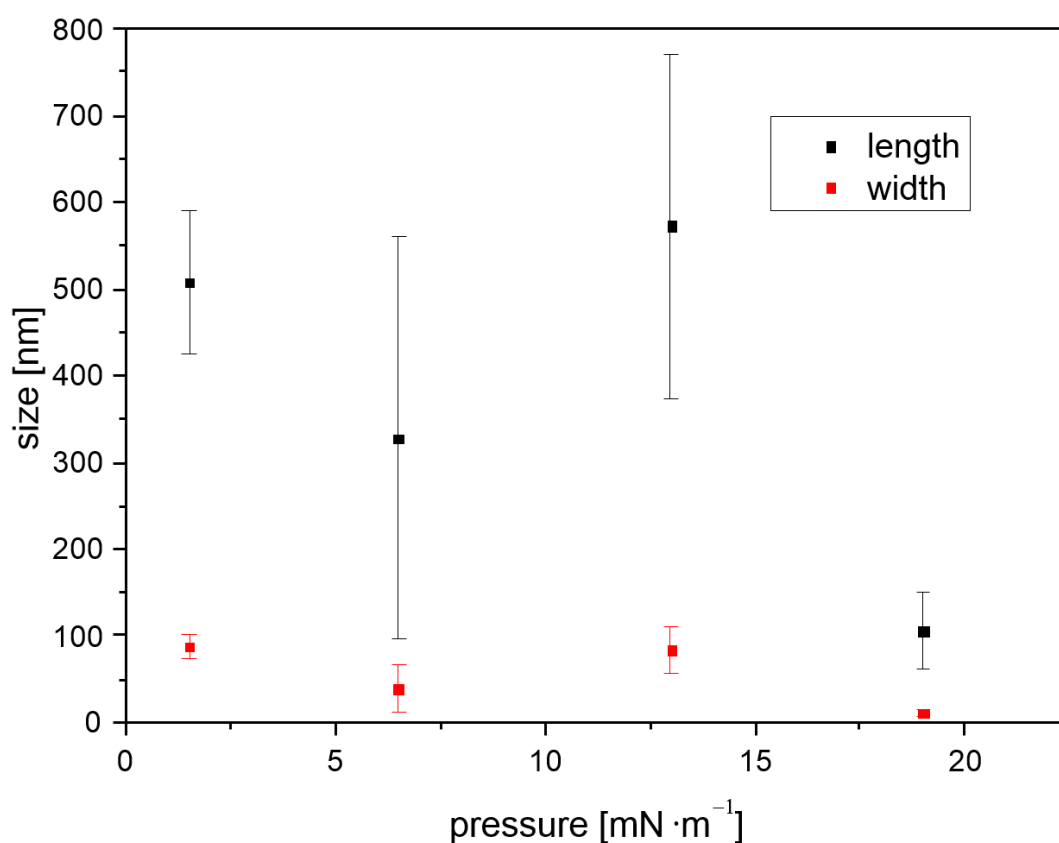


Figure 12 Length and width of fibrils depending on transfer pressure.

3.1.2 HFB2

Class II hydrophobin HFB2 shows a homogeneous protein film at low transfer pressures, with a height of roughly 2 nm. This value is in good agreement with the findings of KISKO *et al.*, who report a thickness between 24 and 28 Å at the air/water interface. [KISKO, K., SZILVAY, G. R. *ET AL.* 2009] It must be stated here, however, that their data was obtained at higher surface pressures of 10 to 20 mN/m. As discussed before, preparation and handling of the sample are of major importance for the results. Absolute values are therefore once again pretermitted and only trends are discussed. Irregular structures varying in height between 4 and 15 nm are present on top of said closed layer at all stages of compression. Figure 13 and Figure 14 show the AFM micrographs and height distribution for samples transferred at different pressures, respectively.

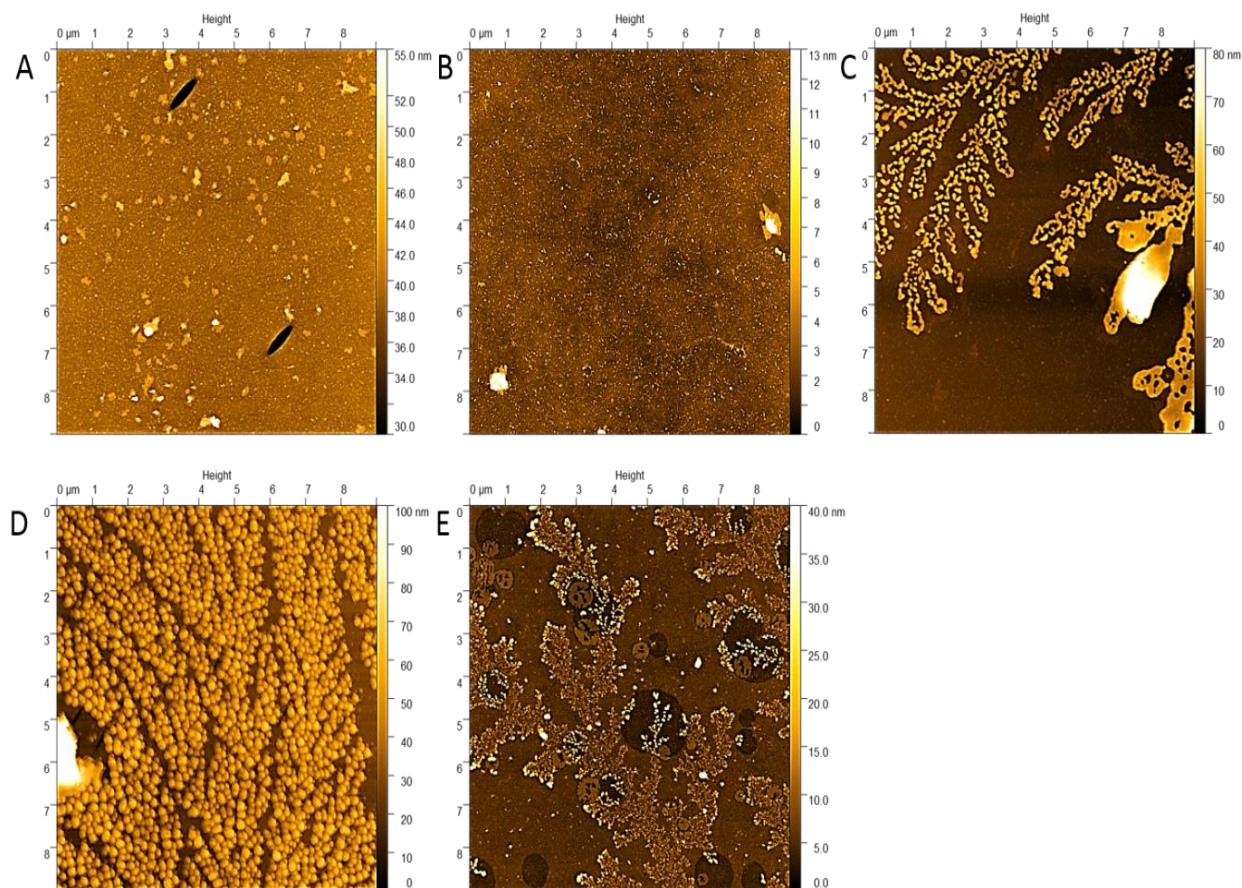


Figure 13 AFM height micrographs of HFBII at different surface pressures: A) 3.3, B) 6.5, C) 13, D) 19, and E) 27.5 mN/m; dimensions are 9x9 μm^2 .

The most notable feature of HFB2 structures arises at an intermediate transfer pressure of 13 mN/m. Large dendritic aggregates with heights between 40 and 100 nm and several microns in length appear and persist with increasing pressure. Going hand in hand with an increase of the substrates coverage, these complex multi-layered structures constitute the main form of aggregation in all samples at intermediate to high transfer surface pressures. Their height, however, decreased with a further increase in surface pressure before transfer. Starting at 2 nm thickness at low surface pressure, the height distribution broadens and shifts to values of up to 42 nm at 19 mN/m transfer pressure; at 25 mN/m it again drops and stabilizes around 5 nm. This steep decrease may be an artefact of sample preparation. As the densely packed film is ripped from the air/water interface it is subjected to drying capillary forces, changing the dominant interactions from protein/water to Protein/air and intermolecular forces (see also the discussion part at the end of this chapter).

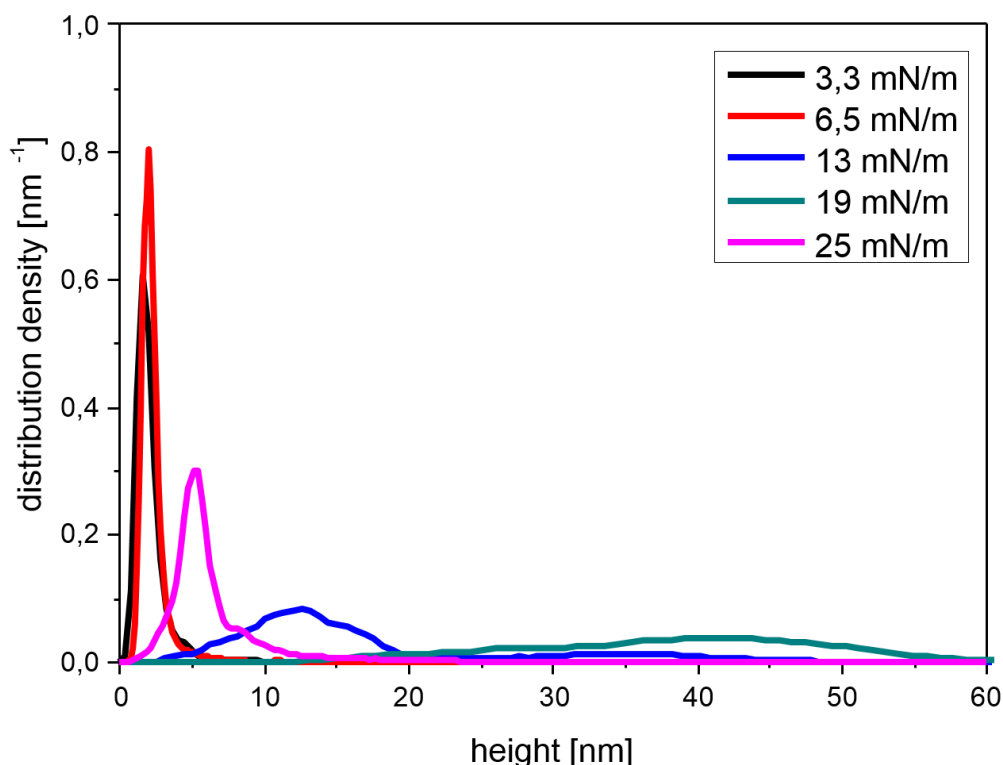


Figure 14 Height distribution of HFBII structures transferred at different surface pressures.

Coverage of the mica surface for both proteins is shown in Figure 15.

For SC3 covering rises from about 64 % at a very low surface pressure of 1.5 mN/m to about 90 % already at 6.5 mN/m, where it remains stable over all transfer pressures achieved. For the HFB2 samples, on the other hand, it is generally higher at low surface pressures, ranging from about 60 to 80 % at low pressures, and stabilizing at around 92 % at transfer pressures of 13 mN/m and above.

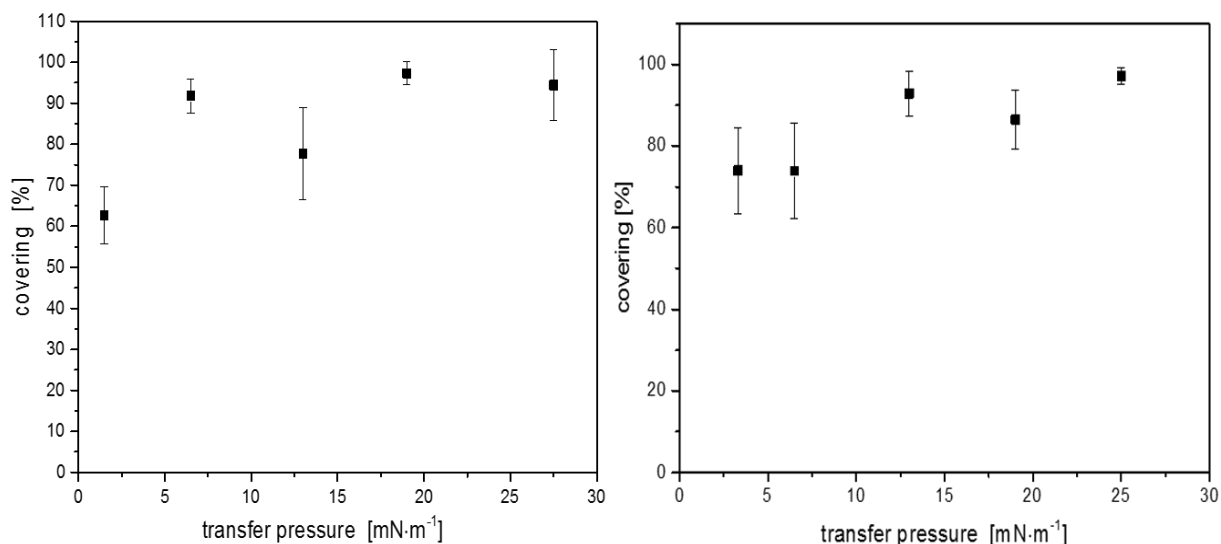


Figure 15 Coverage of the mica surface by protein films transferred at different surface pressures. *Left: SC3; right HFB2*

3.2 MULTIPLE COMPRESSIONS/EXPANSIONS TO VARIOUS SURFACE PRESSURES

When scrutinizing the literature concerning interfacial morphologies of a multitude of hydrophobins, it quickly becomes apparent that surface pressure and sampling are often well-adjusted. Additionally, the resolution achieved in former AFM studies is much higher than what is presented here. Given the results of single compressions, the question arises how the non-uniform disassembly observed both in epifluorescence and AFM is influenced by multiple cycles of constraint and relieve and in turn influences the morphology ultimately arising. Figure 16 shows compression and expansion isotherms of a single sample of HFB2.

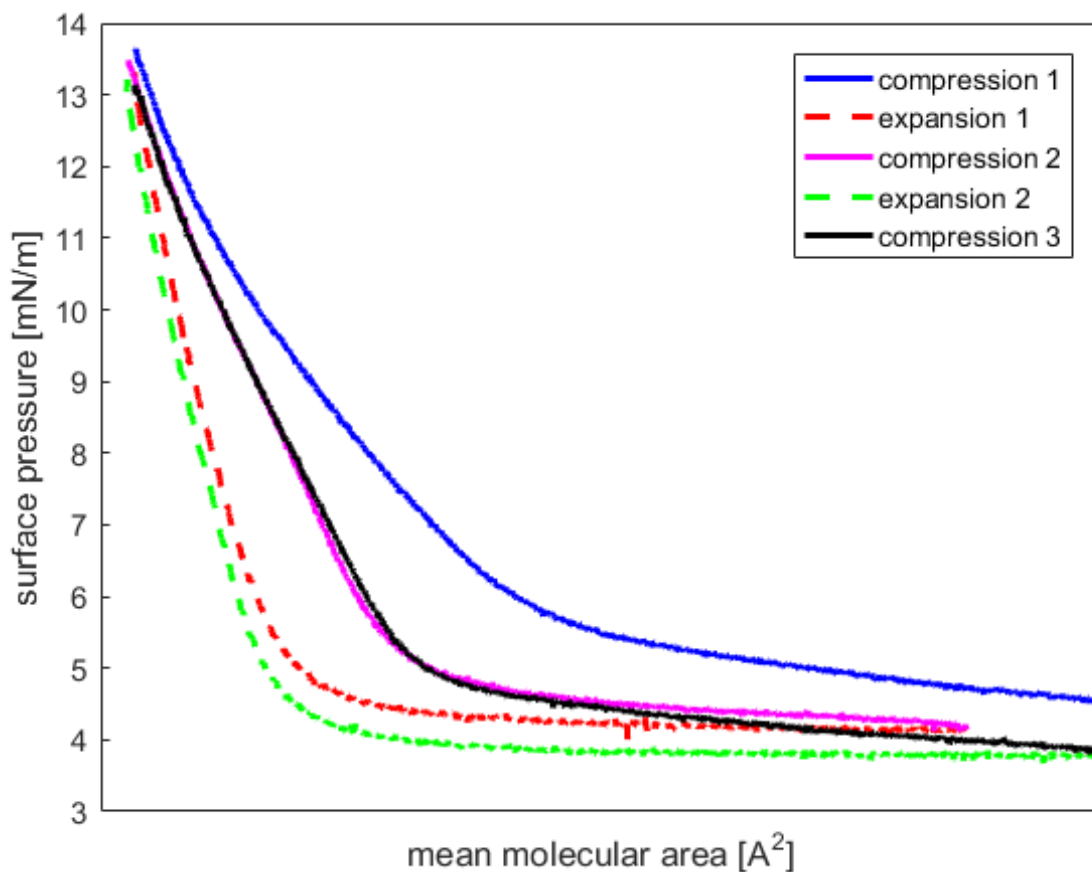


Figure 16 Hysteresis between the compression and expansion isotherms of HFB2. Additional cycles did not differ from the second one.

The x-axis does not carry any designated values, because they could not be calculated from exact protein concentrations. The trend, however, is visible in all experiments of this type. As already mentioned in the previous section, there is a strong hysteresis between the first compression (*blue*) and expansion (*red dots*) isotherms. The second and all subsequent compression isotherms lay on top of each other, indicating that the formation of stable aggregates, which gives rise to the hysteresis in the first place, does not continue over more subsequent cycles. Similar curves were recorded for SC3 and are presented in section 3.2.1.1.

Taking into consideration the effects of lateral pressure on the morphology, multiple compressions and expansions were carried out to the same values of transfer pressure used in the experiments previously shown. Transfer pressures of 13 mN/m for both proteins and 1.5 mN/m for class I SC3 are of special interest to investigate both weak initial and multiple submissions to ‘intermediate’ constraints.

3.2.1 SC3

Compressing SC3 to 1.5 mN/m several times before transfer again leads to a homogenization of the observed aggregates. As mentioned in the previous section, large spherical aggregates of several hundreds of nanometres in diameter are present alongside fibrils of various lengths. These fibrils persisted after expansion to zero surface pressure. Once again, the height distribution shifts from bimodal to monomodal curves and the observed structures only partially dissolve upon expansion and cluster into larger assemblies. Because of this clustering there is great variation between samples and the coverage of the substrate decreases by about 40%. This non-uniform disintegration of the surface film becomes even clearer when SC3 is compressed to 13 mN/m and subsequently expanded to low surface pressures several times. The fibrils shorten drastically from about 570 nm on average after the first compression to just over 100 nm length after the fourth, indicating a preference to form new fibres upon recompression over extending existing ones. As was the case for a single compression to ever-increasing surface pressures, the films morphology grows more homogeneous. Once again the height distribution shifts from bimodal to monomodal. (see Figure 17)

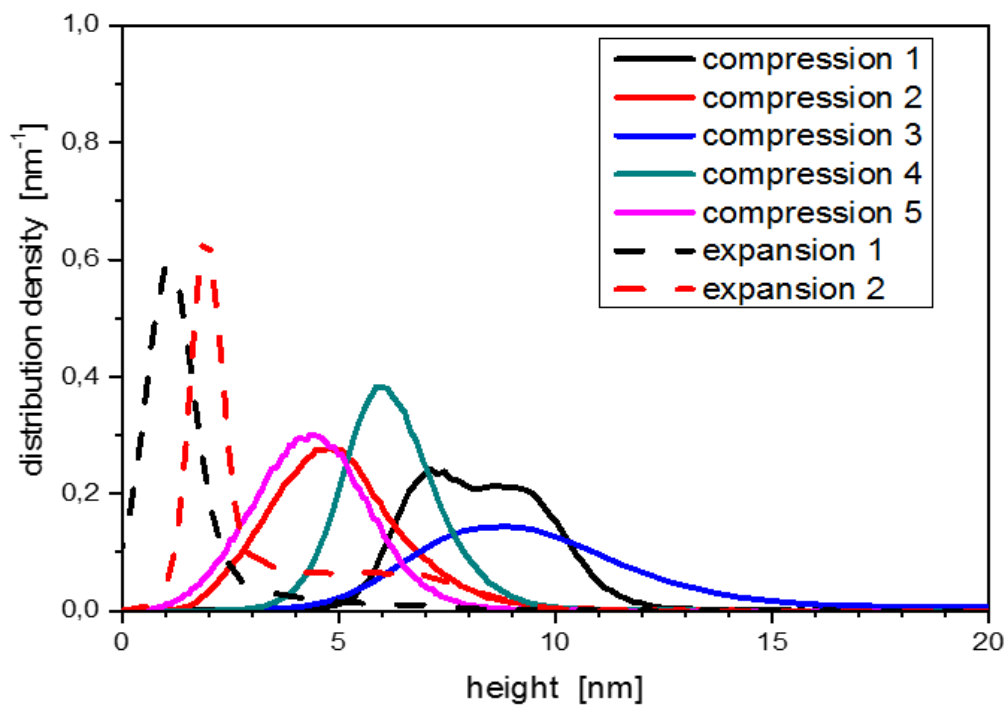


Figure 17 Height distribution of SC3 aggregates over several compression/expansion cycles to 13 mN/m.

Here, the curves for the first and second expansion exhibit a shoulder in the range of 2.5 to around 8 nm, which coincides with the maxima of preceding compressions. The AFM micrographs of expanded films show a strong increase in the height of these aggregates, mainly due to the formation of globular structures that vary greatly in their size and thickness, which explains the strong broadening of the height distribution curve for the third expansion. (see Figure 18)

Figure 18E shows a remarkable feature which, to the best of the author's knowledge, has never before been presented for hydrophobins. A more detailed examination of the structures present in that sample can be found in section 3.2.3.

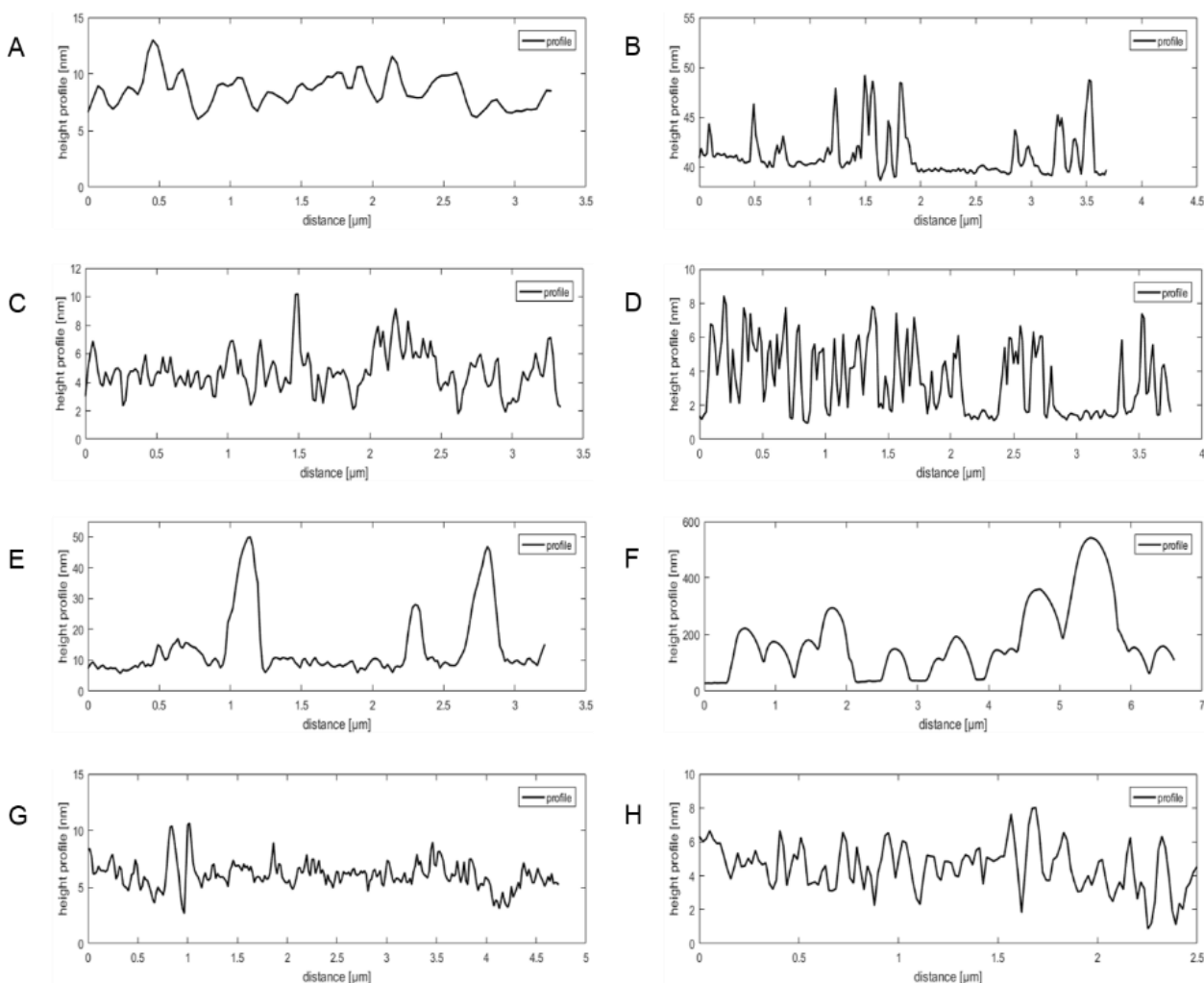
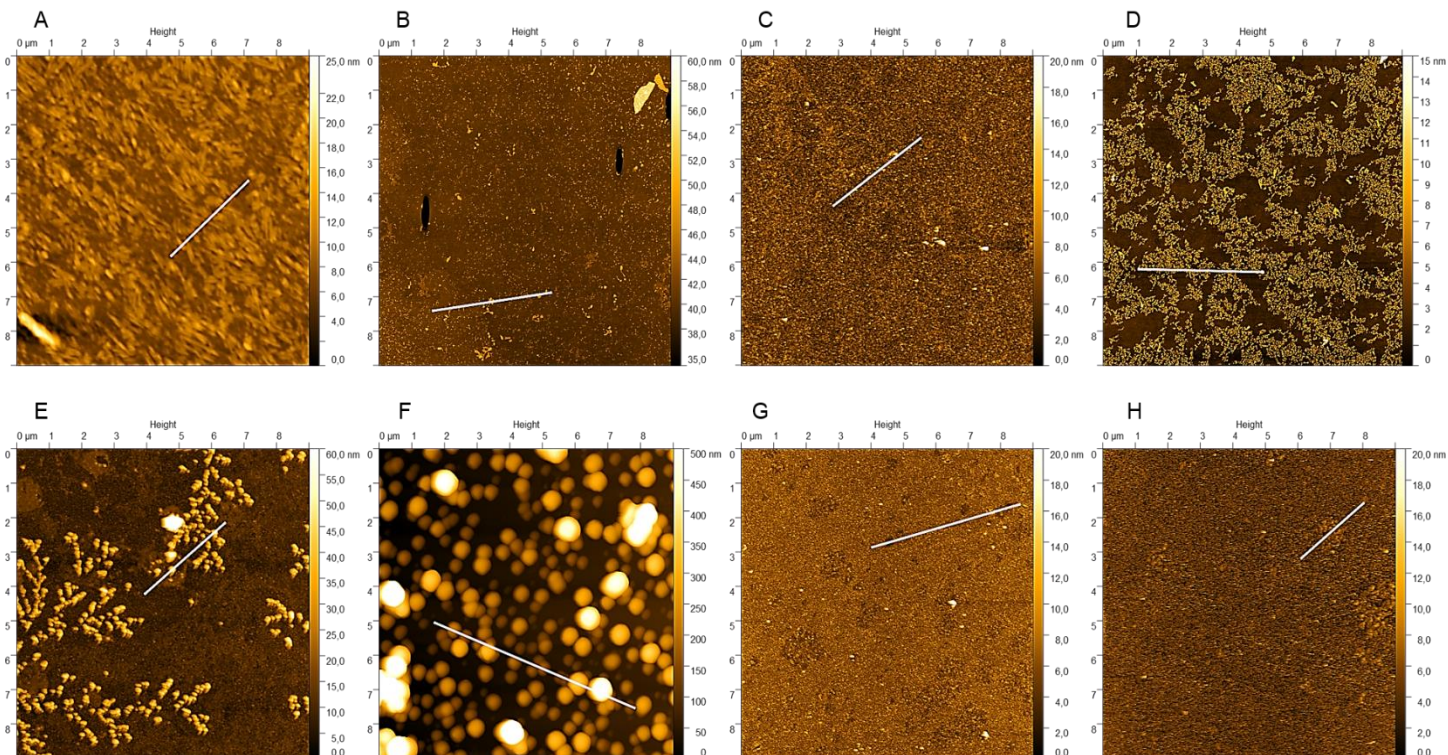


Figure 18 top: AFM height images after **A)** 1 compression, **B)** 1 expansion, **C)** 2 compressions, **D)** 2 expansions, **E)** 3 compressions **F)** 3 expansions, **G)** 4 compressions, **H)** 5 compressions. Dimensions are $9 \times 9 \mu\text{m}^2$; *bottom:* cross-sections along the indicated lines.

3.2.1.1 Epi-fluorescence microscopy

Aggregation of SC3 at the air/water interface can be monitored by epi-fluorescence. As discussed in chapter 2.1.3 both the choice of dye and its 'position' within the system are of major concern for such an experiment. Two dyes of different hydrophathy were chosen to monitor the formation of aggregates and gauge the dyes' influence on the proteins behaviour.

Firstly, 4,4'-Dianilino-1,1'-Binaphthyl-5,5'-Disulfonic acid, dipotassium salt (**bis-ANS**) was chosen to monitor fibrillation. It has been shown that bis-ANS is superior in the detection of fibrillation in peptides and proteins even to thioflavin T [YOUNAN, N. D. AND VILES, J. H. 2015] This is attributed to the dyes higher affinity towards exposed hydrophobic patches in fibres. Its spectral properties are comparable to those of thioflavin T, e.g. absence of fluorescence emission in water due to twisted intramolecular charge transfer (**TICT**) motion, while a hindrance of said twisting motion after binding to the surface of a fibre yields a high fluorescence intensity. Bis-ANS has successfully been employed in the determination of the critical aggregation concentration (*cac*) of bolalipid micelles where conventional fluorescence probes such as pyrene failed. [KORDTS, M., KERTH, A. *ET AL.* 2017] Following the mechanism of fibrillation proposed by Kwan and co-workers [KWAN, A. H., WINEFIELD, R. D. *ET AL.* 2006]

fibres of class I hydrophobins form by extension of the mostly hydrophobic β -barrel and should thus present large hydrophobic strands to allow for the adsorption of the dye. However, bis-ANS is very hydrophobic and therefore prone to adsorption to the air/water interface. Hence it constitutes a foreign molecule in the interface which might influence the self-assembly of the protein.

Figure 19 shows a compression isotherm of SC3 on a 0.5 μ M solution of bis-ANS. Evidently, the isotherm is different from what was presented in the previous section. A notable drop in surface pressure between around 60 and 30 \AA^2 / molecule indicates the beginning of fibrillation and the stacking of fibres. Several phenomena evident from the values of Π need addressing here. Firstly, the absolute values of surface pressure at which no further compression is possible (and/or the film collapses) are very low. Secondly, negative values of surface pressure are observed in virtually every sample. It should be noted again that the surface pressure is defined

as the difference in surface tensions between the pure subphase and the film-carrying system.

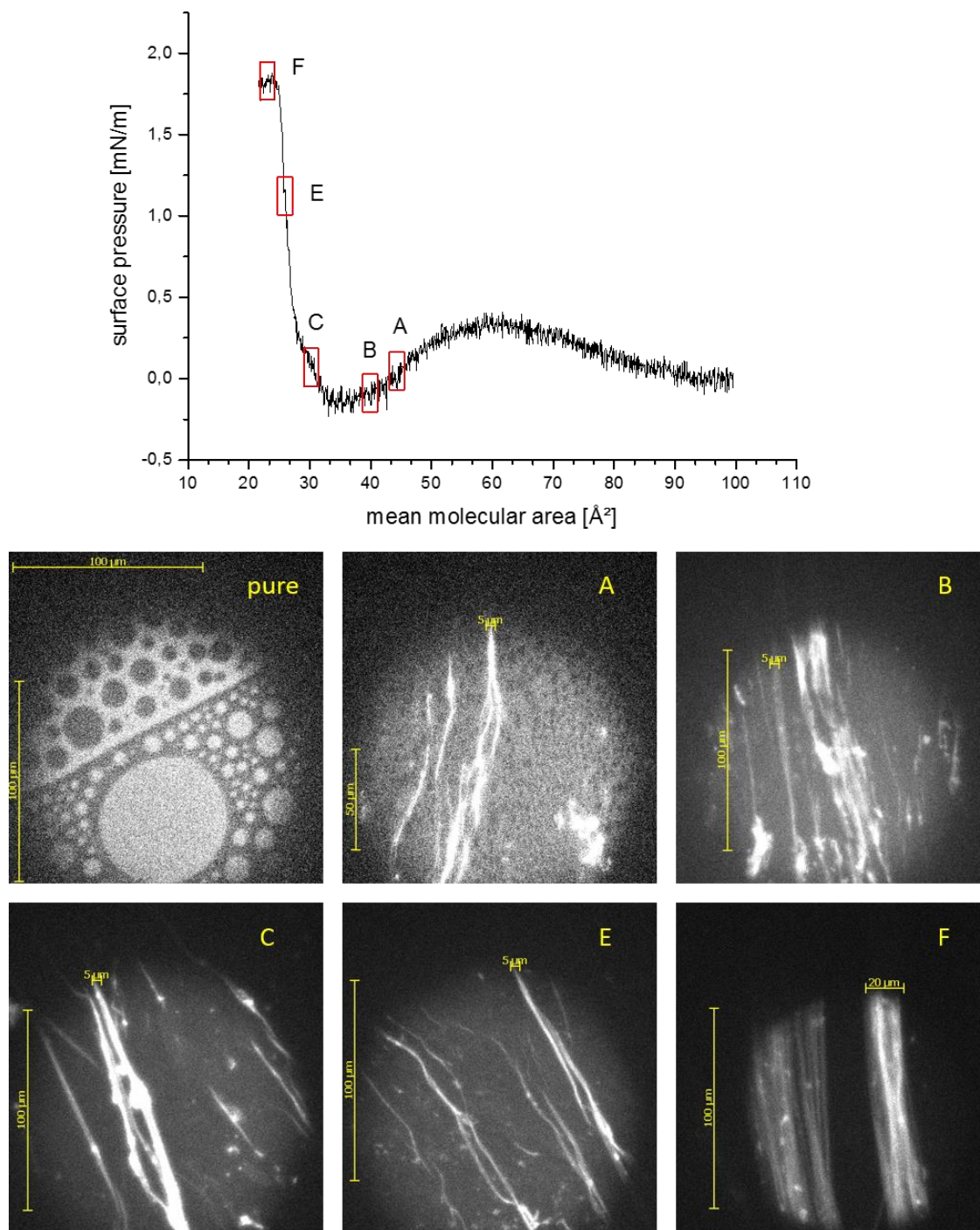


Figure 19 *top*: compression isotherm of SC3 on 0.5 μM Bis-ANS solution; *bottom*: fluorescence microscopy images at the indicated points in the isotherm. ‘pure’ refers to the interface before spreading of the protein. Image “D” was omitted from this figure.

Negative values are therefore indicative of an increase in surface tension. As can be seen in Figure 19 **bottom** fibrous aggregates of more than 100 μm in length are

present in bundles of several microns in width and appear stacked on top of each other. The darker regions between those bundles are likely also occupied by a protein film. Since the dye is not adsorbed there, however, no statement about the morphology or packing state can be made for those regions.

Generally speaking, surface tension arises from the anisotropy of interactions between molecules at the interface with stronger interactions directed into the sub-phase, as they are not compensated by those directed towards the gas phase. In recent years the influence of π - π -stacking and hydrophobic interactions on fibrillation kinetics, stability and morphology has been examined in great detail for various amyloidogenic peptides. Two schools of thought have arisen in this regard. On the one hand, aromatic moieties contribute to fibrillation due to π -stacking interactions by enhancing the fibrillation kinetics, increasing the thermodynamic stability of fibres, providing a directional component for fibre growth and elongation, or any combination of those effects. On the other hand it has been argued that the hydrophobic nature and planar geometry, and by extension the β -sheet propensity, of critical amino acid sequences are the major factors for fibrillation. In this case aromaticity is advantageous, but not absolutely required for amyloidogenesis. [PROFIT, A. A., VEDAD, J. *ET AL.* 2015] Notably, MARSHALL *et al.* have shown that a readily fibrillating peptide could be rendered unable to aggregate by substituting all phenylalanine moieties with alanine; the resulting solution showed only random coil structure. [MARSHALL, K. E., MORRIS, K. L. *ET AL.* 2011] MAREK *et al.*, on the other hand, showed that aromatic residues affected fibrillation kinetics quite strongly in islet amyloid polypeptide (IAPP), but had no effect on the principal propensity to fibrillate. [MAREK, P., ABEDINI, A. *ET AL.* 2007]

It is conceivable that the presence of the hydrophobic dye bis-ANS serves as a “glue” by engaging in hydrophobic interactions and possibly π -stacking between adjacent fibres and along the fibre axis. This would result in three-dimensional packages of potentially very long fibres.

Furthermore, such a clustering of aggregates may well explain the low absolute surface pressures, as the compressibility of the film depends on the density of molecules per area unit. By lateral and vertical stacking of the fibres the areal requirement would be smaller, resulting in a lower surface pressure.

Following this line of argument hydrophobic and aromatic interactions between protein fibres perpendicular to the interface, mediated by the dye, would likely prove stronger than hydrophobic interactions between the protein and air. Resulting in a net force directed towards the subphase, this would increase the interfacial tension of the system and thus explain negative values for the surface pressure Π .

In other experiments of this system the drop in surface pressure into negative values is even more pronounced and the position of the isotherms along the x-axis is generally poorly reproducible. The general shape, however, persists even when the dyes concentration is changed. An example is shown in Figure 20.

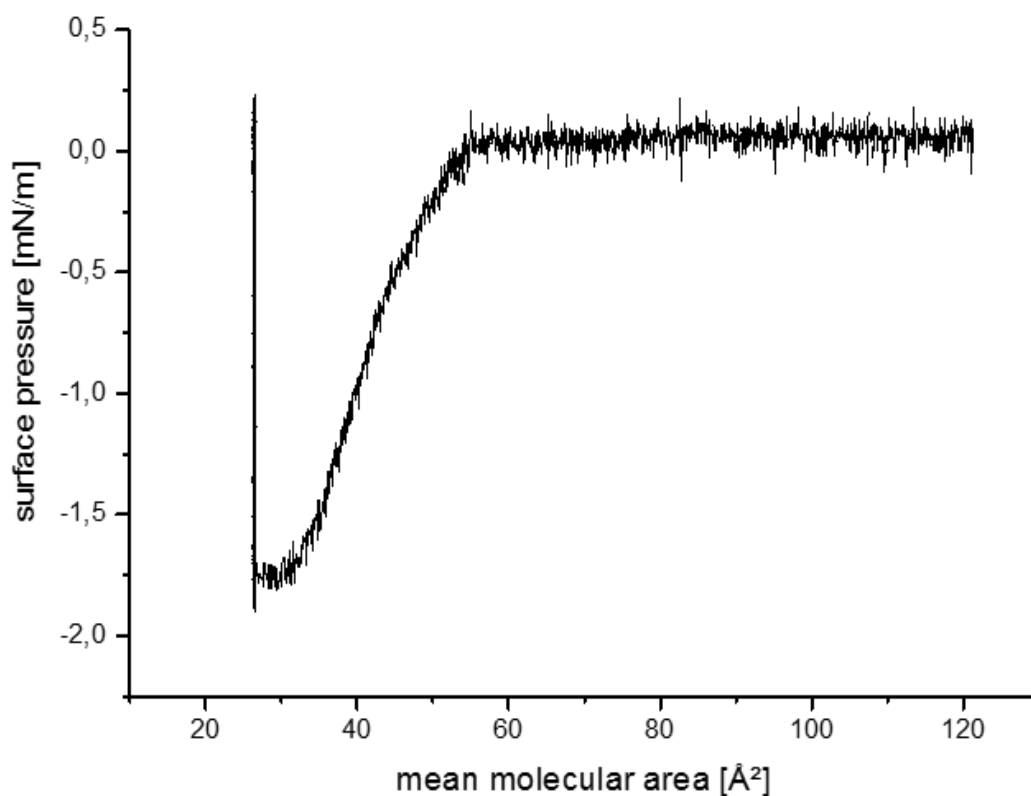


Figure 20 Compression isotherm of SC3 on a 1.4 μM solution of Bis-ANS at 20 °C.

To eliminate the influence of the dye water-soluble Rhodamine 123 (**Rh123**) was employed to monitor the undisturbed self-assembly. SHIEH and ZASADZINSKI showed that this dye preferentially adsorbed to liquid-disordered regions of lipids and had no noteworthy influence on the structure of lipid domains and compression isotherms. [SHIEH, I. AND ZASADZINSKI, J. A. 2015] Most importantly the dye itself

does not lead to an increase in surface pressure and yields sufficient emission intensity even at very low concentrations. Figure 21 shows several compression and expansion isotherms of SC3 on a 15 nM solution of Rh123 in water. Their shape generally is in agreement with the isotherms on pure water and other experiments concerning multiple cycles of constraint and relieve.

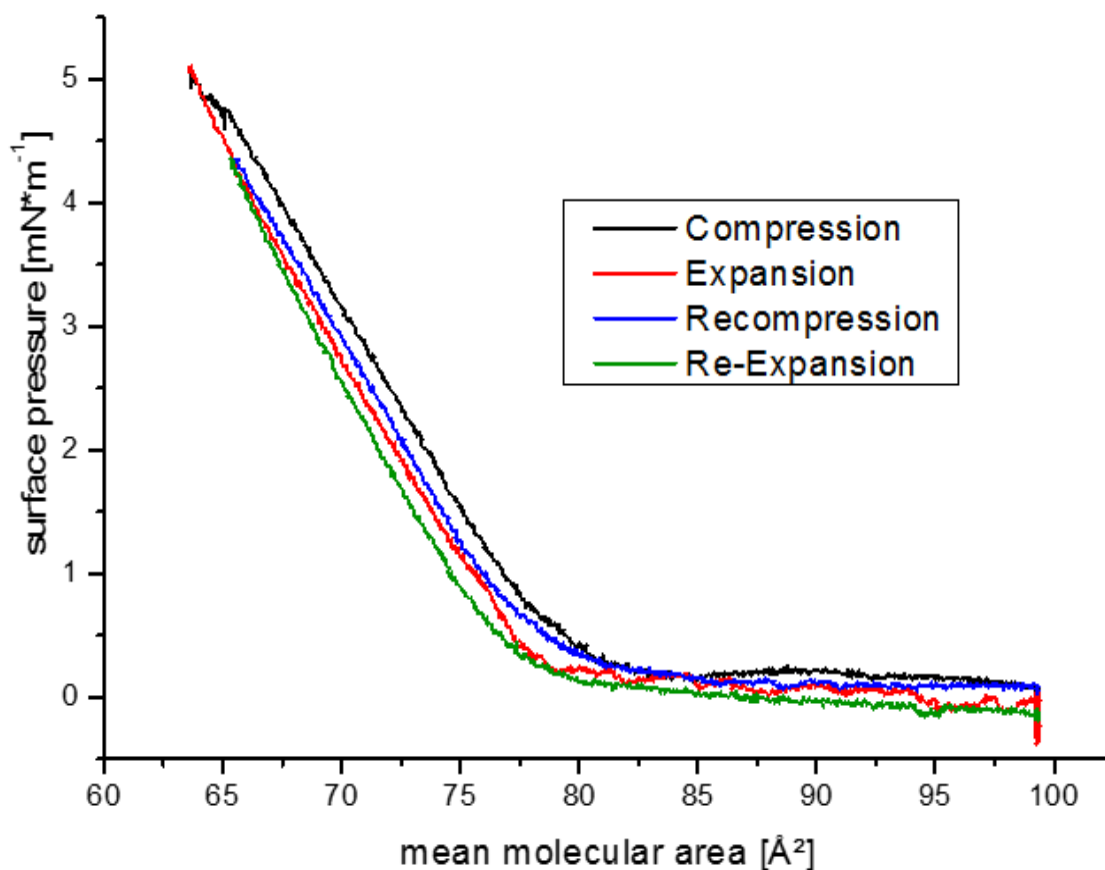


Figure 21 Compression and expansion isotherms of SC3 on 15 nM Rh123 at 20 °C. The same sample was subjected to a cycle of compression (*black*), following expansion (*red*), a second compression (*blue*) and second expansion (*green*). The third compression isotherm did not considerably differ from the second one (not shown).

Some exemplary fluorescence microscopy images of the resulting structures are shown in Figure 22.

As described in section 2.2.2 contrast is achieved by the preferential adsorption of the fluorophore to more loosely packed regions of the interface. Upon first compressing the protein, stable patches of tightly packed protein matter arise at the interface, persisting after expansion. They are mostly circular and different levels of

contrast indicate multi-layered structures that only partially disassemble when expanded. The scope of these images, unfortunately, does not allow for the detection of fibrils like the AFM micrographs.

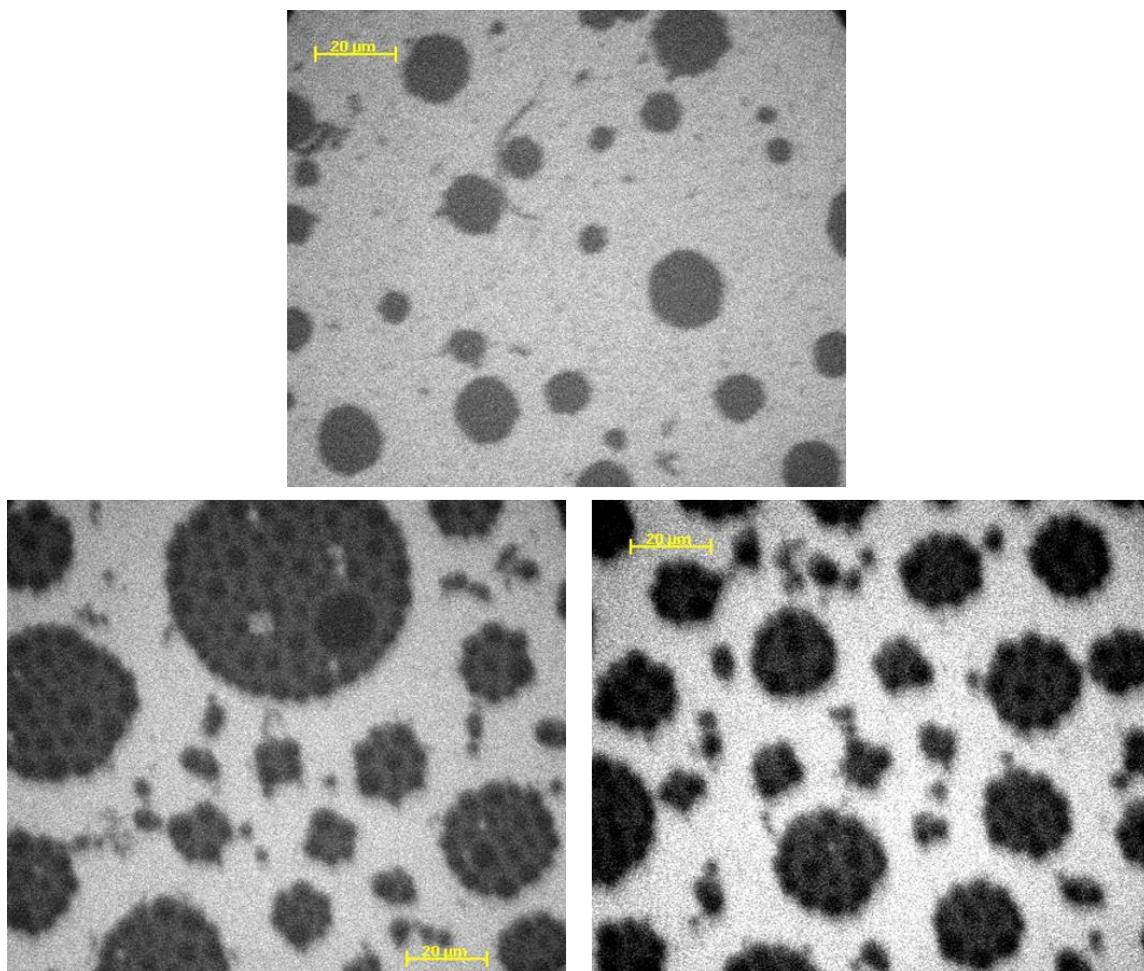


Figure 22 Fluorescence microscopy images of SC3 on 15 nM Rh123 at 20 °C. Scale bars are 20 μm . *top*: second compression; $\Pi = 1.6$ mN/m; *bottom*: third compression; $\Pi = 0$ mN/m.

Since no Langmuir-Blodgett transfer could be carried out, due to the physical setup of the microscope, the hydrophobic side of these aggregates was not imaged in AFM. It can be expected, however, that the circular ‘spots’ consist of fibres on comparable length scales.

The most notable feature, apart from the shape of the isotherm itself, is the absence of clearly visible fibre-packages of at least 100 μm length seen with the hydrophobic dye bis-ANS. This may be attributed to the origin of contrast in both systems. While

Rh123 illuminates the less densely packed regions, bis-ANS preferably binds to fibrillary aggregates, making their detection much easier.

It is, however, evident that the staining fluorophore influences the fibre formation itself. It is therefore also feasible that no such large scale packages of fibres exist when Rh123 is utilized.

Further studies on LS and LB films compressed to different extents on Bis-ANS and Rh123 solutions would provide greater insight into the exact differences in the interfacial morphology.

3.2.2 HFB2

Because spreading HFB2 resulted in elevated initial surface pressures between 1 and 6 mN/m that did not relax to zero even after stabilization for several hours, weak initial constraints could not be studied in the context of multiple compression cycles. Repeated compressions to 13 mN/m revealed a strong heterogeneity of structures.

Most notably, the dendritic structures observed during a single compression mostly dissolve when the film is expanded. In contrast to SC3, however, a closed layer of protein remained stable underneath these larger structures. After the second compression, these larger structures disappeared but the film appeared rather inhomogeneous, with small aggregates randomly distributed on top of the closed layer and several round holes in the top layer. After the third compression, several larger structures with diameters of 40 nm to between 200 and 300 nm were present, their height is in the range of 10 to 12 nm. These clusters once again mostly dissolved when the film was expanded. (See Figure 23)

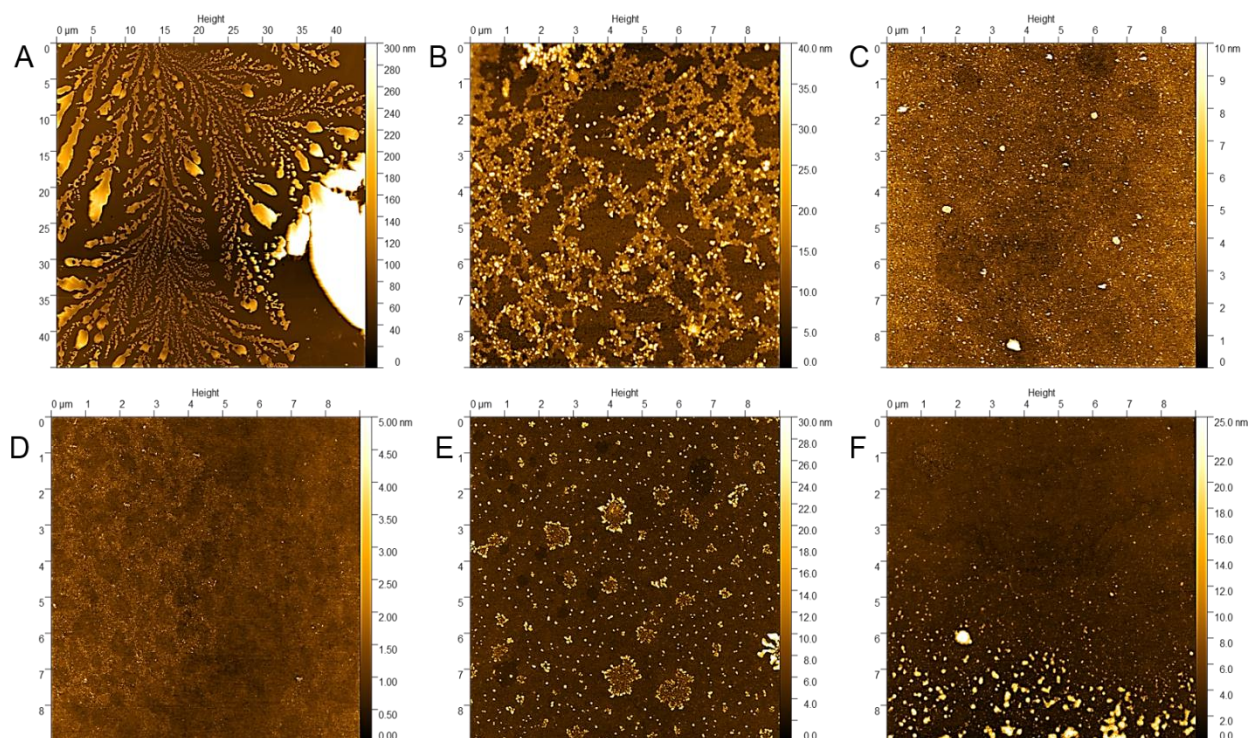


Figure 23 AFM micrographs of HFB2 transferred at 13 mN/m: **A)** 1 compression, **B)** 1 expansion, **C)** 2 compressions, **D)** 2 expansions, **E)** 3 compressions, and **F)** 3 expansions; dimensions are $9 \times 9 \mu\text{m}^2$.

Figure 24 shows the height distribution of the observed structures for up to three compressions of HFBII to a surface pressure of 13 mN/m and subsequent expansions. All compression curves are rather unimodal and the maximum shifted from about 10 to 13 nm after the first compression to about 4 nm after the third compression. The first expansion created a bimodal distribution with maxima of about 7.7 and 13 nm; the latter coinciding with the first compression maximum, which again shows the non-uniform dissolution of the film.

Coverage of the mica surface ranged from 70 % to about 95 % and did not change significantly over several cycles. It also tended to be slightly lower for the corresponding expansions, which again supports the observation that the structures dissolve in a nonuniform manner. (see Figure 25)

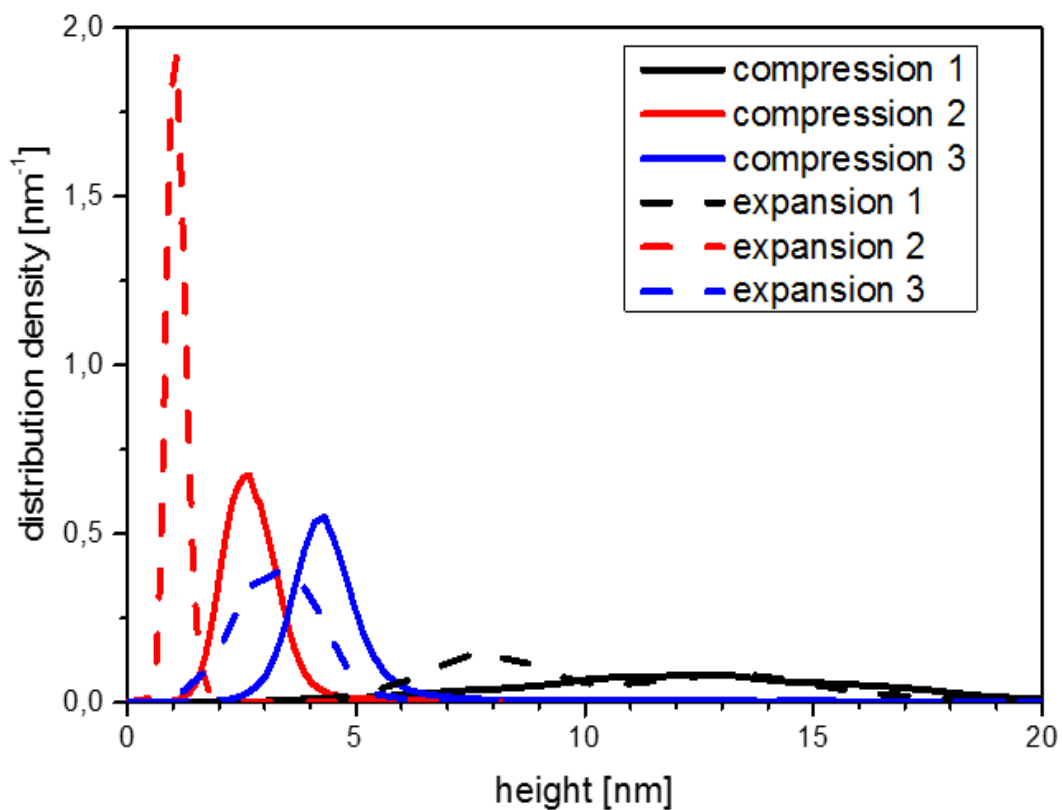


Figure 24 Height distribution of HFBII structures transferred after several compressions to 13 mN/m and subsequent expansions.

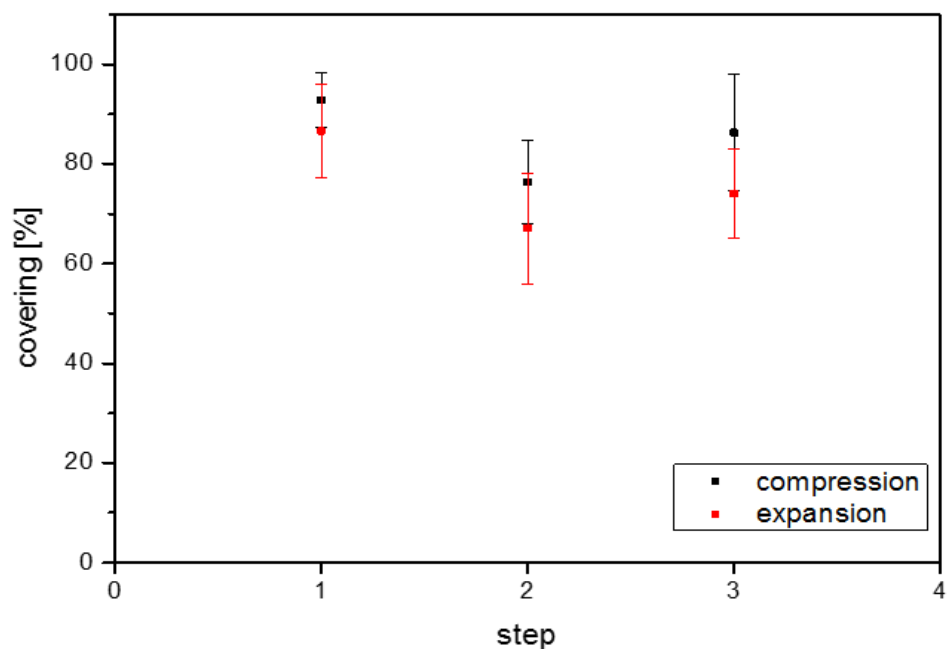


Figure 25 Coverage of the mica surface by HFBII after each compression to 13 mN/m and subsequent expansion.

3.2.3 DENDRITIC SUPERSTRUCTURES IN BOTH CLASSES

As mentioned before, the dendritic structures that constitute the predominant morphology of HFB2 films at intermediate and high surface pressures, do not persist over multiple cycles of constraint and relieve. As already shown in Figure 18 E compressing SC3 to 13 mN/m several times before transfer can occasionally give rise to structures that are very similar in height, size and general morphology.

Figure 26 presents a direct comparison between HFB2 after one and SC3 after three compressions, including cross-sections along the indicated lines. Once again, the protein layer underneath these large structures is more homogeneous for HFB2, while fibrillary assemblies predominate in SC3. Given the considerable variety of constraints at play, it is difficult to explain this phenomenon in a straightforward manner. Scouring the literature revealed that, although monolayers of several hydrophobins of either class have been studied quite extensively, the surface pressure at the air/water interface is usually well adjusted and the resolution achieved is much higher than in this work.

While these dendritic assemblies are well connected in HFB2, Figure 26 B shows interrupts in the propagation of the superstructures from SC3. This suggests dynamic assembly at differing time scales. Furthermore, in many samples of HFB2 the edges of these dendritic structures are noticeably thickened (see Figure 28), which is also indicative of kinetic effects: protein clusters coalesce at miscellaneous rates due to different evaporation rates of the residual water.

In any case, the fact that two proteins with vastly different aggregation behaviour can exhibit such striking similarities on a micrometre scale begs the question whether one can design external constraints in such a manner that specific, more complex structures that differ from the initial fibrillary and two-dimensional assemblies can be obtained.

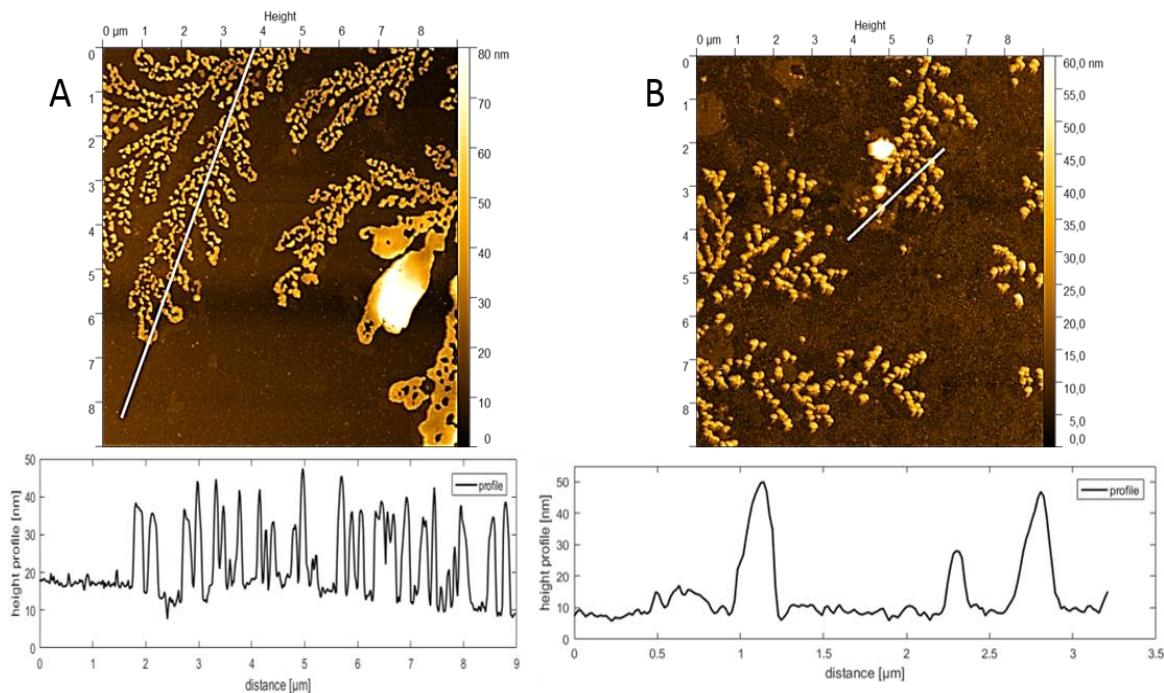


Figure 26 *top*: AFM micrographs of A) HFB2 and B) SC3 transferred at 13 mN/m after one and three compressions, respectively; dimensions are (9x9) μm^2 . *bottom*: cross-sections along the white lines, measured in direction of increasing x value. Height scales are given in nm.

Taking into account the great variety and heterogeneity still present in all samples examined in here, it stands to reason that these large dendrites have simply not been seen in these earlier studies. It is also worth mentioning once more that sample preparation is essential for the results one can obtain; as most studies were performed on small droplets of protein solution dried on solid substrate, or LB films, most commonly transferred onto highly oriented pyrolytic graphite (**HOPG**), it stands to reason that the dominant interactions between substrate and protein are fundamentally different [SZILVAY, G. R., PAANANEN, A. *ET AL.* 2007]

An interpretation of these results is therefore necessarily speculative.

3.2.3.1 Adsorption kinetics may reveal the underlying mechanisms

HÄHL *et al.* have published a study on the unusual adsorption behaviour of class II hydrophobins to the air/water interface. Their results include AFM images of LS-films of HFB1, deposited onto silicon wafers hydrophobized with self-assembled monolayers of octadecyltrichlorosilane. After contact with the interface the substrate was immediately removed again and residual water was drained off with an absorbent paper. HFB1 is structurally very similar to HFB2, differing slightly in the

molecular mass and number and position of charged side groups. While the methods applied by the aforementioned group differ considerably from the experimental strategies presented here the proposed model may be of use in explaining the observed morphology.

Globular clusters of protein matter with diameters of about 2 μm are visible in the height images, structurally similar to the dendritic superstructures reported here. The authors argue that the large clusters already represent the protein density in the final monolayer and do not fuse, due to their crystallinity, as it is unlikely that two neighbouring clusters share the same crystal orientation. [HÄHL, H., GRIFFO, A. *ET AL.* 2019]

Furthermore, the interactions between protein and solid substrate are likely much stronger in the case of hydrophobized silicon as compared to mica which inhibits two-dimensional movement of the clusters after transfer. In the compression and expansion experiments described herein these clusters, which would likely be present after spreading (see Figure 27), are forced into contact with each other and thus fuse.

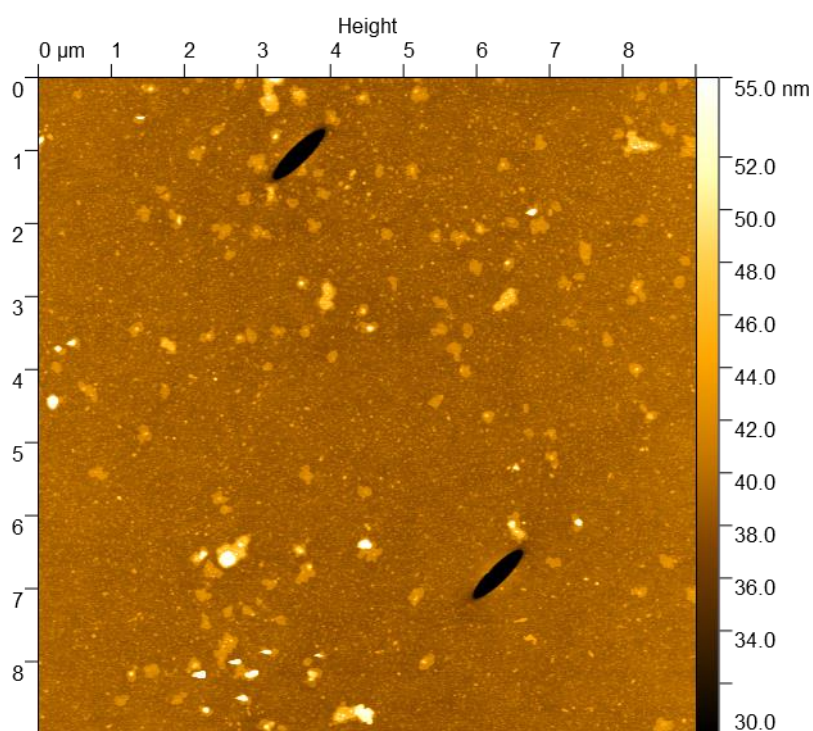


Figure 27 AFM height micrograph of HFB during the first compression; transferred at 3.3 mN/m. Dimension is (9x9) μm .

Combined with drying effects, which are described in detail in the following section, the idea of laterally mobile clusters forced into fusion explains the prevalence of superstructures built from smaller globular aggregates; it also offers an explanation for the non-uniform disassembly of the interfacial layer upon expanding the films. Forcing the existing patches into contact seems not to thoroughly fuse them together in a stable manner; hence, they disassemble when the external constraint is lifted. This model would then also explain the increasing homogeneity of protein films after several compression-expansion cycles.

3.2.3.2 Fingering instability and the *Marangoni* effect

Thin films of binary polymer solutions of different varieties and the mesoscopic dewetting of *poly*(3-hexylthiophene), to give only two examples, have produced tree-like patterns of polymer aggregates and ring-like nanoparticle chains, which have been explained as the result of a self-assembly process directed by instabilities due to sequential evaporation; which in turn leads to nanoscale inhomogeneities and –instabilities, guiding the formation of ordered structures.

[GOVOR, L. V., REITER, G. *ET AL.* 2006; GOVOR, L. V., PARISI, J. *ET AL.* 2009; KARTHAUS, O., KOITO, T. AND SHIMOMURA, M. 1999]

As KARTHAUS *et al.* pointed out, fingering instability at the three-phase-line of occurs due to the *Marangoni effect*. [KARTHAUS, O., GRASJO, L. *ET AL.* 1999] It is caused by a gradient of the interfacial tension in the vicinity of the three-phase-line. While the investigated systems differ considerably from the LS-films investigated here the underlying physics are likely very similar and can be illustrated by the following example:

The so-called “tears” of wine occur in a thin film of said beverage, rising up the glass due to capillary action. The alcohol in the liquid has a lower surface tension and higher volatility than the water and evaporates from the mixture. The resulting liquid film has a higher water content and therefore an increased surface tension, which leads to a contraction of the liquid to lower the interfacial area. The liquid is pulled up the glass until its own weight exceeds the force of this effect and droplets start to run down the glass wall again.

To reiterate: A local increase in the interfacial tension leads to a contraction of the liquid film and dewetting of the solid substrate (i.e. the glass) up to the point of

another force (i.e. gravity) restricting further contraction which then leads to the formation of droplets.

The multi-layered protein film is still covered with a water droplet directly after transfer. As the water starts to evaporate, it retracts from the hydrophobic domains of the protein and simultaneously more hydrophilic protein regions are exposed to air. This increase in protein/air interfacial tension, coupled with the proteins propensity for self-assembly, leads to a contraction of the protein film into aggregates of globular appearance. These form fractal larger-scale structures due to the inhomogeneous evaporation of the liquid, leading to the aforementioned *fingering instability*.

This assertion is backed up by the placement of these structures in Figure 28.

Several holes can be seen in the underlying film, likely caused by small gas bubbles or ripping of the film during transfer. While the fractals are relatively broad and connected by a comparatively large contact line upon the closed protein layer, protein aggregates within these holes are much thinner and more well-defined in terms of their fingering pattern. The proposed explanation is that the absence of a closed protein layer in the direct vicinity of these structures eliminates preferential protein-protein interactions, amplifying the effect of exposure to air and thus the instability. Apparently, this effect is so prominent that such dendritic structures constitute the dominant morphology in HFB2 samples at and above a transfer surface pressure of 13 mN/m.

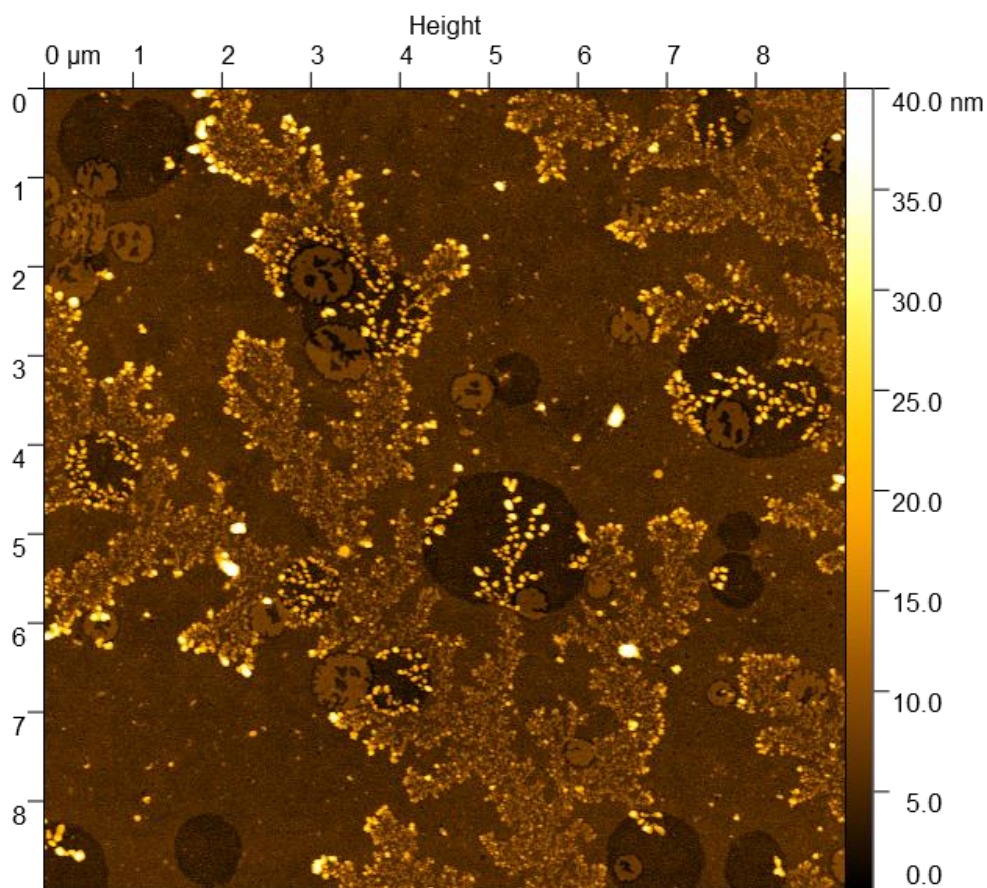


Figure 28 AFM height micrograph of HFB2 after single compression; transferred at 27.5 mN/m. Dimensions are (9x9) μm .

Additionally, the superstructures are thickened at the edges, which suggests kinetic effect during drying. Due to differences in evaporation rates the protein film ‘coalesces’ at differing rates. This observation fits well with the principal physics of the *Marangoni effect*.

The propensity of class I hydrophobins, such as SC3, to fibrillate seems to largely counteract the instability. Fibril formation, when once again understood in terms of the proposed mechanism mentioned in **section 1.1**, compacts the protein’s three-dimensional structure and thus in itself decreases the interfacial area. SC3 has a higher reported surface activity than HFB2, with surface pressures reaching up to 48 mN/m [WÖSTEN, H. A. B. 2001; ASKOLIN, S., LINDER, M. *ET AL.* 2006]

In this sense the underlying protein film has already adapted to the drying effect, leading to the inhomogeneity of its fibrillary structures seen in virtually all SC3 samples. Figure 26 B was obtained after three compressions to 13 mN/m.

Following the argument for the more defined fingered patterns in defects of the closed layer of HFB2 one could propose that the inhomogeneous layer of SC3 has a similar effect; hence, the dendritic assemblies are more well-defined than most of those seen in HFB2 samples. As touched upon briefly in **section 1.1** the closed membranes formed by HFB2, their ability to readily dissociate and the lower surface activity suggest that the two-dimensional interactions between HFB2 monomers in an interfacial layer are rather isotropic due to the proteins rigidity and ability to make favourable lateral contacts. Keeping in mind the crystallinity and orientational constraints mentioned in the previous section, this assumption should still hold on a molecular level.

In SC3, on the other hand, fibrillation is the primary process of assembly and the fibrils' amyloid-like nature necessitates directed fibre growth along a specific direction. A close look at Figure 26 B shows that the propagation of the fingered structures is interrupted at several points; the general direction of growth is consistent, however. It is likely that the dynamic self-assembly happens at varying timescales, reinforcing the notion of differing evaporation rates, driven by a competition between the 'fracturing' of the protein layer and fibrillation.

SC3 is also generally less water-soluble than HFB2, despite that fact that it is heavily glycosylated, containing an average of 17 - 24 mannose units per protein, [DE VOCHT, M. L., SCHOLTMEIJER, K. *ET AL.* 1998], which constitute about 24 % of the total protein mass. One may thus propose that the contracting effect is both less prominent in SC3, because the interfacial tension between the water soluble parts and air is lower than in HFB2; and that fibrillation acts as a secondary way of compacting the protein film that seems to dominate structure formation.

Moreover, it has been suggested that solubility is a major factor for fibre formation and stability. [SCHMITTSCHMITT, J. P. AND SCHOLTZ, J. M. 2003] It was hypothesized in this study that increased solubility should suppress fibrillation. It stands to reason that removal of the sugar would lead to a decreased solubility, which in turn should strengthen the propensity to fibrillate.

3.3 THE IMPACT OF GLYCOSYLATION ON THE COMPRESSION ISOTHERMS OF SC3

Attempts to deglycosylate SC3 as described in the experimental section were carried out; however, definitive proof of success is still missing. Qualitative assessment of the products shows a decreased solubility as evidenced by attempts to solve and separate them using SDS-PAGE. Unfortunately, mass spectrometry data could not be acquired, for reasons not uncovered yet.

Compression isotherms were monitored alongside epi-fluorescence microscopy to investigate their interfacial behaviour analogously to the native protein.

Figure 29 shows Π -A-isotherms of native and (presumably) deglycosylated SC3 for multiple compressions and expansions.

The major difference between the two is the existence of a pronounced region of decreased slope in the deglycosylated samples (Figure 29 bottom), which is also prominent in the corresponding expansion isotherms. The exact concentration of the deglycosylated species could not be determined due to its poor solubility; the total area available is therefore plotted in the corresponding figure.

Taking lipids as an analogy this suggests reversible phase transitions in the interfacial layer, attributed to conformational changes as a reaction to the increased external constraint. This can be explained by increased spatial density of monomers in the interface. The absence of sugars reduces the size of the hydrophilic part, allowing for denser packing of monomers which compensates the external constraint, leading to an increased compressibility of the interfacial layer.

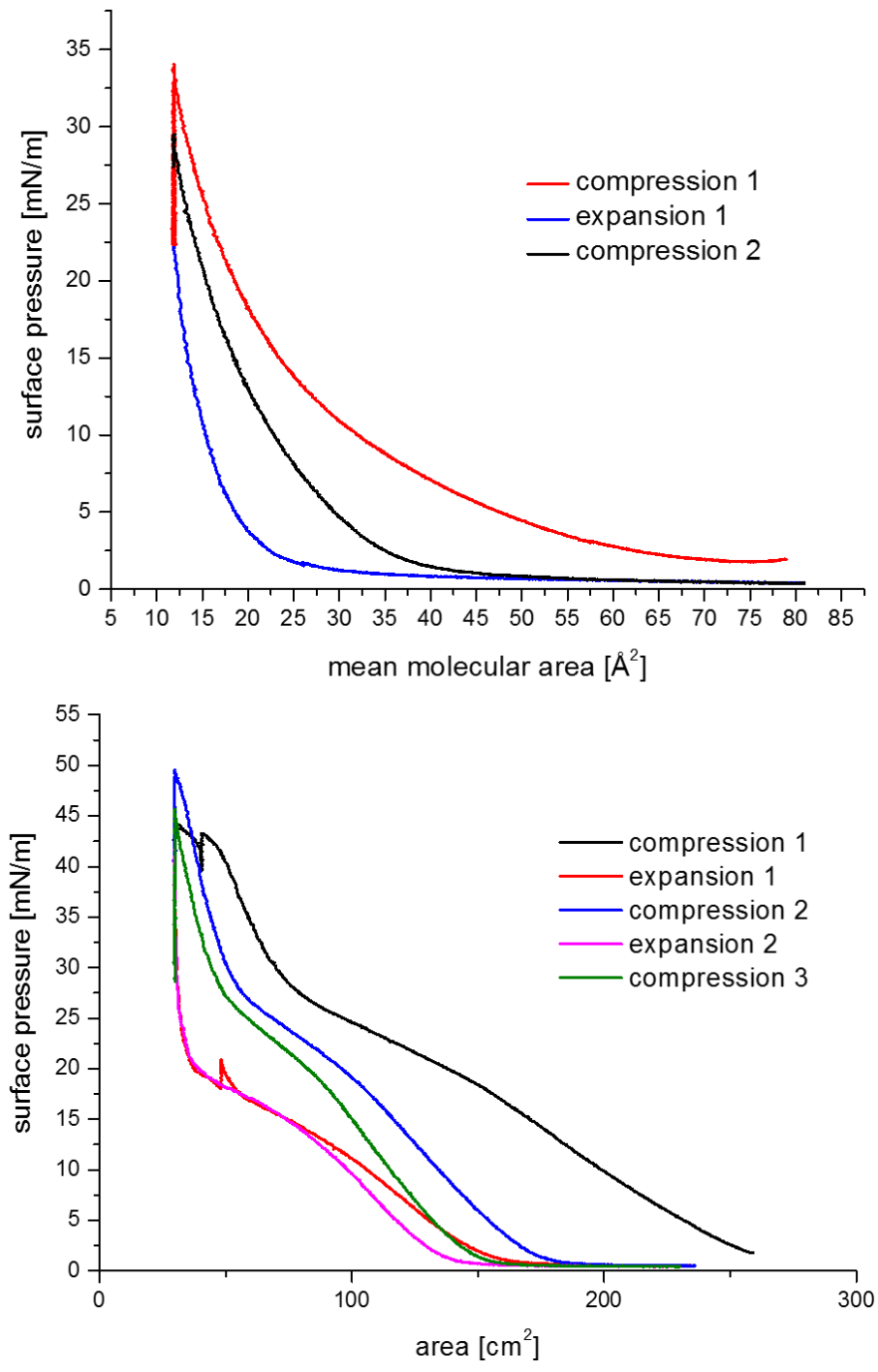


Figure 29 Isotherms of SC3 for several compressions and expansions. *top*: native SC3; *bottom*: deglycosylated SC3

Epi-fluorescence microscopy yielded significantly less contrast between regions of different packing density. Several preliminary experiments suggest that the principal aggregation behaviour is independent of the glycosylation state, which is a reasonable conclusion given that most hydrophobins are not glycosylated to begin with, yet fibrillation is the defining feature of class I hydrophobins. Instead, the loss of hydrophilicity after deglycosylation seems to affect aggregation kinetics and the larger-scale morphology of interfacial films. Further studies should also give insight into the changes in surface pressure at fixed molecular areas, as seen in the isotherms for the first compression and expansion. When the barriers were stopped during compression the surface pressure quickly decreased, suggesting reorientation of the interfacial layer to compensate for the lateral constraint. Upon expansion of the film the surface pressure increased when the barriers were stopped. Epi-fluorescence showed a pattern of large dark patches colliding. Unfortunately the contrast was too low to record usable images. The loose stacking of such large patches, although highly speculative at this point, might explain the shifting surface pressure at static area values. Upon compressing the layer patches of densely packed protein collide, reducing the compressibility of the layer. When the barriers are stopped a reorientation of the layers relaxes the film. On the other hand, expansion of the film allows for the patches to drift apart. Occupying all the available surface area, the increase in surface pressure suggests that the vertical interactions between layered patches of protein are relatively weak. However, much more detailed experimental data and analysis are needed to test this hypothesis.

3.4 SUMMARY, CONCLUSIONS AND OUTLOOK

Hydrophobins have previously been described as the most surface active proteins known. [WÖSTEN, H. A. B., VAN WETTER, M.-A. *ET AL.* 1999] Extensive research has been conducted on their self-assembly at hydrophilic/hydrophobic interfaces, especially the air/water interface. It has further been established that class I hydrophobins primarily form rodlets or fibrils akin to amyloids which can adhere very strongly to numerous surfaces, while class II members form rather homogeneous membranes that dissociate more readily. In virtually all studies investigating the morphology of self-assembled structures the experimental conditions, such as surface pressure and compression state, were well adjusted and a high resolution of a few hundred nanometres were usually achieved. In this chapter larger scale morphologies of LS-films and the effect of multiple cycles of constraint and relief are discussed.

3.4.1.1 Single compression to various surface pressures

Lateral constraints were shown a significant impact on the observed morphology for both proteins. Fibrillary aggregates formed by SC3 are present in LS-films transferred at various surface pressures, even at very low constraints. Their height distribution shifts with increasing transfer pressure from a bimodal distribution at low and intermediate transfer pressures to a rather homogeneous distribution centred around 5 - 6 nm at the highest transfer pressure achieved, which was 27.5 mN/m. The apparent length and width of these fibrils follows no clearly visible trend. Coverage of the mica surface quickly increased to a stable value near 100 % at surface pressures above ~ 13 mN/m. No significant stacking into multilayers was observed.

HFB2 assembles into remarkable microscopic structures at transfer pressures of 13 mN/m and above. Dendritic assemblies of globular clusters several microns in length constitute the predominant morphology; and these superstructures are always present on top of a closed protein layer. Contrary to SC3 the height distribution for HFB2 starts well defined at values around 2 nm when transferred at 3.3 mN/m and broadens significantly, shifting to an average of 42 nm, when transferred a 10 mN/m. At the highest transfer pressure achieved (25 mN/m) the height

distribution stabilizes at about 5 nm. This, however, may well be an artefact of sample preparation, caused by “ripping” the film in its highly compressed state from the interface and subsequently subjecting it to capillary forces upon drying.

While no large-scale structures like the ones discussed herein have been reported in contemporary literature, the general results of film balance measurements and AFM imaging are in very good agreement with the established classification of Hydrophobins. Furthermore, even for single compressions, the subsequent expansion isotherms exhibit a strong hysteresis, indicating a non-uniform disassembly of the interfacial films for both proteins.

3.4.1.2 Multiple cycles of constraint

Multiple compression and expansion cycles have a major influence on the morphology of interfacial structures for both classes. In both cases the interfacial films tend to become more homogenous when compressed and expanded several times. Neither of the protein films dissolved uniformly upon expansion; rather large clusters of densely packed material remained beside void areas without protein coverage. Despite no clearly visible trend in the height distribution for SC3, the fibrils shortened drastically over multiple compressions. The coverage of the substrate surface stabilized at close to 100 % when the film was compressed to a surface pressure of 13 mN/m. HFB2 shows dendritic morphology when transferred to mica at surface pressures of 13 mN/m and above. These large structures, which may have heights of more than 40 nm, are not present when the film is compressed multiple times. Generally speaking the films are more homogeneous when transferred in a state of higher lateral constraint.

In some cases “fractured” layers of protein aggregates and dendritic structures very similar to those prevalent in HFB2 could be observed in LS-films of SC3 after several compressions before transfer. While these fingered morphologies are usually quite large in HFB2 they occasionally were found to be just as filigree when observed inside defects of the underlying closed protein layer. An attempt to evaluate this phenomenon qualitatively introduces a combination of recent findings, showing stable unfusing clusters of monolayered protein that are forced into contact by

the lateral constraint, and the *Marangoni effect*, whereby the evaporation of water from the freshly transferred film subjects the hydrophilic regions of the protein clusters to air, resulting in a complex multiphase system of both parts of the amphiphile, mica, water and ambient atmosphere. This leads to a contraction of protein matter, accompanied by their propensity to self-organize, into fingered structures of several micrometres in length and width. The tendency of class I hydrophobin SC3 to fibrillate results in an entirely different situation; however, the presence of comparable fractured morphologies suggests that the latter effect also takes place.

Figure 30 illustrates the emergence of said dendritic structures in both proteins depending on their subjection to lateral constraints: cycles of compression and relaxation for SC3, increasing lateral constraints for HFB2.

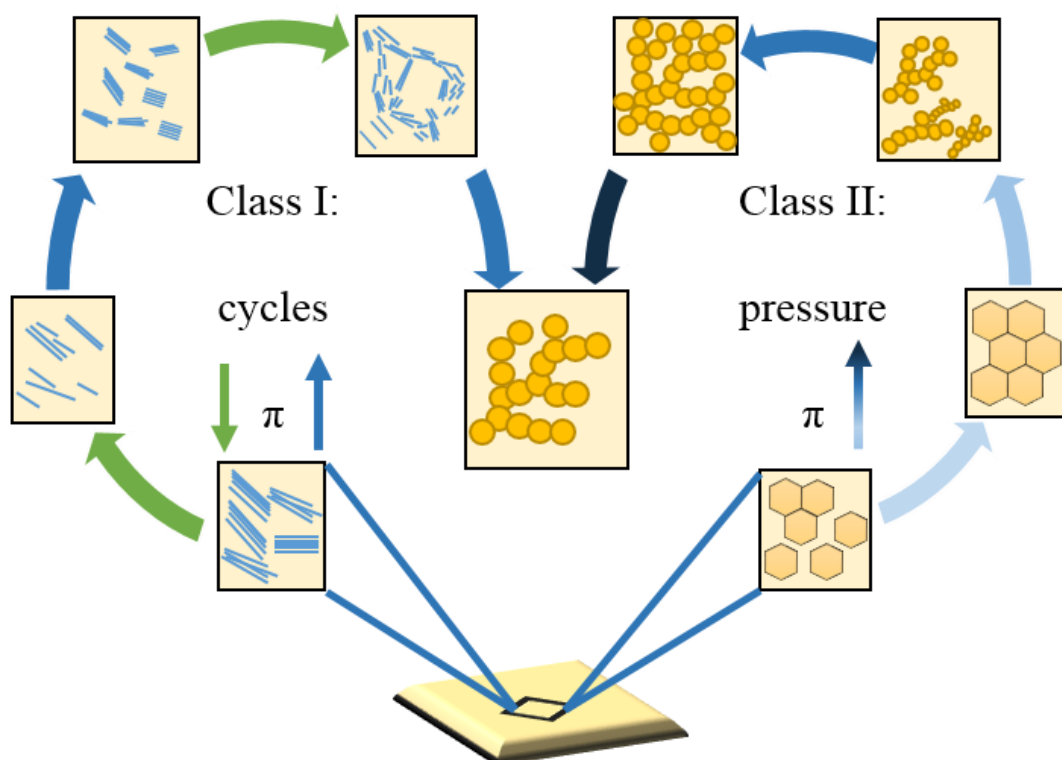


Figure 30 Schematic depiction of emergent dendritic structures. *Left:* Class I hydrophobin SC3 forms fibrils that persist during expansions (green arrows) and shorten over multiple cycles until dendritic superstructures emerge. *Right:* Class II HFBII forms closed membranes that transition into large dendritic aggregates at transfer pressures of 13 mN/m and above.

It is conceivable that this phenomenon occurs specifically in LS-type films wherein the hydrophilic part of the protein is gradually subjected to the gas phase. Imaging of the hydrophobic side, for example by LB-transfer, on a scale of several micrometres could not be found in contemporary literature.

3.4.1.3 Outlook

A quantitative characterization of the underlying processes under multiple mechanical constraints is key to fine-tune these interfacial layers for technical application. Given that two proteins with fundamentally different aggregation behaviour can result in similar microscopic structures under certain conditions, one may speculate that despite the empirical separation of hydrophobins into two classes their self-assembly can be guided by external constraints to achieve similar structures on different scales. Possible experimental approaches to characterize these fingered structures include, to name just a few, neutron or X-ray scattering to determine the ordering of proteins within the globular aggregates and between these assemblies, circular dichroism spectroscopy to investigate the secondary structure elements of the proteins within these aggregates and ellipsometry to determine optical constants, film thickness, roughness and other material properties connected to changes in optical response. Preliminary experiments suggest an influence of the glycosylation state of SC3 on the aggregation kinetics. The successful deglycosylation by mass spectrometry, epi-fluorescence and AFM imaging of the interfacial morphology need to be verified and investigated in detail to provide insight into the exact role of the sugar moieties on the interfacial behaviour. If the mechanisms of self-assembly of deglycosylated SC3 can be understood in detail, the moieties that formerly carried sugars could be used as target sites for fusion compounds with various polymers, opening up enormous potential for surface modifications and material design in a plethora of applications.

4. IN SOLUTION – INTERACTION WITH PHOSPHOLIPID

VESICLES

The formation of regular structures by self-assembly in aqueous environments at various length scales is a ubiquitous feature of diverse natural systems. [WHITE-SIDES, G. M. AND GRZYBOWSKI, B. 2002]

Amphiphiles, such as phospholipids or simple surfactants, are known to assemble into a variety of structures in solution while also showing adsorption to available interfaces. In the case of hydrophobins, especially SC3 as the most widely studied member, assembly in solution is believed to be the starting point for interfacial assembly. [WANG, X., GRAVELAND-BIKKER, J. F. *ET AL.* 2003; CORVIS, Y., BREZESINSKY, G. *ET AL.* 2006] Zykwińska and co-workers showed that SC3 assembles into nanorods in aqueous solution and that this process could be directly controlled by ionic strength and pH. [ZYKWINSKA, A., GUILLEMETTE, T. *ET AL.* 2014]

Understanding the phenomena of the self-assembly process for hydrophobins and their interactions with complex structures in solution, especially regarding their adaptive roles during the fungal life cycle, is one key element to harness their potential.

Confining the self-assembly to the quasi two-dimensional air/water interface allows for precise control over a number of experimental parameters, such as available area, lateral constraints, compression speed and interactions with solid substrates in the case of AFM studies.

In bulk, however, a much more complex situation arises. While a lot of experimental parameters, such as ionic strength, temperature and pH, can be precisely tuned and the variety of liquid/liquid interfaces open for study is manifold, these parameters are usually interdependent which hinders untangling the influence of their individual impact.

The main focus of this chapter is the interaction of hydrophobins with phospholipid vesicles as a simple model for lipid bilayer membranes in aqueous solution.

Dynamic Light Scattering was used to determine particle size distributions of the proteins, vesicles and mixtures to discern whether interactions occur in the first place.

Continuous wave Electron Paramagnetic Resonance (**cwEPR**) spectroscopy was applied to investigate the local environment of a paramagnetic probe on a molecular level. Three different approaches were taken to introduce such a species into the system, allowing for different viewpoints on the mechanisms taking place. These can be thought of as

- 1) the perspective of a guest molecule inside the vesicle subject to perturbations of its environment by introducing 16-DSA into the phospholipid vesicle,
- 2) a view from the interior of the vesicle itself by using a spin-labelled phospholipid as part of the bilayer, and
- 3) a view from the protein's perspective as an interacting agent by using spin-labelled HFB2.

4.1 *MIXED VESICLES OF POPC AND 16-DSA – THE GUEST'S PERSPECTIVE*

The first approach taken was to introduce the paramagnetic probe into the vesicle as a guest molecule. Not fixed to either species directly involved in the interaction, this allows for an “outside” perspective on the environment surrounding the phospholipids and proteins. To this end 16-DSA was incorporated into POPC vesicles as described in section 2.6. To verify the successful mixing two different ratios of POPC to 16-DSA were chosen and cwEPR spectra were recorded and compared to those of the probe in aqueous solution (see Figure 31). The vesicles with a lower ratio (Figure 31 **top**; *black* curve) give a spectrum very similar to that of free 16-DSA, although the inclination of the baseline is indicative

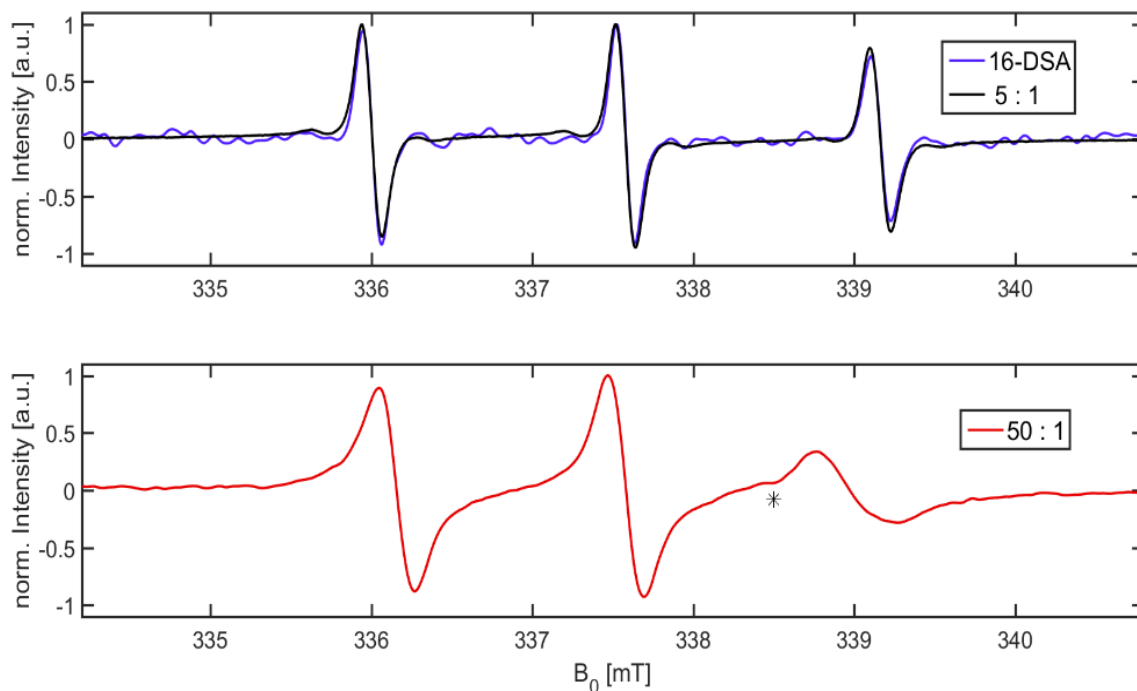


Figure 31 cwEPR spectra of mixed vesicles with POPC : 16-DSA ratios of 50:1 (red; bottom) and 5:1 (black; top) compared to 200 μ M 16-DSA (blue; top) in water recorded at 20 °C. * marks a tube artefact.

of slower diffusion. It is likely that some of the spin probe is located inside the vesicles while a portion is excluded. Because freely rotating 16-DSA gives very strong signals, even a minor fraction (e.g. 2 %) can obscure the slower components. At a ratio of 50:1 the resulting spectrum shows Heisenberg exchange and a slower diffusion rate of the spin probe, indicating that 16-DSA is indeed incorporated into the liposome.

The signal at ~ 338.5 mT, marked by an asterisk (*) in the bottom graph of Figure 31, is the result of a defect electron in the spectrometers leading tube.

To determine whether either protein interacts with the vesicles different mixtures were prepared and analysed with DLS at 20 °C. Figure 32 shows the resulting intensity weighted particle size distributions.

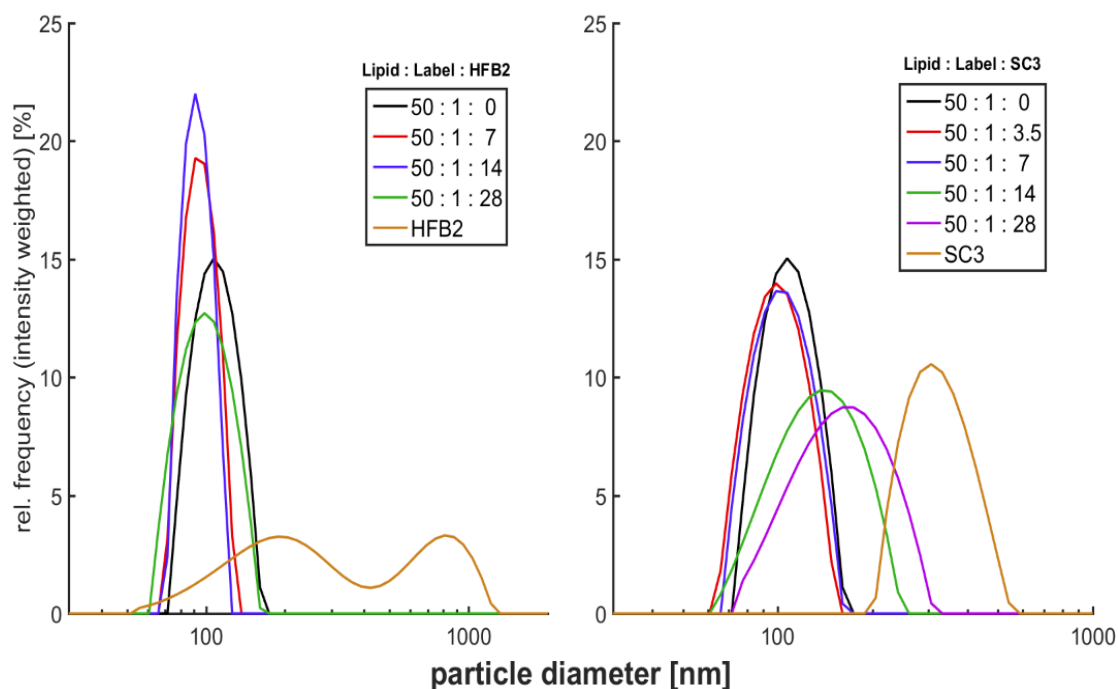


Figure 32 DLS traces of mixed vesicles with varying amounts of HFB2 (*left*) and SC3 (*right*), recorded in water at 20°C and a scattering angle of 90°

In both cases the addition of relatively small amounts of protein lead to a broadening of the distribution towards smaller diameters. While pure HFB2 shows a very broad size distribution with several maxima that includes the relevant diameters of about 50 to 80 nm, SC3 does not. Therefore, the DLS data strongly indicates an interaction between SC3 and the vesicles, while being inconclusive for HFB2.

With increasing amounts of protein the distribution shifts towards larger particles which might simply be a mixing effect of vesicles and large protein aggregates that cannot be resolved by DLS.

However, X-Band EPR spectra of all the mixtures confirm an interaction between both proteins and vesicles.

Figure 33 shows both the complete spectra and the high field lines of mixed vesicles with varying amounts of HFB2. Even at very low concentrations of protein the hyperfine coupling increases, line broadening is reduced and a more mobile component emerges with rising contribution the higher the protein content.

Simultaneously, the positive part of the high field line for pure vesicles decreases. That means that upon interacting with the protein, a second, more mobile popula-

tion of 16-DSA appears while some of the spin probe is unaffected. This is indicative of a *static inhomogeneity*, where two species of spin probe experiencing different local environments are present, no probe molecules are exchanged between species on a relevant time scale and the fraction each component represents is a function of protein concentration. Such nanoscale inhomogeneities have, for example, been studied in responsive polymers. [KURZBACH, D., JUNK, M. J. N. AND HINDERBERGER, D. 2013]

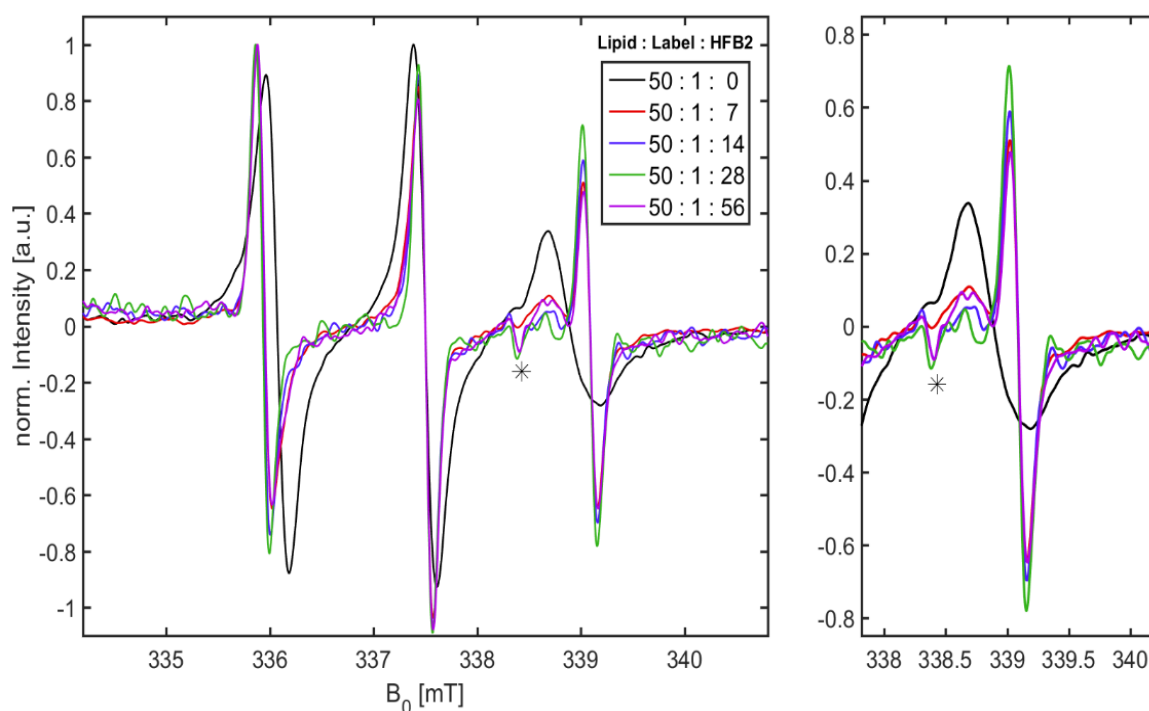


Figure 33 cwERP spectra of mixed vesicles with varying amounts of HFB2 in water recorded at 20°C. *left*: full spectra; *right*: high field lines. * marks a tube artefact.

This notion of an irreversible release of spin probe from the vesicle was reinforced by computational simulations, which represent the spectra reasonably well by assuming two components with fixed hyperfine coupling and diffusion tensors, simply changing the ratio between the two. (see Figure 34)

It should be noted that the spectrum without any protein was approximated with a single component to simplify computations. The aforementioned tube artefact, marked by an asterisk (*), was not considered in the simulations.

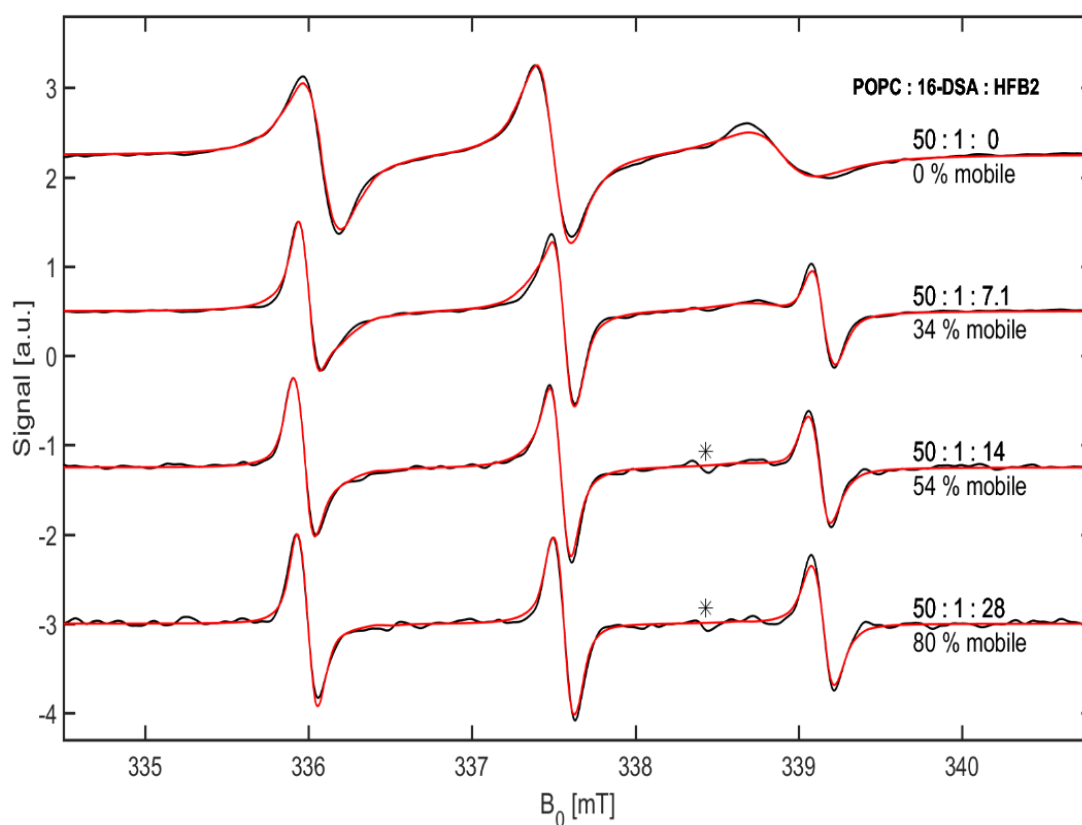


Figure 34 experimental (*black*) and simulated (*red*) spectra of mixed vesicles for varying amounts of HFB2. The assumed fraction of the mobile component is indicated for each spectrum. Spectra are offset along the signal axis for comparability. * marks a tube artefact.

Interaction between mixed vesicles and SC3 also shows the emergence of a more mobile component (see Figure 35). Upon closer inspection, however, the situation is not quite as simple as it was with HFB2. The overall increase in spectral width is less than it was for HFB2, and the right hand side of Figure 35 shows that the high field line's intensity of the mobile component emerging at a low protein concentration (red curve) decreases with rising protein content. Meanwhile the part of the high field line that belongs to the more hindered component increases in intensity and its maximum shifts to higher magnetic field values until eventually the two signals merge into a single line at a lipid:protein ratio of 50:28. This spectral change indicates a *dynamic* inhomogeneity. Once again, two populations of 16-DSA experiencing different environments are present, but individual molecules diffuse rapidly between regimes, leading to an averaged hyperfine splitting and diffusion rate.

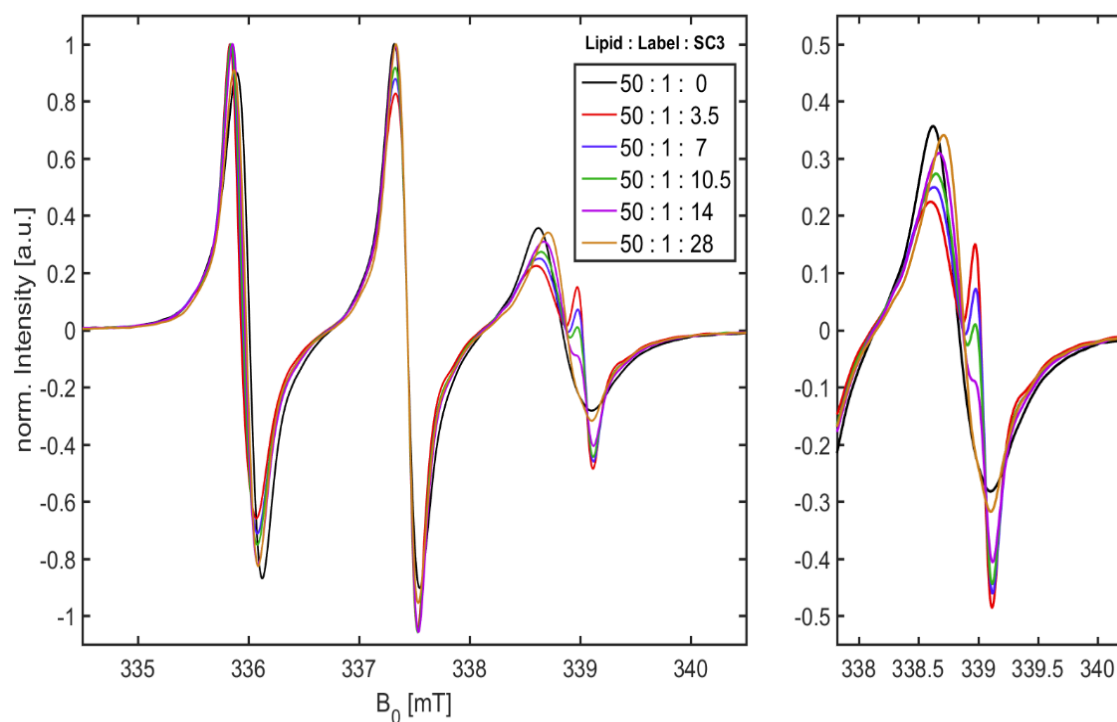


Figure 35 cwERP spectra of mixed vesicles with varying amounts of SC3 in water recorded at 20°C.
left: full spectra; *right:* high field lines

Simulations of spectra for the pure vesicles and the highest lipid:protein ratio were carried out analogously, approximating each spectrum with a single component, as shown in Figure 36.

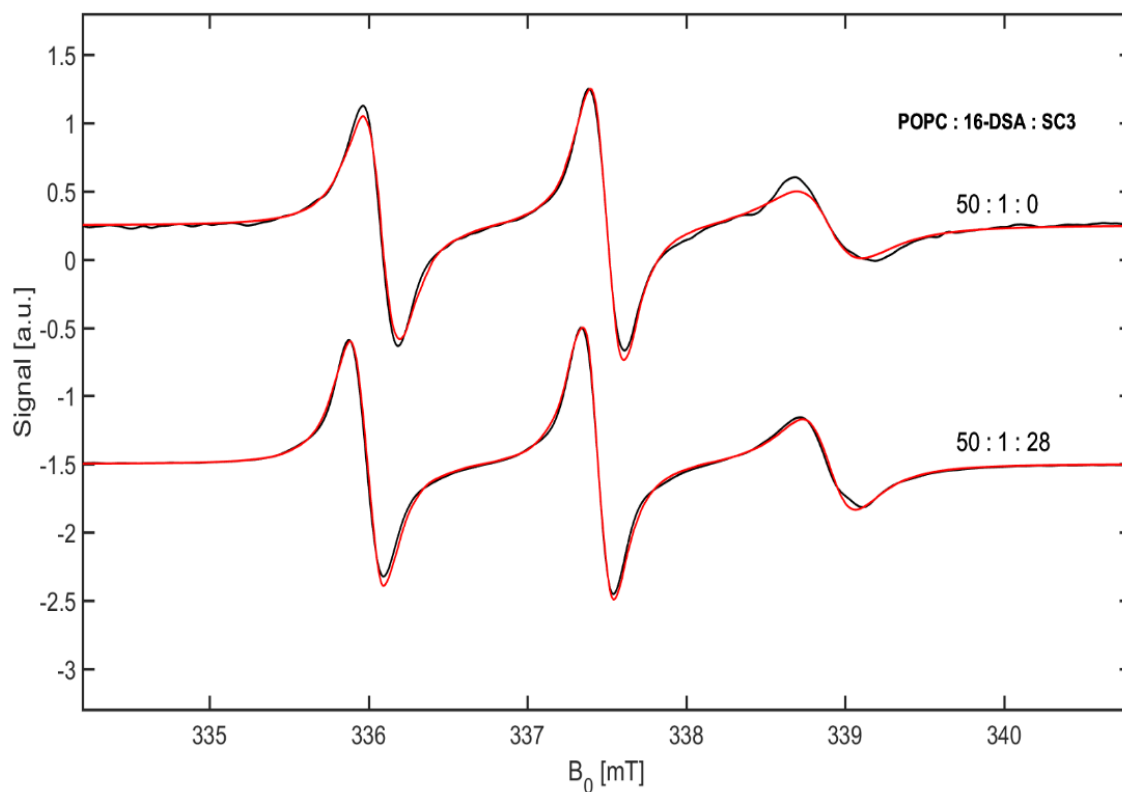


Figure 36 experimental (*black*) and simulated (*red*) spectra of mixed vesicles. *top*: pure vesicles *bottom*: containing 8 g/L SC3. Spectra are offset for clarity.

The applied simulation parameters for the g-tensor and hyperfine coupling tensor elements and calculated rotational correlation times and root means square deviation (rmsd) values are summarized in Table 6.

Table 6 simulation parameters for spectra shown in Figure 36.

parameter	pure vesicles	with SC3
$[g_{xx} \ g_{yy} \ g_{zz}]$	[2.0097 2.0065 2.0025]	[2.0097 2.0066 2.0025]
$[A_{xx} \ A_{yy} \ A_{zz}]$ [MHz]	[10.35 10.35 98.8]	[12 12 98.8]
τ_c [ns]	1.38	0.99
rmsd [%]	2.80	1.99

It should be noted that, while the values of the g-tensor differ slightly, the resolution in the X-Band limits the precision of this parameter. The values shown here were adjusted to match simulations and experimental spectra.

The hyperfine coupling values of the sample containing SC3 are noticeably larger, indicating a more polar environment of the probe, and the average rotational correlation time is about 28 % smaller. Furthermore, while the rmsd is comparable between spectra, the one component approximation fits the sample containing protein better, which is also visibly true in the high field lines matching more closely. These findings reinforce the notion that the interaction of SC3 with mixed vesicles leads to a *dynamic inhomogeneity*.

Class I hydrophobins, such as SC3, are generally more flexible than their class II relatives, and often contain extensive loops that are believed to be involved in their fibrillation. Moreover, SC3 is heavily glycosylated, with an average of 24 mannose units per monomer that constitute an additional flexible part. Class II HFB2, on the other hand, is more rigid. Starting at this generalization, the following explanation for the differences shown in this section is proposed:

When class II hydrophobin HFB2 interacts with the vesicle shell 16-DSA is released into the surrounding water. Because of its relative rigidity the protein then ‘caps’ the vesicle shell barring the spin probe from re-entering the phospholipid bilayer.

The more flexible class I hydrophobin SC3 creates a fluctuating environment, allowing for fast diffusion of the spin probe between the surrounding water and the lipid bilayer. This ensemble of environments makes for a dynamic inhomogeneity. A number of concerns arises that will have to be addressed in future studies:

Firstly, the aggregation state of either protein in these systems is unknown. WANG *et al.* have concluded that SC3 exists primarily in its monomeric form in pure water and that these monomers form structured dimers rapidly and efficiently without changing the protein’s fundamental structure. These dimers are believed to be the fundamental building block of interfacial self-assembly. However, ‘interfacial’ in this context generally refers to hydrophilic/hydrophobic interfaces like the air/water, oil/water or a liquid/solid interface. [WANG, X., GRAVELAND-BIKKER, J. F. *ET AL.* 2003] Whether further self-assembly occurs and if it produces similar structures at a ‘water/vesicle’ interface is currently unknown. The notion of a structured dimer with an unaffected fundamental protein conformation fits the dynamic nature of the

inhomogeneities reported in this chapter well, although conclusive evidence is yet to be found.

PAANANEN *et al.* proposed a well-defined four-armed structure for HFB2 in aqueous solution at concentrations above 0.5 mg/mL (corresponding to a lipid : label : HFB2 ratio of 50 : 1 : 3.5), up to 100 mg/mL. Again, a well-defined structure of comparatively rigid protein multimers fits the explanation offered for the occurrence of a static inhomogeneity, but conclusive evidence has not been found yet. [PAANANEN ET AL., 2003]

Secondly, the protein concentrations chosen in this work are relatively high. The lower concentration limit for both proteins, at which the effects described here can be observed, are unknown; as is their correspondence with the proposed respective critical aggregation concentrations. Lastly, HFB2 und SC3 are two excessively studied hydrophobins and often serve as ‘prime examples’ for their respective class. If the effects reported here are specific to these proteins or features common to the respective class of hydrophobins they belong to is currently unknown.

4.2 SPIN-LABELLED PHOSPHOLIPIDS – THE VESICLE’S PERSPECTIVE

The second approach was to utilize a spin-labelled phospholipid as part of the lipid bilayer to investigate the effect of the protein’s presence on the bilayer itself. To this end, PDSPC was added to POPC in different ratios and then extruded into vesicles (henceforth referred to as PDSPC vesicles) of 100 nm in diameter as described in section 2.6.

Ratios between the POPC and labelled phospholipid of 5:1 and 50:1 were chosen, respectively, and the size distribution was determined by DLS for two different scattering angles as shown in Figure 37.

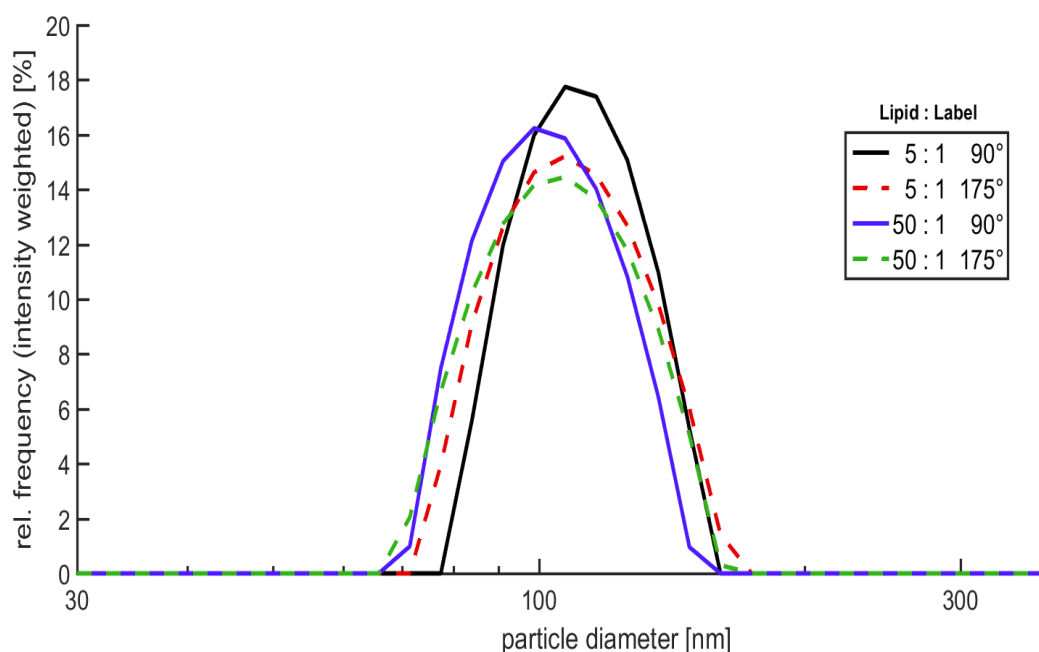


Figure 37 Particle size distribution of PDSPC vesicles of varying composition in water at 20 °C. The scattering angles were 90° (‘side’, *solid lines*) and 175° (‘back’, *dashed lines*)

No clear differences are visible between compositions and scattering angles, indicating that the labelled phospholipid is integrated smoothly into the bilayer.

Yet, a ratio of 5:1 is poorly suited for EPR measurements, because the high concentration leads to many collisions between radicals and thus frequent Heisenberg spin exchange, complicating evaluation and interpretation. (see Figure B - 1 in the appendix) In general all the measurements of spin-labelled phospholipids yielded the lowest signal-to-noise ratios of the three approaches taken.

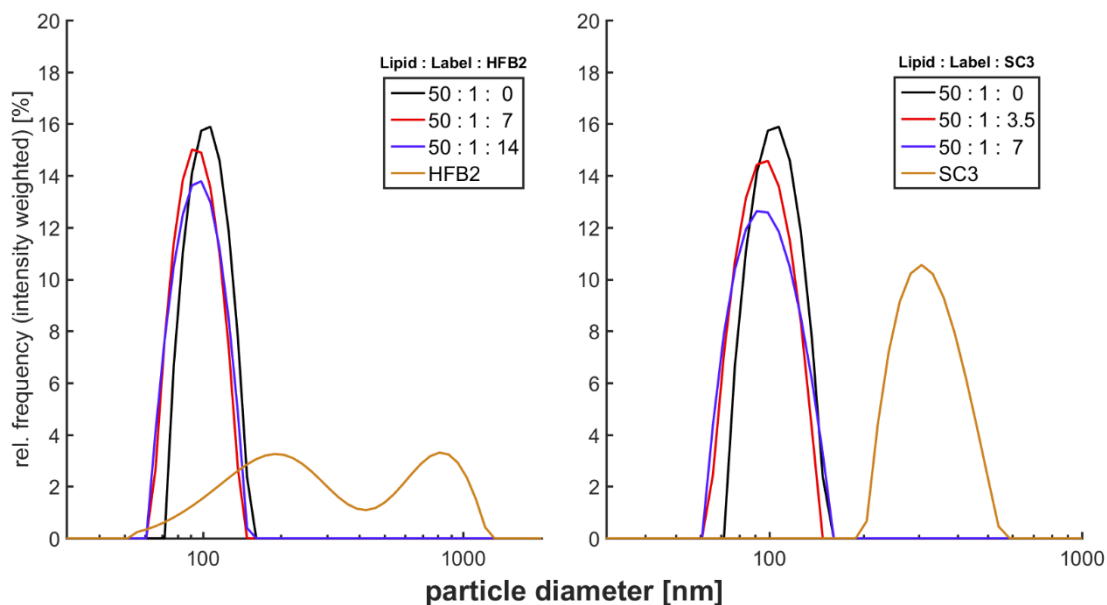


Figure 38 DLS traces for vesicles containing spin-labelled phospholipids with varying amounts of HFB2 (*left*) and SC3 (*right*) recorded in water at 20 °C and a scattering angle of 90°

The DLS traces for mixtures with either protein (see Figure 38) follow the same trend as the mixed vesicles containing 16-DSA, with the distribution getting broadened in a similar fashion for both proteins.

EPR spectra of vesicle solutions containing either protein reveal no major changes in the general lineshape. Figure 39, however, shows that the decrease of the S/N ratio is more prominent for HFB2.

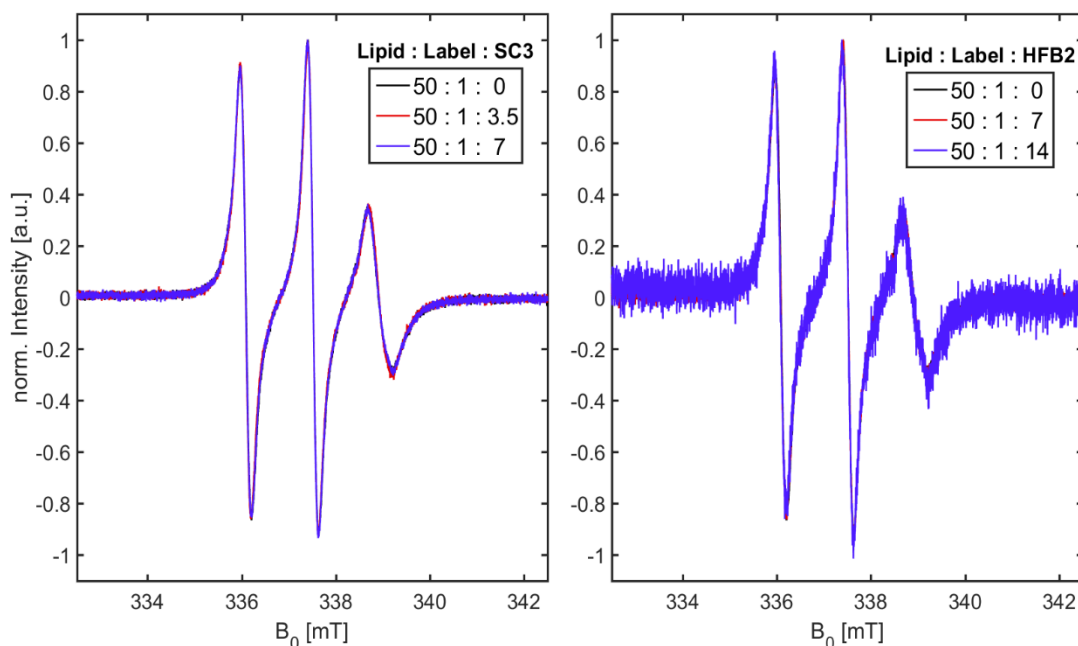


Figure 39 cwEPR spectra of PDSPC vesicles with SC3 (*left*) and HFB2 (*right*) recorded in water at 20 °C.

Since the spectral shapes are generally unaltered by the presence of either protein the lipid state inside the vesicle seems to be unaffected by the interaction of the two. This seems to be the case for both proteins.

A power sweep was performed on all mixtures in order to elucidate whether the decline of the S/N ratio is a saturation effect. In this experiment the incidental microwave power is increased between the recordings. Excessive microwave power leads to line broadening and loss of intensity. Plotting the signal amplitude versus the square root of the applied microwave power gives the saturation curves; and microwave power should be chosen within its linear section. All spectra were recorded with 4.79 mW incidental microwave power, giving a square root value of 2.188. All saturation curves can be found in the Appendix. The applied microwave power falls within the linear range of the plot and thus power saturation is not a plausible cause for the decrease in S/N ratio. Currently there is no definitive answer to this problem.

4.3 *SPIN-LABELLED HFB2 – THE PROTEIN’S PERSPECTIVE*

As described in section 2.6 HFB2 was labelled with 5-MSL to provide insight into the direct molecular environment of the protein monomer. Since attempts to covalently attach a spin label to SC3 were unsuccessful, only the class II hydrophobin could be investigated in this way. The particle size distributions shown in Figure 40 establish a general trend that subsequent experiments discussed in the following sections exhibit as well, indicating that the label does not significantly impact the interaction between protein and vesicle.

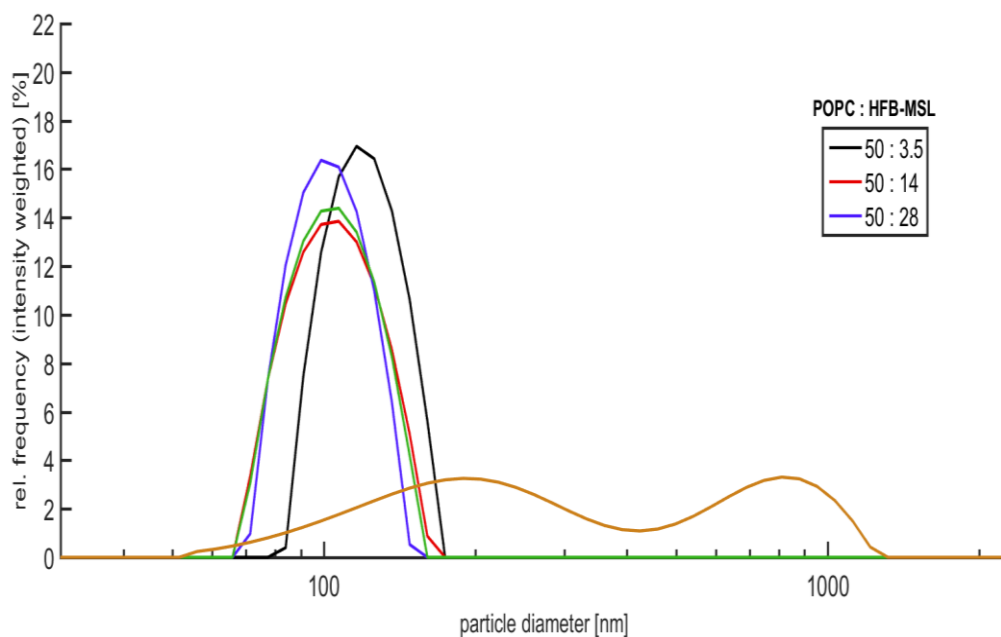


Figure 40 Particle size distribution of POPC vesicles with different amounts of spin-labelled HFB2 recorded in water at 20 °C and a scattering angle of 90°

It was stated in **section 2.6** that positions 40Q and 46K of HFB2’s primary sequence lie in the helical region that constitutes the hydrophilic part and all other valid target sites for the attachment of 5-MSL are part of the central beta-barrel. Although the exact locations of the attached labels are unknown the consistency of the spectra indicates that HFB does not completely penetrate the vesicle shell.

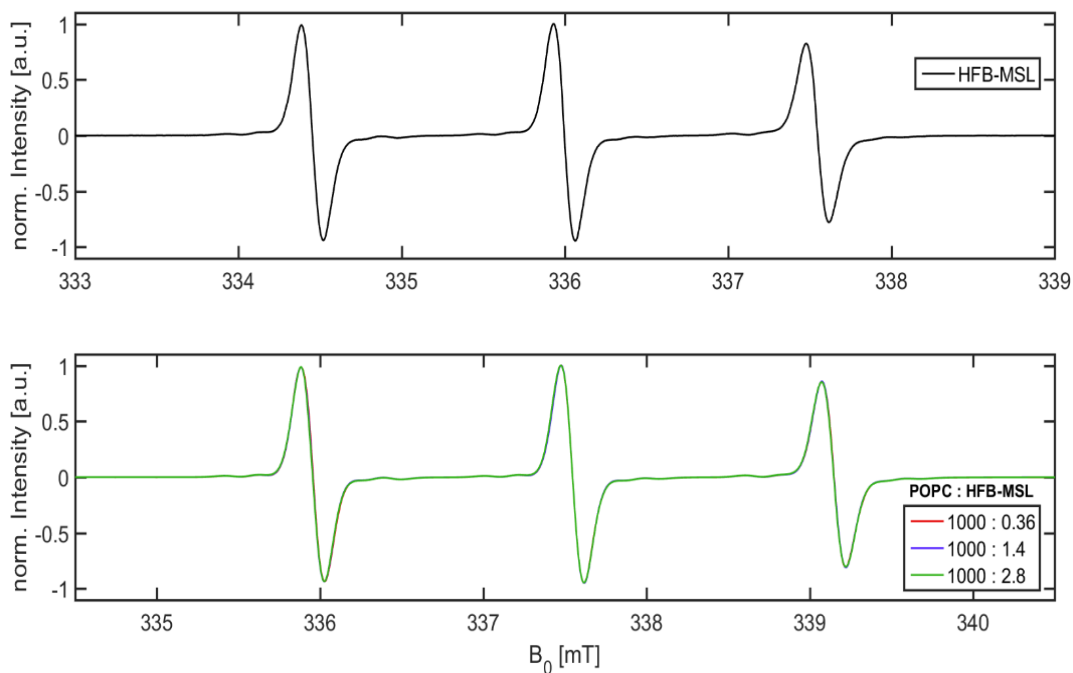


Figure 41 Normalized cwEPR spectra of POPC vesicles with varying amounts of spin-labelled HFB2 recorded in water at 20 °C.

Considering the matching DLS traces it stands to reason that this is true regardless of the presence of a spinlabel at the protein. The changes in particle size may then be explained by the restrictions of the underlying model used for the evaluation of the DLS data. As discussed in **section 2.4**, by the definition of the hydrodynamic radius, a hypothetical spherical particle is assumed. The interaction between protein and vesicle is certain to influence the solvation shell and tumbling of the latter and thus alters the hypothetical spheres size. If and how strongly either protein penetrates the lipid bilayer cannot be conclusively determined from the data at hand; nonetheless, penetration of the bilayer similar to transmembrane proteins is unlikely based on the spectra presented here.

4.4 *SUMMARY AND OUTLOOK*

Both proteins under investigation interact with phospholipid vesicles in solution. Although the exact state of neither is known, several things can be inferred by the observations presented in this chapter. Neither protein seems to penetrate the bilayer, as evidenced by the consistency of the EPR spectra of spin-labelled phospholipids and spin-labelled HFB2. A small guest molecule is released from the liposomes upon interaction with either protein, leading to a dynamic exchange in the case of SC3 and a static release in case of HFB2. This difference might be explained by their respective solution precursor structures and thus seems to indicate that neither protein undergoes self-assembly at the water-liposome interface as they do at the air/water interface. Indeed, WÖSTEN *et al.* found that SC3 secreted into the aqueous environment would self-assemble at the air/water interface and lower the surface tension to allow for the formation of aerial hyphae, but that these assemblies would not subsequently diffuse into the cell wall.

[WÖSTEN, H. A. B., VAN WETTER, M.-A. *ET AL.* 1999] Furthermore, WESSELS and co-workers argued that Hydrophobins are absent in the walls of submerged hyphae and rather regulated to be retained there at a certain stage of fungal development.

[WESSELS, J. G. H., DE VRIES, O. M. H. *ET AL.* 1991]

This raises a number of questions that currently remain unanswered. Firstly, it is not clear why the fatty acid spin probe is released from the liposome to begin with.

A study on the influence of SDS as a model surfactant on phosphatidyl choline vesicles suggested solubilisation of the membrane caused by the surfactant that ultimately lead to the formation of mixed micelles of SDS and phospholipid.

[DEO, N. and SOMASUNDARAN, P. 2002] There was no indication of any interaction between either hydrophobin and 16-DSA in aqueous solution, and neither protein is known to form micellar structures in water. The EPR spectra of the labelled phospholipid reveal no significant changes upon interaction between the liposomes and either protein. The exact mechanism of the interaction between hydrophobins SC3 and HFB2 and liposomes have yet to be elucidated. A feasible approach would be the application of 5-DSA instead, both as a guest and part of a phospholipid. Because the paramagnetic centre would then be much closer to the headgroup region, more significant changes in the probes rotational mobility and direct environment might occur. GLOVER *et al.* demonstrated the suitability of 5-DSA in discerning changes in the fluidity of a membrane. [GLOVER, R. E., SMITH, R. R. *ET AL.* 1999]

Secondly, it is unclear whether this is a class-wide phenomenon among hydrophobins. SC3 and HFB2 are perhaps the best researched members of their respective class and are often used as ‘model members’. The interpretation for the different behaviour of 16-DSA offered in this chapter may imply generalizability; however, much more experimental data on a variety of hydrophobins is needed to investigate this possibility. Thirdly, as mentioned earlier, the exact structure of the proteins in these systems is unknown. In order to get a deeper understanding of the molecular ordering and mechanisms, detailed information on the protein secondary structure elements, oligomerization state and flexibility are needed.

Possible approaches to investigate these parameters include infrared reflection absorption spectroscopy (**IRRAS**) on hydrophobins adsorbed to POPC monolayers and (vibrational) circular dichroism spectroscopy to investigate secondary structure elements prevalent in the protein, and advanced EPR techniques such as double electron - electron resonance (**DEER**) to measure distances between regions of interest within the protein.

Nonetheless, it could be shown here that a triangulation approach by introducing the observed paramagnetic species to different parts of a complex system can offer a vantage ground for understanding the molecular mechanics of such interactions with high precision and at low cost.

5. MULTIPLE FORMS, MULTIPLE FACES

Hydrophobins are remarkable proteins that serve a very broad range of purposes during the fungal life cycle. While major advances towards a detailed understanding of their biological roles and molecular mechanisms as well as their technological application have been achieved since the pioneering work in the early 1990s, some questions and problems of great importance remain yet unsolved. Some generally accepted features have been expanded upon in this thesis. In the first chapter of the present work several questions have been posed regarding the self-assembly process, morphology and other concepts. This chapter shall serve as a concluding remark on the results and ideas presented herein and an attempt to shed light on these questions and give a brief outlook on possibilities and challenges to be tackled by future research.

5.1 *CONTROLLED ASSEMBLY AT THE AIR/WATER INTERFACE*

Hydrophobins self-assemble at hydrophilic/hydrophobic interfaces into complex structures. The morphology and properties of these supramolecular assemblies depend heavily on a variety of factors besides the nature of the interface and of the protein itself. Sample preparation and handling has a major influence on the results obtained by various means. The present work shows remarkable changes in the morphology of surface films formed by two hydrophobins on a micrometre scale, caused by multiple cycles of well controlled lateral constraints and subsequent relief. The differences between data presented here, even at little to no external stress, and a multitude of results published over the recent years, highlight the importance of the experimental procedures applied. The similarity of micron scale structures between two proteins with vastly different primary aggregates that could be found in some samples calls into question the strictness of the established classification system. It was proposed in the present thesis that a combination of drying capillary forces and complex changes in multiple interfaces during evaporation are the main causes for large scale dendritic structures.

The simple fact that multiple processing cycles induce noticeable changes in a variety of crucial parameters, such as surface covering, film thickness and

superstructure size indicates that direct control over the interfacial morphology is possible, at least in principle. Precise governance on different length scales is key for fine-tuned applications in many fields of interest, such as the design of nanomaterials, drug delivery and surface engineering in biomedical, ecological and technological contexts.

Class I hydrophobin SC3 is one of only very few glycosylated members of this protein family. Neither the biological significance nor the influence on the proteins self-assembly are properly explored and understood yet. DE VOCHT *et al.* showed that removal of the sugars weakens the interaction between SC3 and a hydrophobic solid surface, while the surface activity (measured as reduction of the water surface tension) was unaffected. The authors argued that the mannose units play an important part in conformational changes leading to an α -helical state that is crucial for the adsorption of SC3 to solid substrates. [DE VOCHT, M. L., SCHOLTMEIJER, K. *ET AL.* 1998]

Preliminary data for deglycosylated SC3 at the air/water interface shows the emergence of a plateau region in the compression and expansion isotherms. While the achievable surface pressures were similar to native SC3, supporting the aforementioned observation that the surface activity is generally unaffected, the interfacial assemblies seem to react differently to external constraints. It was suggested that the reduced area requirement of deglycosylated SC3 compared to the native protein allows for denser packing in the interface. However, much more detailed analysis is required in order to elucidate the impact of deglycosylation on a molecular level. Glycosylation sites, predicted to be several threonine and serine residues in the N-terminal region, could offer potential for the attachment of other molecules to form functional conjugates with well-adjustable properties. For additional information on conjugates involving hydrophobins a number of studies in various contexts can be suggested as a starting point. [PETERS, R., SANDIFORD, L. *ET AL.* 2016; KOSTIAINEN, M. A., KOTIMAA, J. *ET AL.* 2010]

5.2 *PROTEIN – LIPOSOME INTERACTIONS*

The formation of interfacial structures of hydrophobins is generally believed to be governed by their solution precursors. Much like their biological relevance for the parent organism and their assembly at interfaces, major advances have been achieved in recent years towards an understanding of the predominant solution structure of various hydrophobins, their relationship with and importance for the formation of the resulting interfacial films. But there is still no coherent picture of preassembly and the possible connections between structures in solution and at interfaces. Moreover, the interaction between hydrophobins in solution and complex systems such as cell membranes and liposomes is still only poorly understood. This thesis presents data on the interaction between the studied proteins and simple phospholipid bilayers indicating that both hydrophobins interact with liposomes in similar ways, but with strikingly different effects. It was concluded that neither protein penetrates the lipid bilayer and that the general state of the phospholipids is largely unaffected by the presence of either. In both cases the guest molecule 16-DSA was released from the liposome. In case of class I SC3 this release is reversible, leading to a dynamic exchange of the fatty acid between the interior of the lipid bilayer and the surrounding aqueous solution on a nanosecond timescale. Class II HFB2, on the other hand, leads to an irreversible release of the spin probe. An interpretation of this difference was offered regarding the flexibility of the respective protein's solution structure proposed in the literature. SC3 is believed to form unstructured monomers and functional dimers in solution, which would have large flexible regions, while HFB2 reportedly forms rather rigid dimers and tetramers in solution. This difference in conformational flexibility was proposed to be the cause of their respective effect on the release of 16-DSA from the bilayer. Lastly, a number of open questions have been mentioned and put into context with the presented results. SC3 and HFB2 are arguably the most widely studied hydrophobins at present. Applying a similar methodology to a variety of hydrophobins should provide an answer as to whether the phenomena discussed in here are specific to these proteins or rather represent a general feature based on the accepted classification. It should also be noted that virtually no studies of hydrophobins in any context could be found where EPR spectroscopy was applied. The arguments brought forth

in the present thesis highlight the potential of this technique to discern their behaviour in solution; and a great number of possible approaches remains unpursued. Probing the local environment of specific parts of any hydrophobin in solution, combined with a great number of possible interaction partners, such as liposomes or cell walls and discerning the conformation of solution structures by distance measurements with advanced EPR techniques such as DEER are only two examples that emphasize the power of EPR spectroscopy, which is regularly applied in protein research. In this sense the present thesis marks but a starting point for extensive future research on structure formation in these multifunctional proteins. The ultimate goal remains to develop a cohesive understanding of the molecular processes taking place and the possibilities to influence them to gain access to highly precise ‘tailor-made’ superstructures for technological exploitation.

5.3 *THE MISSING LINK*

While a great deal of insight into the self-assembly processes of several hydrophobins has been gained over the past years, there is still a fundamental gap in our understanding of the connection between the different circumstances, environments and experimental approaches taken to gain a cohesive picture of these fascinating proteins’ behaviour. While our understanding of the morphology and properties of their interfacial films has grown vastly, their behaviour in solution still largely eludes us. Figure 42 aims to illustrate the connection between the ‘areas’ touched upon in this work: the air/water interface, posing questions about the morphology of self-assembled protein films on different scales as well as their precise control; the interactions between hydrophobins and complex structures in solution, opening up the possibility of molecular probing via EPR; and the role that their solution precursors play in either of these fields, the titular ‘missing link’, so to speak.

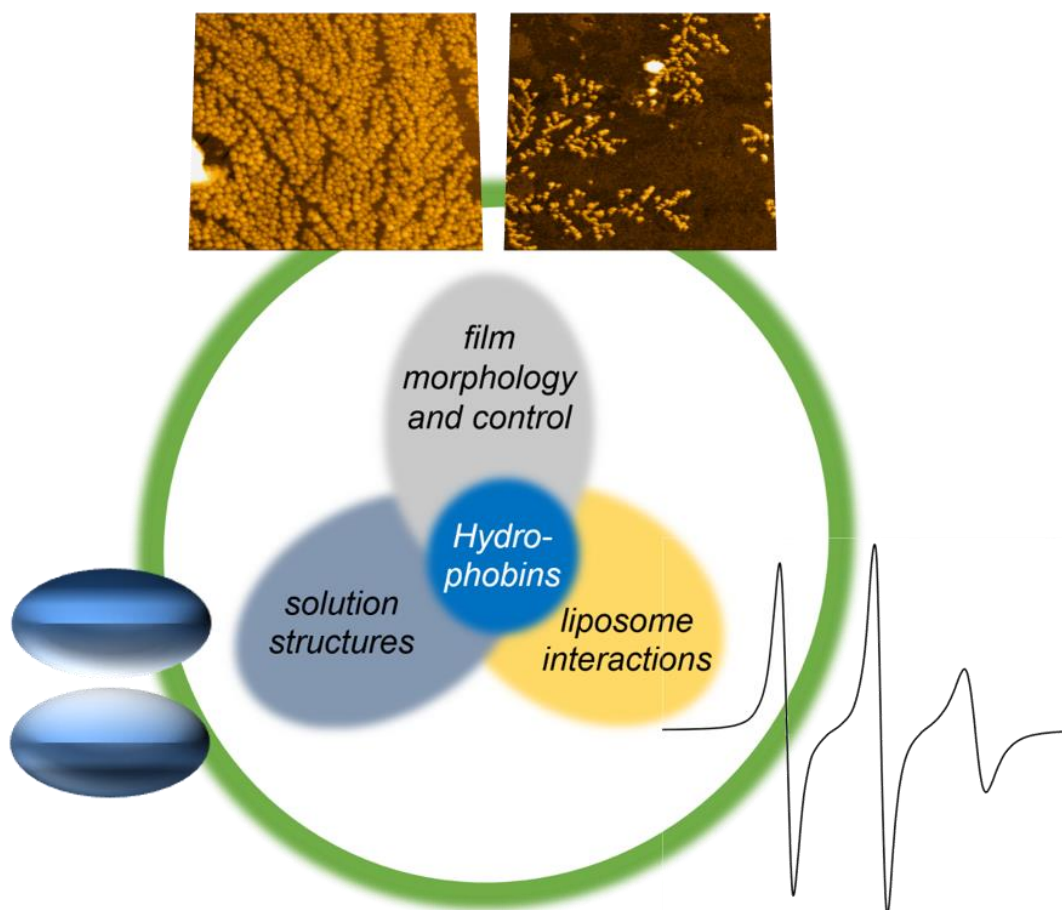


Figure 42 The three main fields of hydrophobin self-assembly and interactions elaborated upon in this thesis: the air/water interface, interactions with liposomes and the solution structures of both proteins.

Hopefully with the still open questions in the previous sections and the corresponding experimental approaches suggested further research will be inspired to enable tapping deeply into the potential of these unique proteins.

6. REFERENCES

- [1] Aïmanianda, V., Bayry, J., Bozza, S., Kniemeyer, O., Perruccio, K., Elluru, S. R., Clavaud, C., Paris, S., Brakhage, A. A., Kaveri, S. V., Romani, L. and Latgé, J. P. (2009). *Nature*. **460**(7259), 1117-1121.
- [2] Askolin, S., Linder, M., Scholtmeijer, K., Tenkanen, M., Penttilä, M., de Vocht, M. L. and Wösten, H. A. B. (2006). *Biomacromolecules*. **7**(4), 1295-1301.
- [3] Babcock, K. (1996). *American laboratory*. **28**(4), 28-30.
- [4] Bayry, J., Aïmanianda, V., Guijarro, J. I., Sunde, M. and Latgé, J.-P. (2012). *PLoS pathogens*. **8**(5), e1002700-e1002700.
- [5] Choi, S. Q., Steltenkamp, S., Zasadzinski, J. A. and Squires, T. M. (2011). *Nature Communications*. **2**, 312.
- [6] Corvis, Y., Brezesinsky, G., Rink, R., Walcarius, A., Van der Heyden, A., Mutelet, F. and Rogalska, E. (2006). *Anal. Chem.* **78**, 4850-4864.
- [7] De Groot, P. W. J., Schaap, P. J., Sonnenberg, A. S. M., Visser, J. and Van Griensven, L. J. L. D. (1996). *Journal of Molecular Biology*. **257**(5), 1008-1018.
- [8] De Stefano, L., Rea, I., De Tommasi, E., Rendina, I., Rotiroti, L., Giocondo, M., Longobardi, S., Armenante, A. and Giardina, P. L. (2009). *The European Physical Journal E*. **30**(2), 181-185.
- [9] de Vocht, M. L., Reviakine, I., Ulrich, W.-P., Bergsma-Schutter, W., Wösten, H. A. B., Vogel, H., Brisson, A., Wessels, J. G. H. and Robillard, G. T. (2002). *Protein science : a publication of the Protein Society*. **11**(5), 1199-1205.
- [10] de Vocht, M. L., Reviakine, I., Wösten, H. A. B., Brisson, A., Wessels, J. G. H. and Robillard, G. T. (2000). *Journal of Biological Chemistry*. **275**(37), 28428-28432.
- [11] de Vocht, M. L., Scholtmeijer, K., van der Vegte, E. W., de Vries, O. M. H., Sonveaux, N., Wösten, H. A. B., Ruyschaert, J.-M., Hadziioannou, G., Wessels, J. G. H. and Robillard, G. T. (1998). *Biophysical Journal*. **74**(4), 2059-2068.
- [12] de Vries, O. M. H., Fekkes, M. P., Wösten, H. A. B. and Wessels, J. G. H. (1993). *Archives of Microbiology*. **159**(4), 330-335.
- [13] Deo, N. and Somasundaran, P. (2002). *Colloids and Surfaces B: Biointerfaces*. **25**(3), 225-232.
- [14] Dons, J. J., Springer, J., de Vries, S. C. and Wessels, J. G. (1984). *Journal of bacteriology*. **157**(3), 802-808.
- [15] Dörfler, H.-D. (2002). Grenzflächen und kolloid-disperse Systeme: Physik und Chemie. Germany, Springer-Verlag Berlin Heidelberg.
- [16] Ebbole, D. J. (1997). *Trends in microbiology (Regular ed.)*. **5**(10), 405-408.
- [17] Eisermann, J. (2017). 3.
- [18] Garcia, R. and García, R. (2002). *Surface science reports*. **47**(6-8), 197-301.
- [19] Gebbink, M. F., Claessen, D., Bouma, B., Dijkhuizen, L. and Wosten, H. A. (2005). *Nat Rev Microbiol*. **3**(4), 333-341.
- [20] Glover, R. E., Smith, R. R., Jones, M. V., Jackson, S. K. and Rowlands, C. C. (1999). *FEMS Microbiology Letters*. **177**(1), 57-62.

- [21] Govor, L. V., Parisi, J., Bauer, G. H. and Reiter, G. (2009). *Journal of physics. Condensed matter*. **21**(26), 264015-264015/264012.
- [22] Govor, L. V., Reiter, G., Bauer, G. H. and Parisi, J. (2006). *Applied Physics Letters*. **89**(13), 133126-133126/133123.
- [23] Hähl, H., Griffio, A., Safaridehkohne, N., Heppe, J., Backes, S., Lienemann, M., Linder, M. B., Santen, L., Laaksonen, P. and Jacobs, K. (2019). *Langmuir*. **35**(28), 9202-9212.
- [24] Hakanpää, J., Paananen, A., Askolin, S., Nakari-Setälä, T., Parkkinen, T., Penttilä, M., Linder, M. B. and Rouvinen, J. (2004). *J. Biol. Chem.* **279**(1), 534-539.
- [25] Heinonen, H., Laaksonen, P., Linder, M. B. and Hentze, H.-P. (2014). *Journal of Biomaterials and Nanobiotechnology*. **05**(01), 1-7.
- [26] Hektor, H. J. and Scholtmeijer, K. (2005). *Curr Opin Biotechnol*. **16**(4), 434-439.
- [27] Holder, D. J. and Keyhani, N. O. (2005). *Appl Environ Microbiol*. **71**(9), 5260-5266.
- [28] Honegger, R. (1991). *Annual Review of Plant Physiology and Plant Molecular Biology*. **42**(1), 553-578.
- [29] Janssen, M. I., van Leeuwen, M. B. M., Scholtmeijer, K., van Kooten, T. G., Dijkhuizen, L. and Wösten, H. A. B. (2002). *Biomaterials*. **23**(24), 4847-4854.
- [30] Junk, M. J. N. (2012). Assessing the functional structure of molecular transporters by EPR spectroscopy. Berlin ;, Springer.
- [31] Karthaus, O., Grasjo, L., Maruyama, N. and Shimomura, M. (1999). *Chaos*. **9**(2), 308-314.
- [32] Karthaus, O., Koito, T. and Shimomura, M. (1999). *Materials Science and Engineering: C*. **8-9**, 523-526.
- [33] Khalesi, M., Deckers, S. M., Gebruers, K., Vissers, L., Verachtert, H. and Derdelinckx, G. (2012). *Cerevisia*. **37**(1), 3-9.
- [34] Kisko, K., Szilvay, G. R., Vuorimaa, E., Lemmetyinen, H., Linder, M. B., Torkkeli, M. and Serimaa, R. (2009). *Langmuir*. **25**(3), 1612-1619.
- [35] Kordts, M., Kerth, A., Drescher, S., Ott, M. and Blume, A. (2017). *Journal of Colloid and Interface Science*. **501**, 294-303.
- [36] Kostianen, M. A., Kotimaa, J., Laukkanen, M.-L. and Pavan, G. M. (2010). *Chemistry – A European Journal*. **16**(23), 6912-6918.
- [37] Kurzbach, D., Junk, M. J. N. and Hinderberger, D. (2013). *Macromolecular Rapid Communications*. **34**(2), 119-134.
- [38] Kwan, A. H., Winefield, R. D., Sunde, M., Matthews, J. M., Haverkamp, R. G., Templeton, M. D. and Mackay, J. P. (2006). *Proc Natl Acad Sci U S A*. **103**(10), 3621-3626.
- [39] Linder, M. B. (2009). *Current Opinion in Colloid & Interface Science*. **14**(5), 356-363.
- [40] Linder, M. B., Szilvay, G. R., Nakari-Setälä, T. and Penttilä, M. E. (2005). *FEMS Microbiol Rev*. **29**(5), 877-896.
- [41] Liu, Y., Nevanen, T. K., Paananen, A., Kempe, K., Wilson, P., Johansson, L.-S., Joensuu, J. J., Linder, M. B., Haddleton, D. M. and Milani, R. (2019). *ACS Applied Materials & Interfaces*. **11**(3), 3599-3608.
- [42] Lugones, L., Bosscher, J. S., Scholtmeyer, K., de Vries, O. M. H. and Wessels, J. G. H. (1996). *Microbiology*. **142**(5), 1321-1329.

- [43] Magonov, S. N., Elings, V. and Whangbo, M. H. (1997). *Surface Science*. **375**(2-3), L385-L391.
- [44] Marek, P., Abedini, A., Song, B., Kanungo, M., Johnson, M. E., Gupta, R., Zaman, W., Wong, S. S. and Raleigh, D. P. (2007). *Biochemistry*. **46**(11), 3255-3261.
- [45] Marshall, K. E., Morris, K. L., Charlton, D., O'Reilly, N., Lewis, L., Walden, H. and Serpell, L. C. (2011). *Biochemistry*. **50**(12), 2061-2071.
- [46] Mulder, G. H. and Wessels, J. G. H. (1986). *Experimental Mycology*. **10**(3), 214-227.
- [47] Paananen, A., Vuorimaa, E., Torkkeli, M., Penttilä, M., Kauranen, M., Ikkala, O., Lemmetyinen, H., Serimaa, R. and Linder, M. B. (2003). *Biochemistry*. **42**(18), 5253-5258.
- [48] Peters, R., Sandiford, L., Owen, D. M., Kemal, E., Bourke, S., Dailey, L. A. and Green, M. (2016). *Photochemical & Photobiological Sciences*. **15**(11), 1448-1452.
- [49] Postulkova, M., Riveros-Galan, D., Cordova-Agiular, K., Zitkova, K., Verachtert, H., Derdelinckx, G., Dostalek, P., Ruzicka, M. C. and Branyik, T. (2016). *Trends in Food Science & Technology*. **49**, 64-73.
- [50] Profit, A. A., VEDAD, J., Saleh, M. and Desamero, R. Z. B. (2015). *Archives of biochemistry and biophysics*. **567**, 46-58.
- [51] Rambach, G., Blum, G., Latgé, J.-P., Fontaine, T., Heinekamp, T., Hagleitner, M., Jeckström, H., Weigel, G., Würtinger, P., Pfaller, K., Krappmann, S., Löffler, J., Lass-Flörl, C. and Speth, C. (2015). *The Journal of Infectious Diseases*. **212**(7), 1140-1149.
- [52] Ren, Q., Kwan, A. H. and Sunde, M. (2013). *Biopolymers*. **100**(6), 601-612.
- [53] Riveros, D. G., Shokribousjein, Z., Losada-Pérez, P., Khalesi, M., Cordova, K., Michiels, C., Delcour, J., Verachtert, H., Wagner, P. and Derdelinckx, G. (2015). *BrewingScience*. **68**, 38-45.
- [54] Schmittschmitt, J. P. and Scholtz, J. M. (2003). *Protein science : a publication of the Protein Society*. **12**(10), 2374-2378.
- [55] Schuren, F. H. J. and Wessels, J. G. H. (1990). *Gene*. **90**(2), 199-205.
- [56] Seidl-Seiboth, V., Gruber, S., Sezerman, U., Schwecke, T., Albayrak, A., Neuhof, T., von Döhren, H., Baker, S. E. and Kubicek, C. P. (2011). *Journal of Molecular Evolution*. **72**(4), 339-351.
- [57] Shieh, I. and Zasadzinski, J. A. (2015). *Proc Natl Acad Sci U S A*. **112**(8), E826-E835.
- [58] Sunde, M., Kwan, A. H., Templeton, M. D., Beever, R. E. and Mackay, J. P. (2008). *Micron*. **39**(7), 773-784.
- [59] Szilvay, G. R., Paananen, A., Laurikainen, K., Vuorimaa, E., Lemmetyinen, H., Peltonen, J. and Linder, M. B. (2007). *Biochemistry*. **46**(9), 2345-2354.
- [60] Tagu, D., De Bellis, R., Balestrini, R., De Vries, O. M. H., Piccoli, G., Stocchi, V., Bonfante, P. and Martin, F. (2001). *New Phytologist*. **149**(1), 127-135.
- [61] Talbot, N. J., Kershaw, M. J., Wakley, G. E., De Vries, O., Wessels, J. and Hamer, J. E. (1996). *The Plant Cell*. **8**(6), 985-999.
- [62] Wang, X., Graveland-Bikker, J. F., De Kruif, C. G. and Robillard, G. T. (2003). *Protein Science*. **13**(3), 810-821.

- [63] Wang, X., Shi, F., Wösten, H. A. B., Hektor, H., Poolman, B. and Robillard, G. T. (2005). *Biophysical Journal*. **88**(5), 3434-3443.
- [64] Wessels, J. G. H. (1994). *Annual Review of Phytopathology*. **32**(1), 413-437.
- [65] Wessels, J. G. H., de Vries, O. M. H., Asgeirsdottir, S. and Schuren, F. H. J. (1991). *The Plant Cell*. **3**(8), 793-799.
- [66] Wessels, J. G. H., De Vries, O. M. H., Asgeirsdottir, S. A. and Springer, J. (1991). *Journal of General Microbiology*. **137**(10), 2439-2445.
- [67] Whitesides, G. M. and Grzybowski, B. (2002). *Science*. **295**(5564), 2418-2421.
- [68] Wösten, H. A. B. (2001). *Annual Review of Microbiology*. **55**(1), 625-646.
- [69] Wösten, H. A. B., Asgeirsdottir, S. A., Krook, J. H., Drenth, J. H. H. and Wessels, J. G. H. (1994). *European journal of cell biology*. **63**(1), 122-129.
- [70] Wösten, H. A. B. and de Vocht, M. L. (2000). *Biochimica et Biophysica Acta (BBA) - Reviews on Biomembranes*. **1469**(2), 79-86.
- [71] Wösten, H. A. B., van Wetter, M.-A., Lugones, L. G., van der Mei, H. C., Busscher, H. J. and Wessels, J. G. H. (1999). *Current Biology*. **9**(2), 85-88.
- [72] Wösten, H. A. B. and Wessels, J. G. H. (1997). *Mycoscience*. **38**(3), 363-374.
- [73] Younan, N. D. and Viles, J. H. (2015). *Biochemistry*. **54**(28), 4297-4306.
- [74] Yu, L., Zhang, B., Szilvay, G. R., Sun, R., Jänis, J., Wang, Z., Feng, S., Xu, H., Linder, M. B. and Qiao, M. (2008). *Microbiology*. **154**(6), 1677-1685.
- [75] Zykwincka, A., Guillemette, T., Bouchara, J. P. and Cuenot, S. (2014). *Biochim Biophys Acta*. **1844**(7), 1231-1237.

APPENDIX

A. CHAPTER 2

As described in **Chapter 2.1** SC3 was extracted from the cultural medium of the parental fungus *S. commune*. The main constituents of this medium are listed in the following table.

Table A - 1 Constituents of liquid culture medium for *S. commune*

compound	CAS-Nr.
Agar-Agar	-
Ammonium molybdate tetrahydrate	12054-85-2
Calcium nitrate tetrahydrate	13477-34-4
Cobalt(II) chloride hexahydrate	7791-13-1
di-Potassium hydrogen phosphate	7758-11-4
Iron(III) chloride	7705-08-0
Hydrogenborate	10043-35-3
Potassium dihydrogen phosphate	7778-77-0
Copper sulphate pentahydrate	7758-99-8
L-Asparagine	70-47-3
Magnesium sulphate heptahydrate	10034-99-8
Malt extract	8002-48-0
Manganese(II) sulphate tetrahydrate	10101-68-5
Soy peptone	91079-46-8
Thiamine	59-43-8
Zinc sulphate hexahydrate	13986-24-8

Agar plates were created from the following medium.

Table A - 2 composition of medium for agar plate cultures of *S. commune*

compound	weighed portion per Litre in g
malt extract	30
Soy peptone	3
Agar-Agar	15

The liquid culture medium was prepared from the so-called minimal medium with the composition listed in **table A – 3**.

Table A - 3 composition of minimal medium for liquid cultures of *S. commune*

compound	weighed portion per Litre
L-Asparagine	1,5 g
Potassium dihydrogen phosphate	0,46 g
di-Potassium hydrogen phosphate	1 g
Magnesium sulphate heptahydrate	0,5 g
Iron(III) chloride	5 mg
Thiamine	0,12 mg

After sterilisation of the minimal medium 50 mL of a 40% glucose solution and 1 mL of the following trace element solution were added to constitute the final liquid medium.

Table A - 4 composition of the trace element solution

compound	weighed portion per Litre
Hydrogenborate	60 mg
Ammonium molybdate tetrahydrate	40 mg
CuSO ₄ x 5 H ₂ O	0.2 g
ZnSO ₄ x 7 H ₂ O	2.0 g
MnSO ₄ x 4 H ₂ O	0.1 g
CoCl ₂ x 6 H ₂ O	0.4 g
Ca(NO ₃) ₂ x 4 H ₂ O	1,2 g

After extraction of the protein as described in **Chapter 2.1** the protein's purity was confirmed by gel electrophoresis. Native SC3 was analysed using SDS-PAGE according to Laemmli using the following buffers:

Table A - 5 Buffer composition for Laemmli-PAGE

10x running buffer	250 mM Tris; 1.92 M Glycin; 1 % SDS
4x sample buffer	500 mM Tris; 10 % SDS; 30 % Glycerole; 40 mM DTT; 10-15 drops of bromophenol blue; pH 6.8
Stacking gel buffer	500 mM Tris; 4 % SDS; pH 6.8
Separating gel buffer	1.5 M Tris; 4 % SDS; pH 8.8

Following the deglycosylation procedure described in **Chapter 2.1.1** Tricine PAGE was performed to investigate the product, because this method allows for better separation of low molecular weight compounds. The buffer composition for the Tricine PAGE is listed below.

Table A - 6 Buffer composition for Tricine-PAGE

10x running buffer	100 mM Tris; 100 mM Tricine; 0.1 % SDS
4x sample buffer	200 mM Tris-HCl; 2 % SDS; 40 % Glycerole; 100 mM DTT; 0.04 % Coomassie Brilliant Blue G-250; pH 6.8

In both cases 120 V of DC voltage was applied for about 20 minutes to collect all samples into the separation gel, followed by 150 V of DC voltage for about 2 hours to achieve separation.

Vesicle solutions were prepared as described in **Chapter 2.7** from stock solution in chloroform according to the following table. (m = mass; V = volume; c = concentration)

Table A - 7 stock solutions used for vesicle preparations

compound	m in mg	V(CHCl ₃) in mL	c in mM
16-DSA	0.42	2	0.546
POPC	20.85	5	5.48
PDSPC	1	1	1.16

B. CHAPTER 4

Figure B - 1 shows X-Band cwEPR spectra of liposomes containing PDSPC with varying amounts of HFB. In section 4.2 it was mentioned that strong Heisenberg spin exchange coupled with the poor signal-to-noise ratio makes the lipid:label ratio of 5:1 poorly suited for EPR investigations.

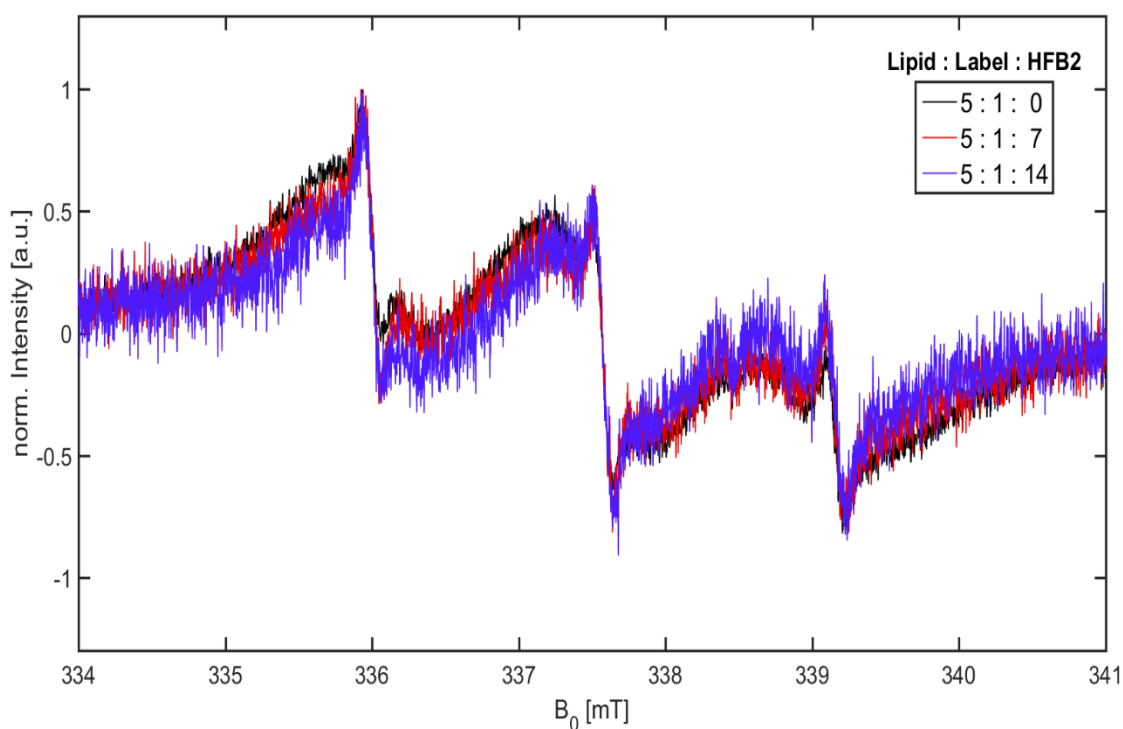


Figure B - 1 cwEPR spectra of POPC:PDSPC vesicles (5:1) recorded in water at 20°C.

As briefly touched upon in section 4.2 the signal-to-noise ratio for vesicles containing the spin-labelled phospholipid was always relatively low. Power sweeps were

performed to investigate the possibility of saturation effects. The resulting saturation curves (Amplitude vs. square root of microwave power) are shown in the following figures. As mentioned in said section, the applied microwave power was 4.79 mW; the square root of which yields 2.188 and thus falls within the linear range for all samples.

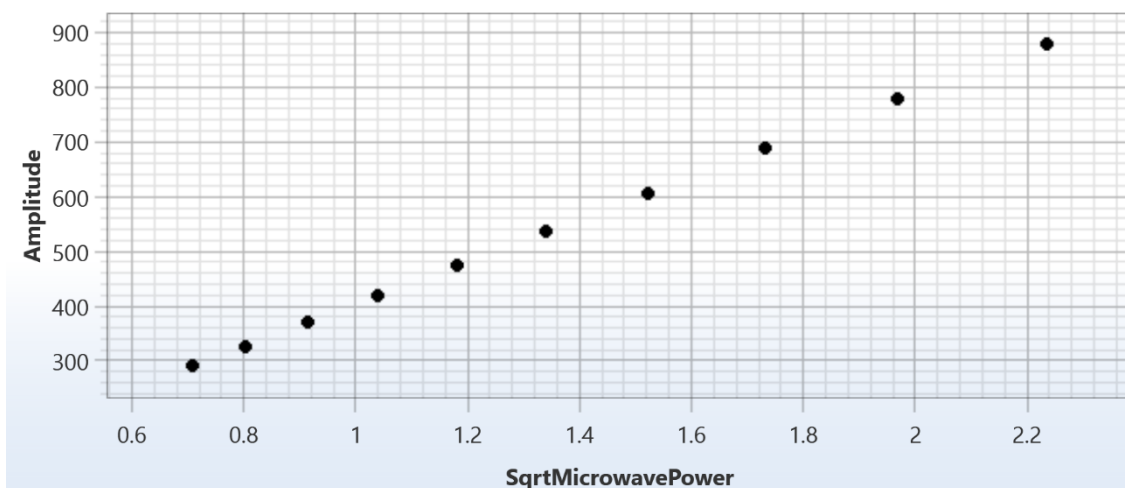


Figure B - 2 Saturation curve for pure POPC: PDSPC vesicles (50:1) recorded at 20°C

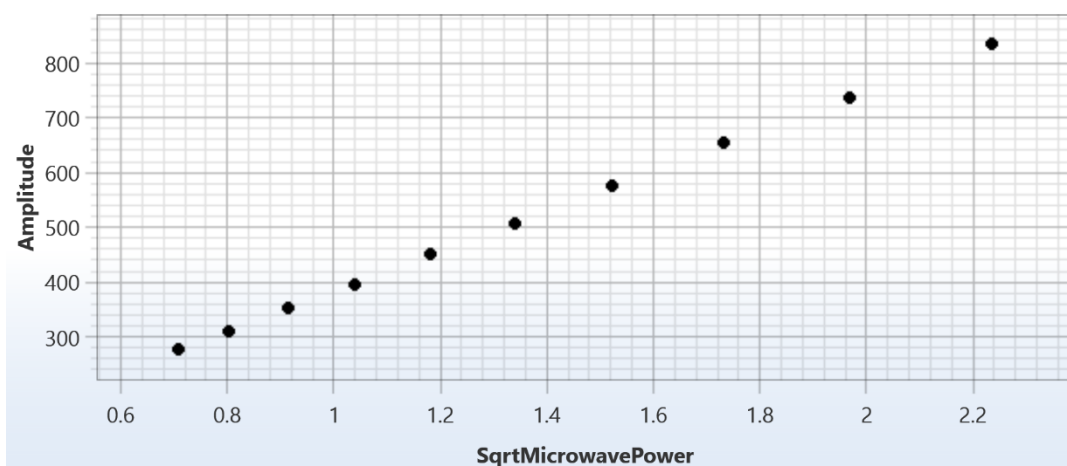


Figure B - 3 Saturation curve for POPC: PDSPC vesicles with SC3 (50:1:7) recorded at 20°C

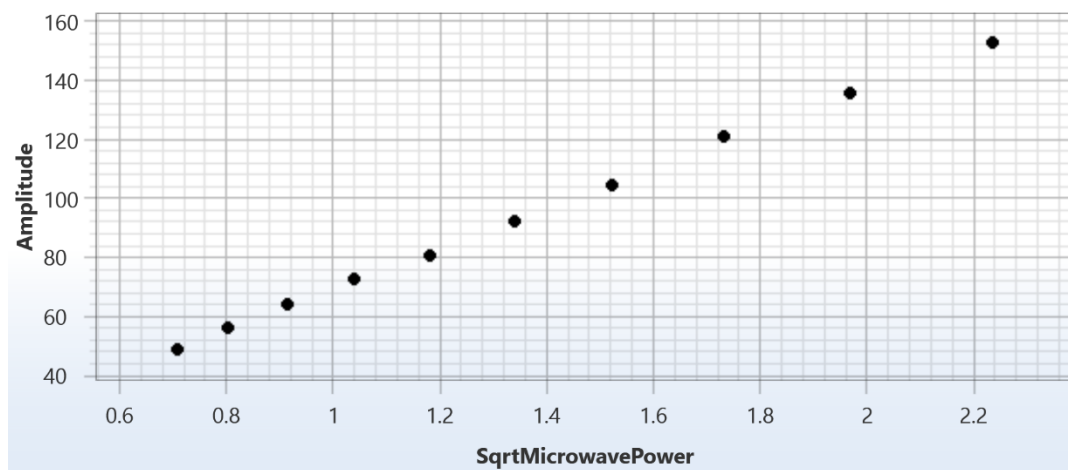


Figure B - 4 Saturation curve for POPC: PDSPC vesicles with HFB2 (50:1:14) recorded at 20°C

ACKNOWLEDGEMENTS

I would like to thank my supervisor Prof. Dr. Dariush Hinderberger for providing the opportunity to pursue the work presented here, for his valuable input and criticism and especially for his remarkable patience in the face of a multitude of technical difficulties in the early stages of this project. A big thank you also goes to Prof. Dr. Thomas Thurn-Albrecht for assuming the mantle of my mentor within the framework of the SFB, and for being a voice of reason and calm in stressful times. A heartfelt thank you also goes to all current and former members of Prof. Hinderberger's working group, especially Dr. Jörg Reichenwallner, Dr. Katharina Laaß and Dr. Jana Eisermann, for lively discussions, active support, both scientific and moral, and the friendliest working environment one could hope for.

Gratitude also goes to Prof. Dr. Alfred Blume, Dr. Andreas Kerth, Dr. Christian Schwieger and all former members and associates of Prof. Blume's working group for introducing me to the field of biophysical chemistry and their continued support in all matters grave or minute during my scientific work in Halle.

A big thank you to Dr. Matt Fuszard for his support with the attempted characterization of various protein species by mass spectrometry.

Special thanks to my former diploma students DLC Melanie Kampe and DLC Katja Peters. Their relentless efforts and dedication contributed invaluable to the work presented herein, and it was delightful to work with both of them for such a long time.

Furthermore, I would like to express my gratitude to my family for their unending support. This includes Jule Würkner, whom I consider family by choice rather than blood. Without her backing and love this work would not have been possible in this form.

Lastly, I would like to thank all members and officials of the SFB TRR 102, for the funding of this project on the one hand and a phenomenal environment for scientific

discussions and pastime activity alike on the other. Dr. Thomas Michael deserves a special mention here for his outstanding work as ‘mother of the doctoral students’.

SCIENTIFIC CONTRIBUTIONS

LIST OF PUBLICATIONS

1. **M. Kordts**, M. Kampe, A. Kerth and D. Hinderberger (2018). "Structure Formation in Class I and Class II Hydrophobins at the Air–Water Interface under Multiple Compression/Expansion Cycles." *ChemistryOpen* 7(12): 1005-1013.
2. **M. Kordts**, A. Kerth, S. Drescher, M. Ott, and A. Blume (2017). "The cmc-value of a bolalipid with two phosphocholine headgroups and a C24 alkyl chain: Unusual binding properties of fluorescence probes to bolalipid aggregates." *Journal of Colloid and Interface Science* 501: 294-303.

ORAL CONTRIBUTIONS

1. Chair of mini symposium of the CRC/TRR 102; 6th June 2019

CONFERENCES

1. M. Kordts, A. Kerth, D. Hinderberger. *Characterization of the Self-Assembly Process of Hydrophobins at Interfaces and in Solution*; ‘Polymers: from Structure to Function’ - Biennial Meeting of the GDCh-Division of Macromolecular Chemistry; 11th – 13th September 2016; poster presentation

2. M. Kordts, K. Peters, D. Hinderberger. *Self-assembly of class I Hydrophobin SC3 at hydrophilic/hydrophobic interfaces*. IDMPC 2017; 17th – 20th September 2017; Wittenberg (Germany); poster presentation
3. M. Kordts, M. Kampe, D. Hinderberger. *Structure formation in Hydrophobins under lateral constraints*. IDMPC 2019; 20th – 23rd October 2019; San Sebastian (Spain); poster presentation
4. M. Kordts, D. Hinderberger. *cwEPR studies of Hydrophobin – liposome interactions in solution*. HALOmem International Meeting on membrane structure and dynamics; 14th – 15th November 2019; Halle (Saale) (Germany); poster presentation

CURRICULUM VITAE

Martin Kordts

PERSONAL INFORMATION

Permanent Address	Bernhardystraße 56 D-06110 Halle (S.), Germany
Date of birth	16 th January 1990
Nationality	deutsch

TIMELINE

1st July 2015 - present	PhD student at Martin Luther University Halle (Saale); group of Prof. Dariush Hinderberger
February 2015 – June 2015	scientific assistant at the Institute of Chemistry, (MLU)group of Prof. Sebastiani, setup and measurement of VCD spectra
July 2014 – January 2015	scientific temporary employee at the Institute of Chemistry, Martin Luther University Halle (Saale); group of Prof. Alfred Blume; extensive supplementary research on the topic of the diploma thesis
October 2013 – April 2014	Diploma in Food Chemistry , received from the Department of Chemistry (Food Chemistry), Martin Luther University Halle (Saale);
<u>Title of Diploma Thesis</u>	<i>„Untersuchungen zum Mizellverhalten von Bolalipiden“</i>
April 2011 – April 2014	Studies of food chemistry; Martin Luther University Halle (Saale);
October 2008 –March 2011	Studies of chemistry (B.Sc.); Martin Luther University Halle (Saale) (MLU) until the 5 th semester

2002 – 2008	Gymnasialzweig, Gesamtschule „Ulrich von Hutten“ (Grammar school), Halle (Saale), Germany; Matriculation standard (Abitur) in 2008 (final mark 1,6)
2000 – 2002	Sekundarschule „August Hermann Francke“ (secondary school), Halle (Saale)
1996 – 2000	Grundschule „August Hermann Francke“ (primary school), Halle (Saale)

LANGUAGES

German	native
English	fluent in speech and writing
French	basic in speech and writing
Italian	basic in speech and writing
Irish	basic in speech and writing

SUPPLEMENTARY TRAINING AND TECHNICAL SKILLS

- Advanced Training Module (ATM) “Infrared Reflection Absorption Spectroscopy (IRRAS); 14th – 15th November 2016
- Training course in First Aid by the Deutsche Gesetzliche Unfallversicherung (DGUV); 21st June 2017
- ATM “Introduction to Small and Wide Angle X-Ray scattering”; 13th – 14th February 2018
- Setup of VCD spectrometer at MLU
- Practical training in aspects of atomic force microscopy at the Centre for Innovation Competence ZIK SiLi-nano®, 17th October 2017; Halle (Saale)

TEACHING EXPERIENCE

- Lab course physical chemistry – fluorescence spectroscopy for M.Sc. Chemistry; summer semesters 2015/2016/2017
- Lab course physical chemistry for food chemists; winter semesters 2015/16, 2016/17, 2017/18 and 2018/19
- Lab course physical chemistry (minor subject), summer semester 2019

EIGENSTÄNDIGKEITSERKLÄRUNG

Hiermit erkläre ich an Eides statt, dass ich die vorliegende Arbeit selbstständig und ohne fremde Hilfe verfasst, keine anderen als die hier genannten Quellen und Hilfsmittel verwendet und alle den verwendeten Quellen wörtlich oder inhaltlich entnommenen Stellen als solche gekennzeichnet habe.

Martin Kordts

Halle (Saale), den _____